A KINEMATIC STUDY OF 0509-67.5, THE SECOND YOUNGEST SUPERNOVA REMNANT IN THE LARGE MAGELLANIC CLOUD, AND ITS ASTROPHYSICAL IMPLICATIONS

By

LUKE HOVEY

A dissertation submitted to the

Graduate School–New Brunswick

Rutgers, The State University of New Jersey

In partial fulfillment of the requirements

For the degree of

Doctor of Philosophy

Graduate Program in Physics and Astronomy

Written under the direction of

John P. Hughes

And approved by

_____

_____

_____

_____

_____

New Brunswick, New Jersey

January, 2016

ABSTRACT OF THE DISSERTATION

A Kinematic Study of 0509-67.5, the Second Youngest Supernova Remnant in the Large Magellanic Cloud, and its Astrophysical Implications

By LUKE HOVEY

Dissertation Director:

John P. Hughes

Supernova remnants are the lasting interactions of shock waves that develop in the wake of supernovae. These remnants, especially those in our galaxy and our companion galaxies, allow us to study supernovae for thousands of years after the initial stellar explosions. Remnants that are formed from Ia supernovae, which are the explosions and complete annihilation of white dwarf stars, are of particular interest due to the explosions' value as standard candles in cosmological studies. The shock waves in these young supernova remnants offer an unparalleled look into the physical processes that take place there, especially since these shocks are often simpler to study than shocks with strong radiative components that are present in remnants that are formed from the core-collapse supernovae of massive stars. I will detail the work of my kinematic study of the second youngest remnant in the Large Magellanic Cloud, 0509−67.5, which has been confirmed to be the result of a Ia supernova. Chapter 2 details the proper motion measurements made on the forward shock of this remnant, which has led to many key results. I was able to use the results of

the global shock speed in the remnant to measure the density of neutral hydrogen in the ambient medium into which these shocks expand. In addition, I use the measurements of the shock speed for select portions of the forward shock to search for signatures of efficient cosmic-ray acceleration. Hydrodynamic simulations are then employed to constrain the age and ambient medium density of 0509−67.5, as well as to place limits on the compression factor at the immediate location of the blast wave. Chapter 3 uses the proper motion results from chapter 2 to determine possible asymmetries in the expansion of the remnant for the eastern and western limbs. These measurements are then used as constraints in hydrodynamic simulations to assess the possible dynamical offset of the explosion site compared to the geometric center of 0509−67.5 that we observe today. I find a continuum of possible offsets, which are sensitive to assumptions that are made about the evolutionary history of the remnant, and use the uncertainties in these calculations to determine the area in which to search for a leftover progenitor companion star in the event that the explosion resulted from a single-degenerate system. The stars within this search area are explored with a multi-band photometric study, wherein we determine the mass ranges for these candidates. Chapter four concludes this thesis, recapping the main results from chapters 2 and 3, and highlights the future projects I will carry out that are motivated by my findings in this comprehensive study of the supernova remnant 0509−67.5.

Acknowledgments

First and foremost, I would like to thank my adviser Dr. John P. Hughes, a.k.a. Jack, for all of his help through my tenure as a graduate student at Rutgers University. His patience and understanding have proved instrumental in guiding me through the emotional roller coaster of obtaining a PhD. He has been a boss, friend, colleague, and advocate for me through the peaks of my academic successes and birth of my children, as well as through the valleys of my life. It is impossible for me to put into words how truly appreciative I am for everything he has done.

I would also like to thank my Rutgers committee members Dr. Andrew Baker, Dr. Robert Bartynski, and Dr. Rachel Somerville for their helpful comments and suggestions on the preparation of this thesis. Also, I would like to thank Dr. Parviz Ghavamian, who is an expert on supernova remnants and Balmer-dominated shocks, for taking the time to serve as my external committee member.

I would also like to thank my family: my father Steven Sr., my mother Lillian, my brother Steven Jr., my wife Kate, and my beloved children Isaac and Alexander, who are my most important creations in graduate school. Perhaps my greatest thanks goes to my late grandfather Howard Hale Hovey. He was the first to interest me in astronomy with the walks he would take with my cousins and me, where he would teach us about the constellations and the mythology behind each one. Most importantly, he taught me to always ask questions, because it is the only way to learn something new.

Chapter two of my thesis has been published by the Astrophysical Journal in August of 2015 with the reference Hovey et al. (2015). The paper is co-authored with John P. Hughes

and Kristoffer Eriksen. Chapter three of my thesis is in preparation for its imminent submission to the Astrophysical Journal and is co-authored by John P. Hughes and Kristoffer Eriksen.

I would like to thank Kevin Heng for providing me with the numerical results of the Balmer shock models found in van Adelsberg et al. (2008), which was integral to chapter 2 of my thesis. In addition, I would like to thank Chelsea Sharon, Curtis McCully, and Saurabh Jha for help with various aspects of the analysis for Hovey et al. (2015).

Dedication

For my best friend and partner in life Kate,

my beautiful children Isaac and Alexander,

and my late beloved Grandfather, Howard Hale Hovey,

who always challenged me to ask questions and **never stop learning**.

Table of Contents

List of Tables

List of Figures

Chapter 1

Introduction

Supernovae (SNe) are among the most violent events in the universe, with kinetic energies on the order of $\sim 10^{51}$ erg. This is so vast that it is of the same order as the entire energy output produced from throughout the entire existence of the star's life. During peak brightness, the luminosity of a SN sometimes outshines its host galaxy for weeks to months.

SNe are characterized by both their spectra and their light curves. The two main classifications of SNe are Type I and Type II, and each has its own subclasses. Type I SNe are defined by an absence of hydrogen lines in their spectra (Minkowski 1941). There are three subtypes of these SNe: Type Ia, Type Ib, and Type Ic. Type Ia SNe are unique in many regards, including remarkably homogeneous light curves and spectra (Filippenko 1997). The spectra of Type Ia SNe contain a distinct SiII absorption line around 6150 Å (Filippenko 1997, and references therein); this line is unique among Type I SNe. Type Ib and Type Ic SNe are characterized by the presence or absence, respectively, of He I lines around 5876 Å(Wheeler & Harkness 1986). The light curves of the different Type I SNe are much more similar than the light curves of Type II SNe (Leibundgut et al. 1991; Patat et al. 1993; Filippenko 1997).

Type II SNe distinguish themselves from Type I events by the presence of hydrogen lines in their spectra (Minkowski 1941). The three main subtypes of these SNe are: Type II-P, Type II-L, and Type IIn. Type II-P SNe are named due to the plateau that can be seen in their light curves, which remain within a magnitude of their peak luminosities for an extended period (Schmitz & Gaskell 1988; Young & Branch 1989). Type II-L exhibit light curves that are strikingly linear in their decline from maximum light (Young & Branch 1989;

Gaskell 1992). Type IIn SNe are distinct among all the other SNe, by having extremely weak or no absorption features in their spectra. These stars are thought to be exploding into extremely dense circumstellar gas and dust. Instead of showing prominent absorption lines, Type IIn spectra contain emission features, the most prominent being a narrow Hα emission line (hence, Type IIn) (Schlegel 1990; Filippenko 1997).

With the exception of Type Ia, all of the subclasses of SNe are core collapse SNe. A core collapse SN occurs at the end of a high mass star's ($M > 8M_{\odot}$) life (Filippenko 1997; Carroll & Ostlie 2006). After a high mass star exhausts the hydrogen in its core, it will begin to fuse helium. The helium will be exhausted rapidly, and the star will fuse elements with increasing atomic numbers until the core starts to burn silicon. In the silicon burning phase, iron is formed; this iron core is incredibly dense and degenerate. Once a star's core contains $\sim 1.4M_{\odot}$ of iron, the degenerate electrons providing an outward pressure become relativistic and the equation of state changes from $\gamma = 5/3$ to $\gamma = 4/3$. At this point, the electron degeneracy pressure can no longer balance the gravitational force, resulting in the collapse of the star's core. As the core collapses, electrons will merge with protons to form neutrons, which will again begin to prop the core up against the force of gravity. If the resulting core can be supported by neutron degeneracy pressure, the collapse will halt and a neutron star will be left behind. If, on the other hand, the force of gravity is still dominating the neutron degeneracy pressure, the core will collapse to a radius of essentially zero, and a black hole will remain. As a result of the collapsing core, a rebound will drive shocks into the in-falling outer layers, which are re-energized by the massive flux of escaping neutrinos.

Type Ia SN proceed through a process vastly different from the core-collapse explosions. It is thought that a Ia SN results from the thermonuclear detonation of a carbon-oxygen white dwarf star (WD) as its mass approaches the Chandrasekhar mass (Branch et al. 1995). No compact object or stellar remnant remains as the Ia explosion completely unbinds the white dwarf star (Woosley & Weaver 1994). These SNe are of great interest since they can

be used as "standard candles" to measure distances on cosmological scales (Phillips 1993). Type Ia SNe proved instrumental in the discovery of the accelerating universe, powered by the enigmatic dark energy (Riess et al. 1996, 1998; Perlmutter et al. 1999), which accounts for 75% of the energy density of the universe; despite the findings that this dark energy is so prevalent in the universe, its nature remains a mystery.

I will focus primarily throughout this thesis on supernova remnants that result from Ia SN explosions. The structure of this introductory chapter is as follows: In §1.1 I will discuss the structure and evolution of SNRs. Section 1.2 will cover how we can determine the SN type with observations of SNRs. I will discuss the evidence for the efficient acceleration of cosmic rays in the shocks of SNRs in §1.3. Section 1.4 concludes the introduction, where I discuss how we can determine the progenitor systems of Ia SNe with observations of the remnants they leave behind.

1.1 Supernova Remnants

The light we observe from a Ia SN results from the radioactive decay of ^{56}Ni, and then ^{56}Co to ^{56}Fe, in the wake of the explosion. As this radioactive glow fades, the light that is observed from the object is a result of shock waves plowing into both the surrounding ambient material and the ejecta from the star that exploded; this marks the transition from SN to the supernova remnant (SNR) phase. These remnants play host to a variety of physical processes, making them ideal astrophysical laboratories.

1.1.1 Supernova Remnant Structure

From the onset of the SN explosion, the ejecta from the progenitor propagate radially at supersonic velocities through the ambient medium that surrounded the star. As this blast wave, which we call the forward shock, sweeps up ambient gas and dust, it will begin to decelerate. In this deceleration, ejecta moving at higher velocities than the forward-moving shock begin to pile-up as unshocked ejecta slam into shocked ejecta, and the material is

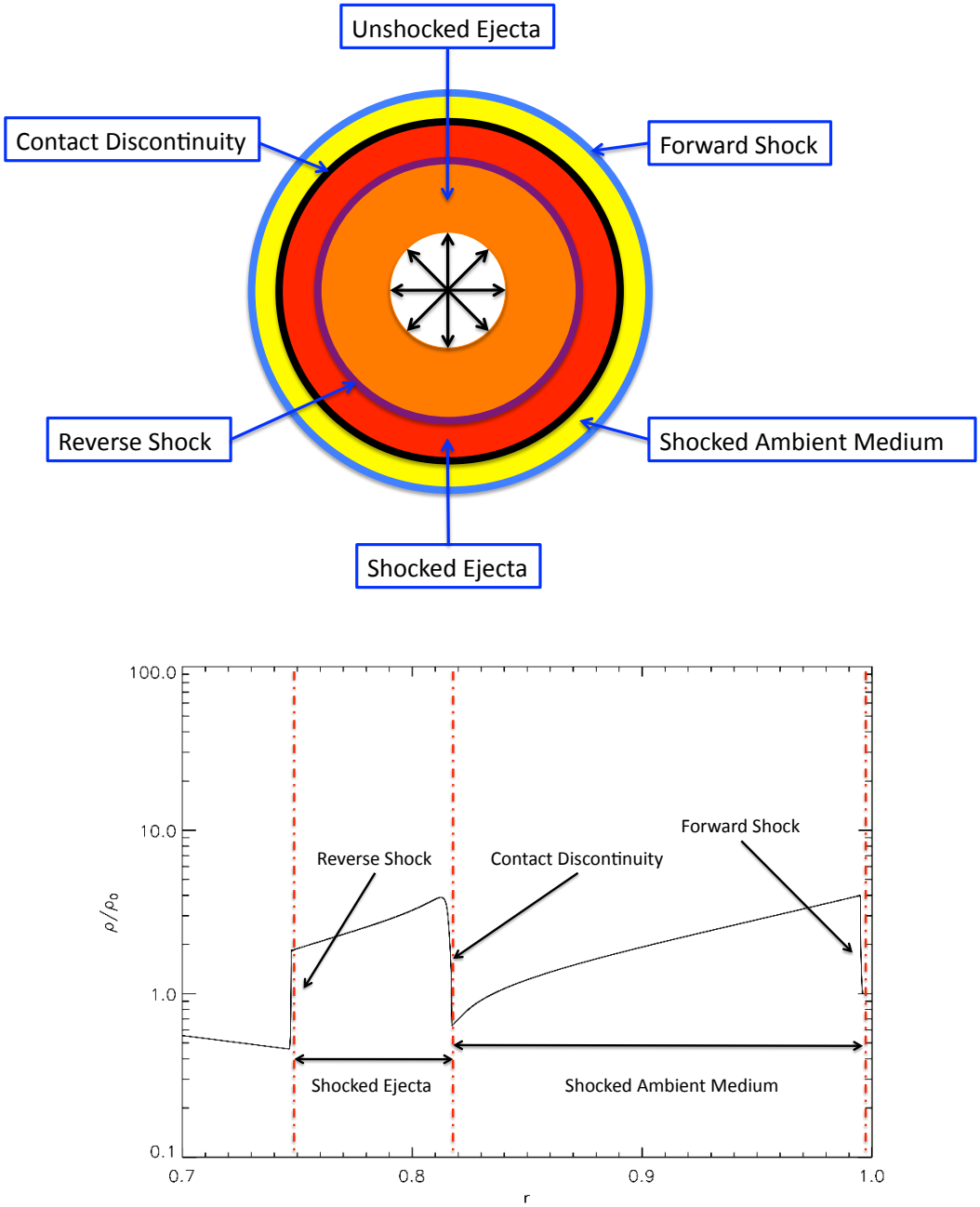

Figure 1.1 *Top* Cartoon representing the two-shock structure of a SNR. *Bottom* Density vs. radius from a one dimensional hydrodynamic simulation at a dimensionless time of unity. The radius is normalized to the position of the forward shock and density is normalized to the ambient medium density.

heated and compressed (McKee 1974). As a result of this, a"reverse-shock" will begin to propagate inwards towards the center of the SNR in the rest frame of the ejecta. Between the regions of shocked ambient medium and shocked ejecta is a contact discontinuity, which is Rayleigh-Taylor unstable. Figure 1.1 *top* shows a cartoon depicting these features of a young SNR. The *bottom* panel of figure 1.1 shows a density vs. radius plot of this structure from a one-dimensional hydrodynamic simulation in which the ejecta are initialized with an exponential density profile. The density is normalized to the ambient medium density and the radius to the position of the forward shock.

The governing equations of motion for a given parcel of gas in a SNR are given by the Euler equations of fluid dynamics (e.g., Landau & Lifshitz (1959); Zel'dovich & Raizer (1967)), which follow as:

$$\frac{D\rho}{Dt} = -\rho\left(\nabla \cdot \vec{u}\right), \tag{1.1}$$

$$\frac{D\vec{u}}{Dt} = -\frac{\nabla P}{\rho} + \vec{g}, \tag{1.2}$$

and

$$\frac{D\epsilon}{Dt} = -\frac{P}{\rho}\left(\nabla \cdot \vec{u}\right). \tag{1.3}$$

In these equations ρ is density, P is pressure, $\vec{u}$ is the velocity of the fluid, $\vec{g}$ is the gravitational acceleration per unit mass, and ϵ is the specific internal energy. The left hand side of the equations are given in the short-hand notation for the convective derivative, which is defined as:

$$\frac{D\phi}{Dt} = \frac{\partial\phi}{\partial t} + \vec{u} \cdot \nabla\phi. \tag{1.4}$$

The conservation equations describing the conditions of a shock wave in one dimension in the absence of magnetic fields are the Rankine-Hugoniot relations (Zel'dovich & Raizer 1967), which are derived from equations 1.1, 1.2, and 1.3. For shocks in SNRs, the gravitational force, and hence $\vec{g}$ in equation 1.2, is negligible and can be assumed to be zero in the derivation of the Rankine-Hugoniot equations. These relations are conservation equations

for mass, momentum, and energy directly behind and at the shock front, which follow as:

$$\rho_0 \vec{v_0} = \rho_1 \vec{v_1}, \tag{1.5}$$

$$P_0 + \rho_0 v_0^2 = P_1 + \rho_1 v_1^2, \tag{1.6}$$

and

$$\epsilon_0 + \frac{\gamma P_0}{(\gamma - 1)\,\rho_0} + \frac{1}{2} v_0^2 = \epsilon_1 + \frac{\gamma P_1}{(\gamma - 1)\,\rho_1} + \frac{1}{2} v_1^2. \tag{1.7}$$

Here the subscripts 0 and 1 denote the pre and post-shock conditions respectively, P is the pressure, γ is the equation of state for the gas (given by the ratio of specific heats c_P/c_v), ρ is density, ϵ is the specific internal energy, and $\vec{v}$ is the velocity of the fluid. The compression factor, or jump-factor, for high Mach number shocks that are typical in young SNRs is

$$\frac{\rho_1}{\rho_0} = \frac{\gamma + 1}{\gamma - 1}, \tag{1.8}$$

and describes the conditions at the interface of the forward shock. This compression factor is 4 for an adiabatic gas with $\gamma = \frac{5}{3}$, and 7 for a relativistic gas with an equation of state of $\gamma = \frac{4}{3}$.

1.1.2 Supernova Remnant Evolution

SNRs evolve as they interact with the surrounding ambient medium of gas and dust. The different phases of evolution serve as a guide to model the dynamics of a remnant's shock waves and contact discontinuity. At first, the forward shock expands rather unimpeded in a period of relative free expansion, where the spectrum of the remnant is dominated by the ejecta; this phase is known as the ejecta-dominated (ED) phase of the SNR's evolution. Once the blast wave has swept up a mass comparable to the mass of ejecta, the remnant enters an adiabatic phase of expansion known as the Sedov-Taylor (ST) phase (Truelove & McKee 1999). These phases are considered to be non-radiative, in the sense that the radiation emitted from the remnant does not appreciably alter the dynamics of the system. Finally, the remnant will enter a radiative phase, where the shocked ambient medium behind the blast wave cools radiatively.

The dynamics of the forward and reverse shocks in both the ED and ST phases can be modeled by similarity solutions if the ejecta of the explosion are assumed to have a power-law profile (Sedov 1959; Chevalier 1982; Hamilton & Sarazin 1984). The transition between these two phases cannot be explained by a similarity solution; therefore, the fluid equations must be calculated with an analytical solution like those provided in Truelove & McKee (1999), or alternatively, through hydrodynamic simulations, which solve the Euler equations numerically. Since the evolution of the blast wave is self-similar, characteristic scales are used in order to make the parameters dimensionless in order to solve the equations of hydrodynamics. These scales can be defined by the three parameters which moderate the dynamics of the SNR evolution: the explosion energy of the initial explosion (E), the mass of the ejecta (M_{ej}), and the density of the ambient medium (ρ_0). The characteristic scales of length, velocity, and time naturally follow from dimensional analysis and are defined as follows:

$$\mathrm{R_{ch}} = \left(\frac{\mathrm{M_{ejecta}}}{4/3\pi\rho_0}\right)^{1/3}, \tag{1.9}$$

$$\mathrm{V_{ch}} = \left(\frac{2\,\mathrm{E_{51}}}{\mathrm{M_{ejecta}}}\right)^{1/2}, \tag{1.10}$$

and

$$\mathrm{t_{ch}} = \frac{\mathrm{R_{ch}}}{\mathrm{V_{ch}}} = \mathrm{M_{ejecta}}^{5/6}\,(4/3\pi\rho_0)^{-1/3}\,(2\,\mathrm{E_{51}})^{-1/2}\,. \tag{1.11}$$

The characteristic time listed here (Eqn. 1.11) is the approximate time for the onset of the SD phase of the remnant's evolution (Truelove & McKee 1999).

Chevalier (1982) argues that the ejecta in Type Ia SNRs are modeled well by a power law distribution with an ejecta density profile of $\rho \propto r^{-7}$. Truelove & McKee (1999) expand on this profile and find exact solutions for the position and speed as a function of time for both the forward and reverse shocks. The solutions they present describe the motion of the blast wave as having a radius of $R_b \propto t^{\eta}$; η is the expansion factor and varies from

$\eta = 1$, during the ED phase, to $\eta = \frac{2}{5}$, in the adiabatic ST phase of evolution. The results of these solutions only deviate by a few percent from the exact solutions of hydrodynamic simulations (Truelove & McKee 1999).

Dwarkadas & Chevalier (1998) argued that a power law distribution for the initial density profile is an oversimplification, and that an exponential is a more realistic modeling of the ejecta. Using this profile, Dwarkadas & Chevalier (1998) show that in almost every explosion model, the exponential density profile is much more representative of the ejecta stratification (just before interacting with the ambient medium) than power-law ejecta profiles. The biggest difficulty with using more complicated ejecta profiles is that there are no analytic solutions of the Euler equations, so we must calculate the dynamics of the forward and reverse shocks with hydrodynamic simulations.

1.1.3 Balmer-dominated Shocks in Supernova Remnants

Tycho's SNR (Tycho hereafter) and SNR 1006, are the most studied remnants, thought to be of Type Ia origin. These remnants belong to an exclusive class of SNRs, known as Balmer-dominated remnants (BDRs). They are named this due to the presence of Balmer-dominated (BD) shocks around the remnant.

BD shocks show Balmer emission in their optical spectra, with little evidence for metal lines or the forbidden emission transitions, which are often observed in other radiative shocks. This emission is thought to trace out the forward shock of the SNR, where it interacts with the ambient medium. Chevalier et al. (1980) proposed a model to explain BD shocks as disturbances ($v_s \geq 1000$ km s^{-1}) that expand into a partially neutral and uniform ambient medium.

BD shocks are collisonless, since the mean free path for particle collisions is much larger than the gyroradius created by the compression in the forward shock of ambient magnetic field lines in the ambient material (Chevalier et al. 1980; Heng 2010). The magnetic fields are turbulent and ions are accelerated back and forth across the shock.

Spectroscopically, the Balmer emission lines exhibit broad and narrow components, with the most prevalent being the Hα emission line. The broad component arises from charge exchange between a neutral preshock hydrogen atom entering the shock that passes its electron to a proton that has been shock heated ($H^0_{cold} + p^+_{hot} \rightarrow H^*_{hot} + p^+_{cold}$) (for a thorough review on BD shocks see Heng 2010, and sources therein). This process will result in an excited, neutral, and hot hydrogen atom, which radiates as the electron de-excites. This emission yields information about the post-shock gas in the remnant, such as the post-shock ion temperature. The narrow component arises from collisional excitations of neutral hydrogen entering the shock ($H^0_{cold} + e^-_{hot} \rightarrow H^*_{cold} + e^-_{hot}$). In addition to collisional excitations, there will also be collisional ionization in the interaction region of the forward shock. The reaction time for the collisional excitation is less than that of the process of collisional ionization, which makes the Balmer emission possible. The ionization timescale is still quite comparable to the rate of the Balmer emission, and hence these shocks form a spatially thin rim with a thickness $\leq 10^{16}$ cm (Ghavamian et al. 2007).

Figure 1.2 *left* is an example of a SNR with BD shocks. This is the Large Magellanic Cloud (LMC) remnant 0519−69.0, and the image is a narrow-band Hα image where we can see these Balmer shock filaments surrounding the entire SNR. I obtained low-resolution optical spectra with the Robert Stobie Spectrograph (RSS) from the Southern African Large Telescope (SALT) from the two slit positions shown. The bottom two panels show the two-dimensional spectra from the two slit locations and there is a red box that highlights the spectrum from the eastern limb of the remnant (indicated with a black box in the Hα image on the left). The middle panel on top shows the one dimensional spectrum that is extracted from the aforementioned filament, and shows only the Balmer emission lines Hα, Hβ, Hδ, and Hγ. We can see that the Hα line is the dominant emission line and can see the narrow component surrounded by the broad component, which has a flux comparable to the narrow component. The panel on the top-right is a zoom-in of the broad Hα component from the same eastern shock, which is clearly discernible from the brighter narrow Hα component.

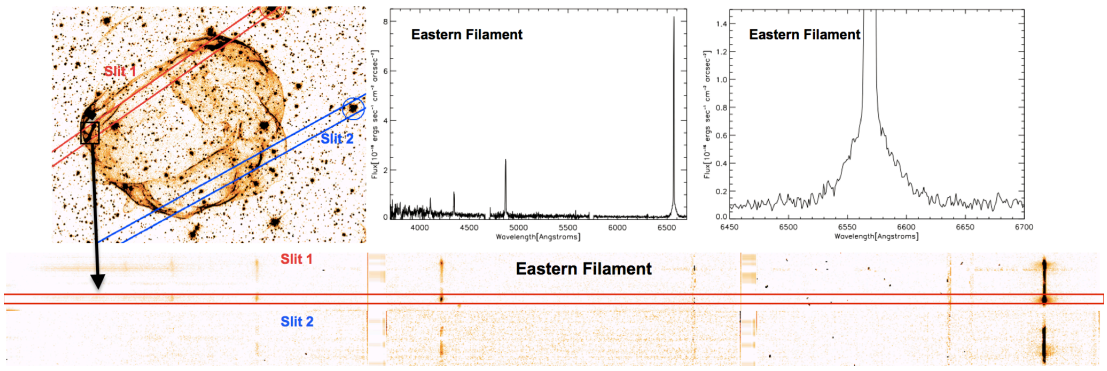

Figure 1.2 **Top Row** *Left* - *HST* narrow-band Hα imaging of 0519−69.0, along with the two longslit positions from which I obtained SALT RSS spectra. A black square highlights an eastern filament that we present in the following two panels and a black arrow indicates the two dimensional spectrum along with its extraction aperture. *Middle* - Longslit spectrum of the eastern shock filament of 0519−69.0. Detections of Hα, Hβ, Hγ, and Hδ with no other apparent emission lines. *Right* - A magnified view of the Hα emission line of the eastern shock, which clearly shows a prominent broad Hα component. **Bottom Row** - Two dimensional longslit spectra of 0519−69.0 imaged with the SALT RSS are shown. Night sky lines and stellar continuum have been subtracted. The extraction region of the eastern filament of 0519−69.0 for the spectrum shown above is highlighted with a red box.

Other extra-galactic BD SNRs, such as those in the LMC, have proved important in understanding the physics of shockwaves in SNRs. One important advantage of remnants in the LMC is that they are not plagued by uncertainties in their distance measurements (as is the case with Kepler's SNR and 1006). This allows us to determine the physical shock speeds and size of a remnant directly. By comparison, shock speeds determined in the Galactic remnants are calculated with Balmer shock models, which are also used to place limits on the distance to these Galactic remnants.

Tuohy et al. (1982) provide the striking examples of extragalactic SNRs that are of Type Ia origin. Interestingly, these remnants were not initially identified from radio counterparts, but from an X-ray survey conducted by Long et al. (1981) with the aid of the *Einstein Observatory*. Tuohy et al. (1982) found that the radio emission from these SNRs is surprisingly faint, hinting at a fundamental difference either in the particle acceleration in BD remnants, or in the nature of the ISM of the LMC. The BD SNR 0509-67.5 in the LMC will be explored at length in chapters 2 and 3.

We will see in §1.2.1 and in §1.3 the usefulness of these shocks for typing SNRs and probing for evidence of efficient cosmic ray acceleration. Chapters 2 and 3 will examine the dynamics of BD shocks in the LMC SNR 0509−67.5, which is approximately the same size as 0519−69.0, which I provided as an example of the properties of BD shocks.

1.2 How do we Type Supernova Remnants?

While typing a SN as being a Ia or core-collapse is relatively straight forward through optical spectroscopy, the typing of SNRs requires more sophisticated techniques. We will discuss the most reliable arguments/methods of typing remnants as follows: the Balmer-dominated remnant argument, X-ray spectra of ejecta, emission line morphology, and light-echoes.

1.2.1 Balmer-dominated Remnant Argument

Tuohy et al. (1982) identified four SNRs in the LMC that were surrounded by BD shocks. These remnants form a unique class of objects referred to as BDRs, where Tycho is referred to as the prototypical BDR. As mentioned earlier, Chevalier et al. (1980) presented a model for this emission where a shock is interacting with a partially neutral ambient medium. This model of the Balmer emission from these shocks is the key argument that remnants with high-speed BD shocks would not be consistent with a core-collapse supernova. The rationale is that a massive progenitor star would have had strong ionizing winds that would not leave a partially ionized medium; therefore, it is unlikely that BD shocks would develop in a remnant that it left behind. While there is evidence of BD shocks in some evolved core-collapse remnants like the Cygnus Loop (Raymond et al. 1983), they do not surround the periphery of these remnants, which thus are not BDRs and are at much lower speeds ($\sim 200 - 400$ km s^{-1}). These BD shocks can form as the blastwave reaches the walls of the wind-blown cavity, where neutral hydrogen exists, that is created by the progenitor star.

1.2.2 X-ray Spectra

Since core-collapse and type Ia SNe proceed through vastly different processes and progenitors, chemical abundances in the ejecta of SNRs can be used to diagnose the type of SNe that preceded them. Hughes et al. (1995) pioneered this technique with *ASCA* X-ray spectroscopy of SNRs in the LMC. The major diagnostic used is the ratio of oxygen-group elements compared to Si and Fe, which have much greater abundances in core-collapse SNe of massive stars when compared to Ia events (Thielemann et al. 1994; Woosley 1991). For Ia SNe, elements such as Si, S, Ar, Ca, and Fe are more prevalent (Nomoto et al. 1984), which is evidenced in the X-ray spectra of the LMC remnants that are BDRs, which are of Ia origin.

More recently, Yamaguchi et al. (2014a) present a new method of typing SNRs by examining only the Fe Kα spectral line. By determining the centroid of this line, the charge state of the iron is determined using the results from Yamaguchi et al. (2014b). Yamaguchi et al. (2014a) then determine the charge state for various Ia explosion models using one-dimensional hydrodynamic simulations and find that Ia SNRs fall within a range of charge states, which are less than 20. The core-collapse remnants show Fe Kα with higher charge states, which could be due to the iron being stratified at different radii for Ia remnants and/or the higher density into which the reverse shock plows.

1.2.3 Supernova Remnant Morphology

Other observations in the X-ray regime have revealed another method that has proved useful in constraining the type of a SNR. Lopez et al. (2009b) showed that the X-ray morphologies of SNRs can be used to type them. This is accomplished using a multipole power-ratio technique that diagnoses the symmetry of a SNR. Using SNR W49B, a core-collapse remnant, as a test case, Lopez et al. (2009b) find that iron abundances are stratified in a highly asymmetrical distribution in the remnant compared to lighter elements.

This technique is then used in Lopez et al. (2009a) to examine the symmetry of 17 SNRs,

with roughly half of the remnants being in the LMC and half being Galactic. The authors find a clear separation of the symmetry between remnants that are thought to be of Ia origin and those that are formed from core-collapse SNe. Lopez et al. (2009a) conclude that Type Ia SNe produce statistically more symmetric SNRs than those created as a result of core collapse SNe. This approach is in agreement with the theory that Type Ia SNe expand into a constant-density partially neutral ambient medium, whereas the core collapse SNe expand into a more complicated ambient medium that has been altered by the strong stellar winds and outbursts of the progenitor before it explodes. This is also consistent with the picture that core-collapse SNe explode with a high degree of asymmetry, sometimes referred to as a "barrel-like" symmetry (Wang & Wheeler 2008).

Peters et al. (2013) use this technique to type remnants using the *Spitzer Space Telescope* MIPS 24 μm band where we see infrared continuum emission from heated dust to an almost identical selection of remnants explored in Lopez et al. (2009a). The main finding here is that the IR emission shows the same pattern as the X-ray emission morphologies, with the Ia remnants being statistically more symmetric than the remnants formed from core-collapse SNe. The explanation proposed for this difference in symmetry is, again, the difference in environmental conditions into which these SNe explode, as well as the differences in the physics of the explosions themselves.

1.2.4 Light Echo Measurements

Another way of typing remnants is to observe the light from the explosion long after it happens. This technique was proposed by Zwicky (1940) and can be accomplished by looking for systems of light echoes that expand from a central location of a known SNR. These light echoes are formed when the light from the original explosion interacts with a sheet of dust where the light is scattered. Since the light has traveled a larger distance than the rays directed at us at the time of the SN, it can be observed as it was at the time of the explosion until the echoes run off the edge of the sheet.

Rest et al. (2005a) found several light echo complexes that originated from known locations of SNRs (including SN 1987A) in the LMC whilst conducting a microlensing survey of our satellite galaxy (Rest et al. 2005b). The proper motions of these light echoes also allowed Rest et al. (2005a) to date three LMC remnants that had not been recorded historically, where the major uncertainty of these measurements is the unknown inclination of the dust sheet.

The natural next step following the discovery of the light echoes of SNe is to take spectra of these events in order to type the explosion in the typical way. Rest et al. (2008) did just that and found the SNR 0509−67.5 was an overluminous Ia event like SN 1991T. This technique has been used more recently to confirm the SN type of the SNR N103B originally proposed by Hughes et al. (1995), which has also been found to be of Ia origin (A. Rest in preparation: as reported in Williams et al. (2014)).

1.3 Observational Evidence of Efficient Cosmic Ray Acceleration in Supernova Remnants

Observations of SNRs may also help to understand the nature of high energy cosmic rays (CRs). It has been long thought that SNRs are the source of cosmic rays up to the "knee" of the cosmic ray spectrum at an energy of 10^{15} eV (Axford 1981; Blandford & Eichler 1987). SNRs are the most likely source of these high energy particles since they need only to lose 10-20% of their energy to the production of cosmic rays to explain the flux that is detected (Ginzburg & Syrovatskii 1964).

The shock waves of remnants are the most likely source for the acceleration of these cosmic rays since the ambient magnetic fields are highly compressed. Unlike terrestrial shocks, the mean-free-path of particle-particle collisions is on the order of parsecs, meaning the shock waves are instead governed by electromagnetic interactions. This process of acceleration is the first-order Fermi mechanism. The likely location of the acceleration is at the forward shock of the remnant where ambient magnetic field lines are highly compressed

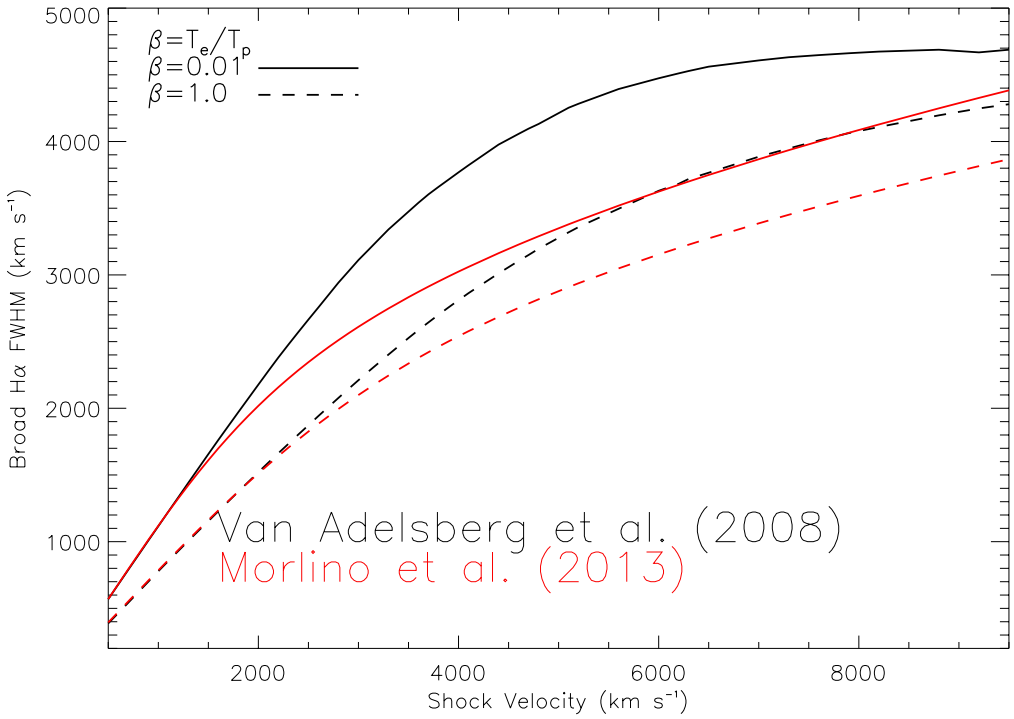

Figure 1.3 Hα broad line width vs. shock velocity for the Balmer shock models of van Adelsberg et al. (2008) in black and the models of Morlino et al. (2013a) in red. Solid curves are shown for $\beta = 0.01$ and dashed curves for the case of full temperature equilibration ($\beta = 1.0$).

having a scale length on the order of an ion gyroradius. The reverse shock is not a strong candidate for this process since the magnetic field that is compressed in the shock is diluted greatly as the ejecta expand.

An indirect method of searching for signatures of efficient CR acceleration is to compare the temperature of post-shock electrons and ions. BD shocks are ideal for this task since these systems are more straightforward than shocks with radiative components. In the case of strong J-type shocks with an adiabatic equation of state of $\gamma = \frac{5}{3}$ and shock speeds greater than ~ 1000 km s^{-1}, the temperature of the electrons or protons follows as:

$$T_i = \frac{3}{16}\frac{m_i v_S^2}{k_{\rm B}}, \tag{1.12}$$

where i denotes the particle of interest, $k_{\rm B}$ is the Boltzmann constant, and v_S is the shock speed. Therefore the ratio of the electron to ion temperature, β, can serve as a diagnostic

for colisionless electron heating if the ratio is observed to be greater than the ratio of the electron to proton mass ($\sim .00054$).

In reality, however, this ratio is known to be less that the ratio of the electron to proton mass due to the effects of plasma instabilities and the waves they generate, such as ion acoustic and Langmuir waves (Cargill & Papadopoulos 1988), which propogate parallel to compressed magnetic field lines. In figure 1.3, we show the results of the Balmer shock models of van Adelsberg et al. (2008) (in black) and Morlino et al. (2013a) (in red), where curves of equal β are plotted on the axes of broad Hα line width vs. shock velocity. Neither of these Balmer shock models include the effects of efficient CR acceleration or the effects on the upstream material from a CR precursor.

Even though the equilibration curves of these models diverge at velocities above 2000 km s^{-1}, they can still be used to look for the effects of CR acceleration if the measured Hα broad line width is significantly lower than the values predicted for the case of total temperature equilibration at the shock for a given shock velocity. While this would not be a definitive diagnostic of efficient CR acceleration due to the uncertainties in these models, it would be a compelling piece of evidence of this acceleration if it is corroborated with other observations.

Another tantalizing piece of evidence from BD remnants arises from measurements of the width of the narrow Hα emission line. Smith et al. (1994) used high resolution optical spectroscopy to measure the narrow line width from four BD SNRs in the LMC, and found widths from 30-50 km s^{-1}. These widths are surprisingly large since they would imply a temperature in excess of 10,000 K in the ambient medium, which would mean all of the hydrogen would be ionized if the temperature distribution of the upstream material is purely Maxwellian. This clearly cannot be the case since we observe Balmer emission in these shocks, so the temperature distribution of the upstream material is being modified by an unknown process. One strong possibility is that it is modified by a CR precursor as ions pass back and forth through the shock front, which may explain these anomalously

large line-widths and evidence of asymmetrical wings in the line profiles (Smith et al. 1994; Sollerman et al. 2003a; Heng 2010).

Observations of remnants in the X-rays also point to the possibility of efficient CR acceleration in SNR shocks. Warren et al. (2005) show that there is anomalous compression occurring at the shock front that is evidenced by ratios of the forward shock radius to the contact discontinuity, where the ratio between the forward shock and reverse shock is much smaller than predictions from hydrodynamic simulations of a purely adiabatic gas. This higher degree of compression is possible if a significant portion of post-shock ions are being accelerated and escaping the remnant (Blondin & Ellison 2001).

The most compelling piece of evidence that SNRs efficiently accelerate CRs is the detection of GeV and TeV emission from several remnants. Even this, however, is not a smoking gun on its own, since there are uncertainties in whether these high energy photons are the result of hadronic or leptonic processes. If the process is hadronic, decaying pions (π_0 decays to $2\gamma \sim 98.8\%$ of the time (Eidelman et al. 2004)) are created from the interaction of accelerated ions with the ambient material. This would indicate that these photons result from CRs that are accelerated in SNR shocks. If the process is leptonic, however, low energy photons from sources like the cosmic microwave background are inverse Compton scattered by relativistic electrons in the ionized plasma of the remnant, and hence, are not direct signatures of CRs.

1.4 Identifying Ia SN Progenitor Systems with Supernova Remnants

As stated earlier, a Ia SN is thought to be a thermonuclear detonation of a C/O white dwarf star that accretes mass from a companion star and has its mass pushed towards the Chandrasekhar mass limit (~ 1.4 $M_\odot$). However, the nature of the companion star, and hence the progenitor system, remains contentious.

The two prevailing systems that are thought to give rise to these SNe are called single-degenerate (SD) and double-degenerate (DD) systems (Iben 1997). In the SD picture, the

degenerate white dwarf star accretes mass from either a main-sequence or slightly evolved post main-sequence star. The DD scenario, by comparison, is a system in which two orbiting white dwarf stars have their orbital distance shrink as they emit gravitational waves until they coalesce and push the mass to the critical limit.

In the sections below I will outline the progress that has been made on constraining progenitor systems of SNRs that are of Ia origin. Primarily, I will focus on the searches for leftover companions in the SD picture and observations of SNR shocks that can constrain progenitor systems with models of how the ambient medium may have been modified before the SN event.

1.4.1 Tycho's Supernova Remnant

Ruiz-Lapuente et al. (2004) presented the results of the proper motions of various stars near the geometric center of the remnant. Most of the stars had velocities of typical foreground stars of $\sim$30 km s^{-1}, but these authors found a star with a velocity of $\sim$ 100 km s^{-1}, which they labeled as star "G". They claim this star is the surviving companion of the explosion because of the large proper motion that is presumably imparted to the star at the time of the SN event.

More recently, however, Xue & Schaefer (2015) independently determined the explosion site and found that star G is rejected at the 8.2σ confidence level, but did state that star "O" from the Ruiz-Lapuente et al. (2004) study was a more promising candidate for a progenitor companion since it fell within their 3σ uncertainty circle and also had a relatively high proper motion like star "G".

1.4.2 Supernova Remnant 1006

Schweizer & Middleditch (1980) found an O-type star that they cautiously suggest could be a stellar remnant from the original SN, but later Wu et al. (1983) concluded that the star is in fact behind the remnant and therefore not associated with it. More recently, Kerzendorf

et al. (2012) led a comprehensive study examining the spectra of 78 stars near the center of the remnant and found no giant stars or post main sequence stars in their sample. They also found no evidence of stars with aberrant rotational velocities. The most likely conclusion of this study is that SNR 1006 is likely the result of a DD channel SN.

1.4.3 SNR RCW 86

The SNR RCW 86 is another remnant thought to be formed from a Ia SN, and may have been the historically recorded SN 185 (Clark & Stephenson 1975). Based on *Advanced Satellite for Cosmology and Astrophysics* (*ASCA*) observation of the remnant, Vink et al. (1997) proposed that the SN that formed RCW 86 exploded into a cavity. Using X-ray proper motions Helder et al. (2009), find the shock speed of the northeastern shock in SNR RCW86 to be ~ 6000 km s^{-1}. This speed is anomalously high considering the majority of shocks in the remnant have speeds less than 1000 km s^{-1} (Long & Blair 1990; Ghavamian 1999; Ghavamian et al. 2001).

Badenes et al. (2007) argue that SD models with high-mass progenitor companions would lead to wind-blown bubbles into which remnants would expand. Using hydrodynamic modeling, Williams et al. (2011b) argue that this strange distributions of velocities could be explained if the remnant were expanding into a wind-blown cavity with the site of the SN being off-center of the bubble, where the eastern shock has yet to reach the walls of the cavity that are retarding the shock around the western rim.

1.4.4 Kepler's Supernova Remnant

The typing of Kepler's supernova remnant (Kepler hereafter) has been controversial in the past, but recent evidence all converges on the remnant of being Ia in origin. This has been accomplished by examining the X-ray spectroscopy and morphology, the presence of BD shocks throughout the remnant, and a lack of detection of a pulsar-wind nebula (Burkey et al. 2013). Unlike the majority of Ia remnants that have been observed, Kepler is

expanding into a non-uniform ambient medium. Using a deep *Chandra* observation of the remnant, Reynolds et al. (2007) argue that the ambient medium into which the remnant is expanding is circumstellar in nature by virtue of solar abundances of O/Fe in the shocked ambient medium. Burkey et al. (2013) build upon these results by mapping the spectra of 100 small regions from various parts of the remnant and find that oxygen abundances are small for the majority of the remnant with the exception of a few regions near the rim. This strengthens the case that the remnant is indeed expanding into circumsteller material and that the progenitor companion was likely an asymptotic giant branch star and Sollerman et al. (2003b) found that the socked circumstellar material is moving at a high systematic velocity of 185 km s^{-1} These findings indicate that the progenitor system of the SN that formed Kepler was likely SD.

1.4.5 Supernova Remnant N103B

As previously noted, SNR N103B was originally identified as of Ia origin (Hughes et al. 1995) and confirmed from optical spectroscopy of the light echoes from the original SN event (A. Rest in preparation: as reported in Williams et al. (2014)). This validates the X-ray findings of Lewis et al. (2003), who proposed the remnant was of Ia origin through a detailed analysis of *Chandra* spectra that showed high abundances of Fe and Si and lower abundances of intermediate mass elements. This remnant provides yet another opportunity to constrain the progenitor system of a Ia event. Through IR observations of the dust in this remnant, Williams et al. (2014) find that this remnant is an apparent analogue of Kepler, inasmuch as the evidence suggests that it is expanding into a complicated ambient medium consistent with circumstellar material. This again would point toward the progenitor system being SD in nature, since a DD system would be expanding into a much more quiescent ambient medium, since the timescale of DD mergers is on the order of 10^9 years.

1.4.6 Supernova Remnant 0509−67.5

The LMC remnant 0509−67.5 is yet another remnant to be typed with the spectrum of its light echoes (Rest et al. 2008). Schaefer & Pagnotta (2012) studied this remnant and found the geometric center with three independent techniques. Using the asymmetry seen in the west of the remnant, they displace the explosion site and constrain their search radius using the uncertainties from their geometric center determination, as well as accounting for possible kick velocities that may have been imparted to the progenitor companion in the event that the explosion resulted from a SD system. Schaefer & Pagnotta (2012) conclude that the SD scenario must be ruled out for SNR 0509−67.5 since they find no stars within their 3σ uncertainty circle.

A striking weakness in this study is that no uncertainty was factored into their error circle for their proposed offset of the explosion site, nor was dynamical information used to assess the dynamic asymmetry that can be seen directly in the expansion of the remnant. We will address these problems with our own study in chapter three of this thesis.

1.4.7 Supernova Remnant 0519−69.0

A final example of a Ia remnant being used to diagnose the progenitor system is the LMC remnant 0519−69.0. Though this remnant has not been spectroscopically typed, it is a BDR that suggests it is of Ia origin. The X-ray spectrum of this remnant is also strongly suggestive that the SN was Ia, due to the lack of oxygen-like elements and overabundance of iron-like species (Hughes et al. 1995). X-ray and IR morphologies of the remnant also show a high degree of symmetry, which again suggests the Ia nature of SNR 0519−69.0 (Lopez et al. 2009a; Peters et al. 2013).

Edwards et al. (2012) build upon the techniques of Schaefer & Pagnotta (2012) to diagnose the progenitor system of 0519−69.0. The study finds 27 stars with magnitudes greater than 22.7 within their 3σ uncertainty circle. These stars are possible candidates as supersoft sources in the SD scenario. None of the stars found within their search radius

showed evidence of being evolved main sequence stars, which eliminates the possibility that the progenitor system was a symbiotic binary, recurrent nova, or helium donor system in the SD paradigm. This study is less conclusive than those noted above, since neither the SD or DD progenitor system model can be ruled out.

Chapter 2

A Direct Measurement of the Forward Shock Speed in Supernova Remnant 0509−67.5: Constraints on the Age, Ambient Density, Shock Compression Factor and Electron-ion Temperature Equilibration.

Abstract

Two *Hubble Space Telescope* narrow-band Hα images separated in time by 1.03 years are used for a proper motion measurement of the forward shock of the Large Magellanic Cloud (LMC) supernova remnant 0509−67.5, the only spectroscopically-confirmed LMC remnant of Ia origin. We measure a global shock speed of 6500 ± 200 km s^{-1} and constrain the pre-shock neutral hydrogen density to be 0.084 ± 0.003 cm^{-3}, for a typical mean number of Hα photons produced per neutral hydrogen atom entering the forward shock. Previously published broad Hα line widths from two locations on the rim and our corresponding shock speed measurements are consistent with Balmer shock models that do not include effects of cosmic ray acceleration. For the northeastern rim location, we limit the post-shock electron temperature to 10% of the proton temperature by also using the broad-to-narrow flux ratio. Hydrodynamic simulations for different initial ejecta density profiles constrain the age and ambient medium density; for an exponential ejecta profile and initial explosion energy of 1.4×10^{51} erg, the remnant's age is 310^{+40}_{-30} years. For all evolutionary models explored, the expansion parameter falls in the range 0.41 to 0.73, indicating that the remnant is still firmly in the ejecta-dominated phase of its evolution. Our measured neutral hydrogen density of the ambient medium, combined with the shocked density obtained in Williams

et al. (2011a), disfavors forward shock compression factors greater than ~ 7.

2.1 Introduction

Ranking among the most energetic of astrophysical events, supernovae result from either the core-collapse of a massive star or from a white dwarf whose mass is pushed toward the Chandrasekhar limit and ignites as a thermonuclear explosion. The latter of these supernovae are known as Ia events and yield optical spectra showing prominent silicon lines along with an absence of hydrogen spectral lines. Remarkably homogeneous in their spectra and light curves, Ia supernovae provide distance measurements that help to constrain cosmological models and their parameters (Riess et al. 1996, 1998; Perlmutter et al. 1999). Radioactive decay of ^{56}Ni and subsequently ^{56}Co to ^{56}Fe powers the light curves of Ia supernovae (Colgate & McKee 1969). Eventually the light curve fades and, as the evolution proceeds, the majority of photons observed result from the interaction of high Mach-number shocks that are driven into the interstellar medium (ISM) by the expanding ejecta. This transition signals the onset of the supernova remnant phase of evolution. Supernovae can be studied for typically months to years before they fade into obscurity, while a supernova remnant can be studied for thousands of years, allowing a second look into their stellar corpses and a fresh view into the impact of SN explosions on the surrounding medium.

Though viewed in less detail than Galactic supernova remnants (SNRs), remnants in external galaxies like the Large Magellanic Cloud (LMC), offer an excellent opportunity to study their kinematics with great accuracy since the distances to their host galaxies are usually well known, unlike the generally poor distance determinations to their Galactic brethren. Of the young remnants of Ia origin, SNR 0509−67.5 serves as an excellent example of a young SNR that is driving collisionless shocks into the ISM. 0509−67.5 was discovered as an X-ray source by the *Einstein Observatory* (Long et al. 1981) and confirmed as a supernova remnant by Tuohy et al. (1982) where the remnant was shown to exhibit a

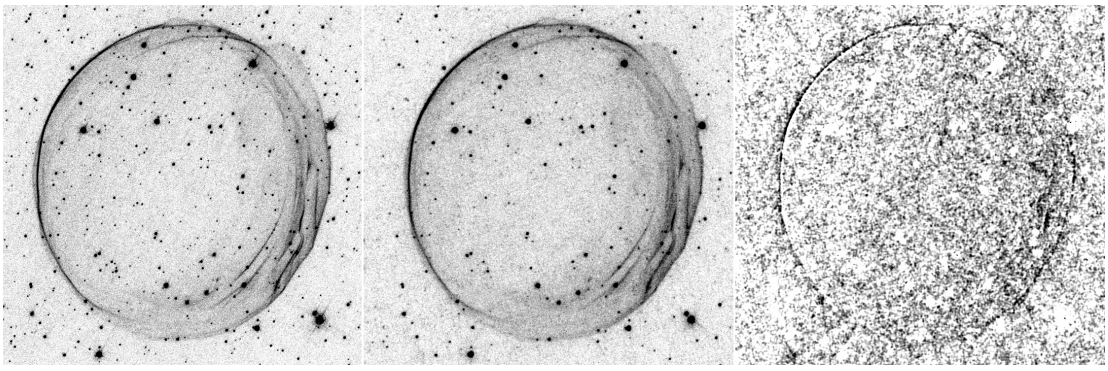

Figure 2.1 *Left* - The first epoch Hα image of 0509−67.5, obtained by the ACS aboard *HST* and drizzled with a pixel scale of 0.05″ pixel^{-1}. *Center* - The second epoch observation of 0509−67.5, taken about a year later, imaged on the WF chips of the WFPC2 aboard *HST* and drizzled with the same pixel scale. *Right* - The difference image, generated by scaling the ACS and WFPC2 images using an average relative intensity factor (see §2.3.1) and blurring the ACS image to match the poorer PSF of the WFPC2 image. The color scale is set so that areas into which the shock has expanded over the course of a year are shown in black.

pure hydrogen line spectrum with no forbidden line emission, identifying it as a Balmer-dominated (BD) remnant. Several Galactic remnants thought to be of Ia origin are also BD, hence it was suggested that 0509−67.5 was of Ia origin by analogy. A Ia origin was indicated in a number of other ways, starting with Hughes et al. (1995), who found that the X-ray spectrum obtained from the *Advanced Satellite for Cosmology and Astrophysics* was consistent with a Ia event due to the prominent emission from silicon, sulfur, argon, calcium and especially iron. Later Warren & Hughes (2004) showed using *Chandra X-Ray Observatory* data from the *Advanced CCD Imaging Spectrometer* (ACIS) that the ejecta abundances for O through Ca derived from the X-ray spectrum were consistent with nucleosynthesis predictions for delayed-detonation Ia explosion models. The discovery of light echos by Rest et al. (2005a) provided an age of 400 ± 120 years for 0509−67.5, where the primary source of uncertainty lies in the unknown inclination of the dust sheet, off which the light scatters. The definitive classification came subsequently from optical spectra of the light echoes, that showed the explosion to be a Ia and likely in the class of over-luminous explosions like SN 1991T (Rest et al. 2008).

Optical emission of the supernova remnant is due to BD shocks whose spectra exhibit

both a broad and narrow component. The broad component arises from charge exchange between neutral hydrogen from the cold ambient medium and hot post-shock protons, while the narrow component results from the collisional excitation of the cold neutrals by shock-heated ions and electrons. Measurements of the intensity ratio of the broad and narrow Hα lines, along with the width of the broad Hα component can be used to constrain the velocity of the forward shock of the remnant (Chevalier & Raymond 1978; Chevalier et al. 1980).

Tuohy et al. (1982) were unable to detect a broad component to the Hα line in 0509−67.5, and later Smith et al. (1991) also came up with a non-detection, but quoted a lower limit on the shock velocity of 2000 km s^{-1}. Ghavamian et al. (2007) detected a broad component to the Lyβ line in the UV with the *Far Ultraviolet Spectroscopic Explorer*, from which they estimated a shock velocity of 3600-7100 km s^{-1}. Helder et al. (2010) were able to detect both a broad and narrow component to the Hα line using the Focal reducer and low dispersion spectrograph (FORS2) on the Very Large Telescope (VLT), and estimated the global forward shock velocity to be 6700 ± 400 km s^{-1}.

Supernova remnants are thought to be a dominant producer of cosmic rays up to the "knee" in the cosmic ray spectrum at an energy of $\sim 10^{15}$ eV (Axford 1981; Blandford & Eichler 1987). BD shocks are typically fast shocks expanding into low density media where the mean free path for proton-proton collisions is on the order of parsecs (Heng 2010); these shocks are therefore likely moderated by the ambient magnetic field where particles can also be accelerated to relativistic energies through the first-order Fermi mechanism (Bell 1978; Blandford & Ostriker 1978; Reynolds & Chevalier 1981). The efficiency of this acceleration process can be high enough to have profound consequences on the dynamics of the forward shock, one manifestation of which appears as an increase in the shock compression factor, C_γ, which depends on the adiabatic index γ as $C_\gamma = \rho_S/\rho_0 = (\gamma + 1) / (\gamma - 1)$. For a shock that accelerates cosmic rays efficiently, the effective adiabatic index can drop below the nominal value of $\gamma = 5/3$ due to the effects of relativistic particle pressure (where $\gamma = 4/3$

is expected) and the escape of particles from the shock. As the effective adiabatic index decreases the compression factor increases (Ellison & Eichler 1984; Blondin & Ellison 2001), and the overall shock velocity and radius will be less than that of a shock with a greater effective γ at the same age.

In this work we measure the proper motion of the forward shock in 0509−67.5, resulting in the first direct measure of the velocity of the blast wave in this remnant. The key observational data set is a pair of Hα *HST* images taken at two different times separated by about a year. Armed with accurate values for the remnant's current radius and shock velocity, we use numerical hydrodynamic simulations to constrain the age and ambient medium density. We explore how different initial ejecta profiles (e.g., Chevalier 1982; Dwarkadas & Chevalier 1998), effective adiabatic indices, and initial explosion energies modify the derived evolutionary parameters. We use our measurements of the Hα intensity to determine the ambient neutral hydrogen density. This value, plus the shocked hydrogen density estimate from Williams et al. (2011a), allow us to further restrict the allowed evolutionary solutions for the SNR.

The structure of this paper is as follows. Section 2.2 describes our *HST* observations and relevant data reduction. Proper motion measurements of the forward shock of 0509−67.5 are given in section 2.3. Section 2.4 addresses the issue of temperature equilibration between ions and electrons in the post-shock region through comparison of our shock velocities with the spectroscopic data from Helder et al. (2010). In §2.5 we present our hydrodynamic simulations of 0509−67.5, which we use to place constraints on the age, the density of the ambient ISM, and the compression ratio in the forward shock. Conclusions are in §2.6. We assume a distance to the LMC of 50 kpc with an uncertainty of 4% (Clementini et al. 2003). Uncertainties are quoted at the 1-σ (68.3% confidence level) unless stated otherwise.

2.2 Observations and Data Reduction

Our first epoch imaging observation (Figure 2.1 – left panel) was taken with the *Advanced Camera for Surveys* (ACS) Wide Field Camera (WFC) on 2006 October 28 through the F658N Hα filter for a total exposure time of 4620 seconds under *HST* Program number 11015 (PI: J. Hughes).[1] With two 4096 $\times$ 2048 CCDs, the WFC covers an effective 202$''$ $\times$ 202$''$ field of view; the remnant was centered on one of these chips. Standard pipeline processing for the ACS (CALACS) applied flat fielding, bias, and dark current corrections to the raw data. We use the *Space Telescope Science Data Analysis Software* (STSDAS) task `multidrizzle` to combine the dithered, cosmic ray (CR) split frames and apply the geometric distortion corrections to produce the final frame shown in Figure 2.1, which has a pixel scale of 0.05$''$ per pixel. The inverse of the weight map produced by `multidrizzle` (with error weighting selected) is taken as the variance map for the ACS data.

ACS failed a few months after this observation. Our program was allocated additional orbits to carry out the second epoch observation on the Wide Field Planetary Camera 2 (WFPC2). This observation was executed on 2007 November 7 using the F656N Hα filter for an integrated exposure time of 14310 seconds. The target was placed on two different Wide Field camera chips (numbers 2 and 3) in order to reduce streaking due to charge transfer inefficiency (CTI). Once again we use `multidrizzle` to combine the data, 12 dithered frames, onto an image with a pixel scale of 0.05$''$ per pixel. The resulting image is similar to the first epoch one, albeit with somewhat poorer spatial resolution (see Figure 2.1 – middle panel).

In order to measure the expected sub-pixel shifts of the shock front, all individual frames of each epoch, plus the two epochs themselves, are registered to a common coordinate frame using the stellar field. Standard IRAF packages (`daofind`, `xyxymatch`, and `geomap`) are used to identify stars in the several frames, find stars common to each observation, and compute

[1]Based on observations made with the NASA/ESA Hubble Space Telescope, obtained at the Space Telescope Science Institute, which is operated by the Association of Universities for Research in Astronomy, Inc., under NASA contract NAS 5-26555.

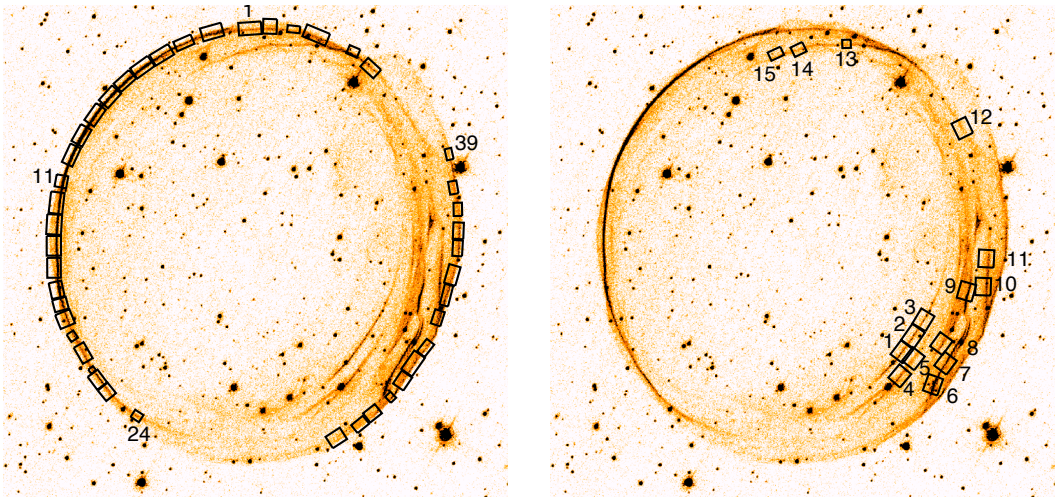

Figure 2.2 Left - The first epoch ACS image of 0509−67.5, showing the 44 rectangular extraction apertures along the exterior rim used to measure the remnant's global shock speed. The regions are labeled numerically starting from the north and increasing in the counterclockwise direction. Right - Same as the image to the left except that here we show the interior extraction apertures.

a final solution for registration allowing for shifts in both the x and y directions, a rotation angle, and different native pixel scales.

Since the native pixel size for WFPC2 is 0.1″, twice that of the ACS WFC data, the point-spread-function (PSF) of the ACS data had to be degraded to match that of the WFPC2 image. With the epochs properly registered, we use the IRAF task `psfmatch` for this. We select 100 unsaturated stars close to the remnant that were imaged in each of the WF chips 2 and 3 on which the remnant was imaged. Further iterations of `daofind`, `xyxymatch`, and `geomap`, as described in the previous paragraph, ensure proper registration between the WFPC2 and convolved ACS data. The final registration of the two epoch images has a R.M.S. uncertainty of 0.0039″ and 0.0055″ in the W-E and N-S axis respectively; this represents the uncertainty for a given star.

In order to provide accurate absolute positions from the ACS data in a standard astrometric reference frame, we register the ACS image to the LMC microlensing catalog (Rest et al. 2005b), which has an astrometric uncertainty of 0.03″ (Alcock et al. 2001), using the same techniques as described above.

2.3 Proper Motion Measurement

Our two *HST* narrow-band images of 0509−67.5 are separated by a time baseline of 375 days ($\sim$ 1.03 years). Even on this short time period, the remnant's expansion is notable, as can be seen in the difference image (Figure 2.1 – right panel).

We measure the proper motion of Hα filaments at numerous azimuthal locations around the remnant. We begin by defining rectangular apertures, aligned (by eye) to be tangent to the shock front at the rim (Figure 2.2). Apertures are chosen to be short enough along the shock front direction that the shock can be treated locally as a straight line segment. Apertures are non-overlapping and avoid obvious stars. In addition, we limit ourselves to apertures where the signal-to-noise ratio of the extracted Hα profiles in the WFPC2 data is relatively high ($\geq$ 10 for the brightest bin and $\geq$ 150 for the total profile) in order to ensure a statistically significant proper motion measurement. The background or sky level is estimated for each aperture using a nearby source-free region beyond the remnant's rim.

One set of apertures covers the exterior rim of bright Hα emission (Figure 2.2 – left panel) and are used to determine the global shock speed of 0509−67.5. Another set covers interior shock filaments (Figure 2.2 - right panel). Unlike the case of the exterior filaments, where the proper motion accurately traces the shock speed, the interior filaments suffer from unknown projection effects for which proper motions only provide lower limits on their shock velocities.

2.3.1 Outer Regions

We start by extracting 1-D Hα brightness profiles (summed along the shock front) from the 44 regions around the rim in both images. Figure 2.3 shows the Hα profiles in counts per 1000 seconds (cpks) extracted from selected regions (see Figure 2.2) as examples, with the first epoch ACS data shown in black (dot-dashed linetype), and the second epoch WFPC2 data in red.

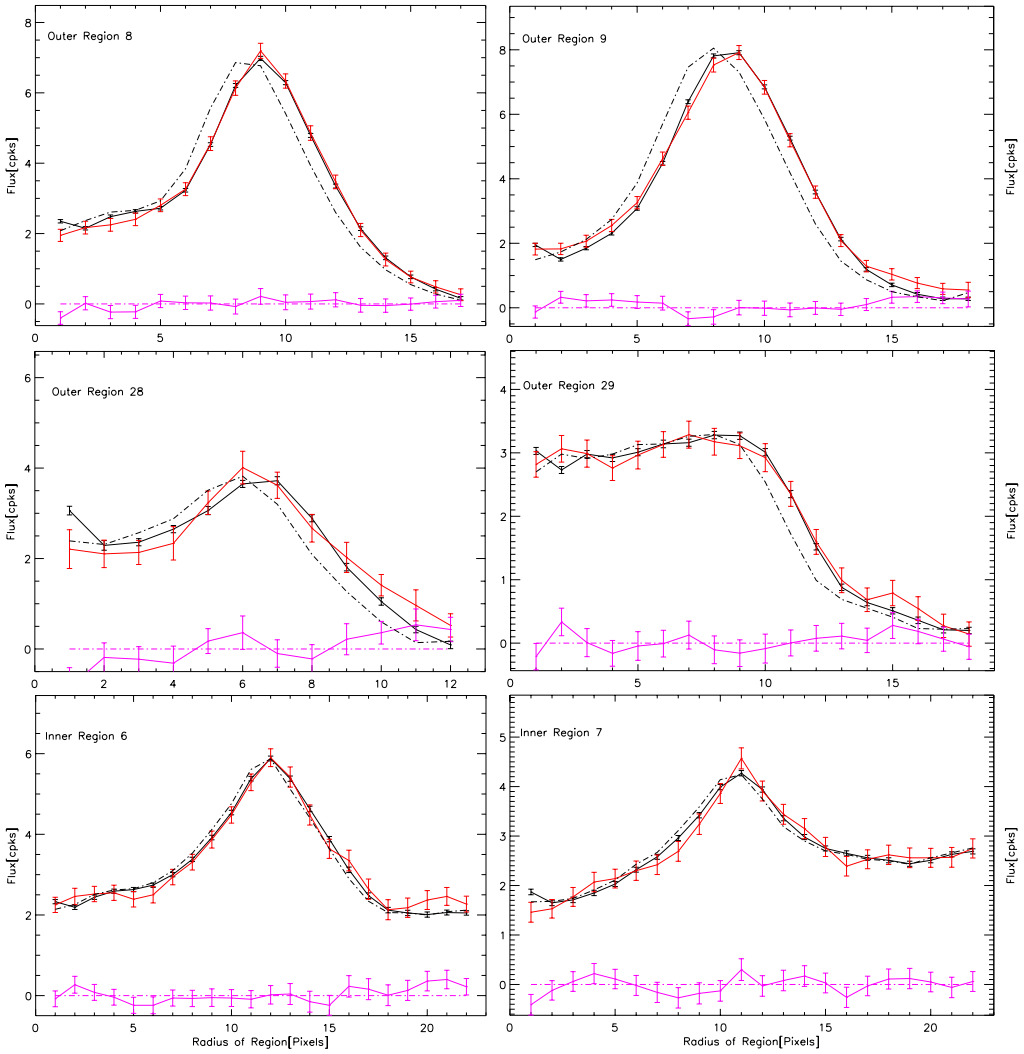

Figure 2.3 1-D spatial profiles of Hα flux for six extraction apertures, 4 from the outer rim and 2 from interior filaments as labeled. In each panel the dot-dashed black line is the Hα brightness profile extracted from the first epoch ACS image and scaled to the WFPC2 profile. The solid black line shows the shifted brightness profile of the ACS image where χ^2 is minimized. Data points and uncertainties for the second epoch profile are shown in red. The purple points show the residuals and combined uncertainties from the subtraction of the WFPC2 profile and the shifted and scaled ACS profile.

Since the signal-to-noise and the PSF are superior in the first epoch image, we treat the Hα profiles from these data as our "model" profiles, which we compare to the corresponding second epoch data, which we treat as our "data" profiles. We employ cubic convolution interpolation on the "model" profiles from the first epoch to shift the model data, M_i, in position; for each shifted profile the model data are normalized to the profile for our data (D_i) by the value R (defined below).

At each shifted position we use a modified χ^2 statistic, which serves as our figure-of-merit function for comparing the shifted and rescaled model Hα profile to the WFPC2 data profile. We define our modified χ^2 as,

$$\chi^2 = \sum_{i=1}^{N} \frac{(D_i - M_i R)^2}{\sigma_{D_i}^2 + \langle R \rangle^2 \sigma_{M_i}^2}, \tag{2.1}$$

where $\langle R \rangle = \sum D / \sum M$ and,

$$R = \sum_{j=1}^{N} \frac{M_j D_j}{\sigma_{D_j}^2 + \langle R \rangle^2 \sigma_{M_j}^2} / \sum_{j=1}^{N} \frac{M_j^2}{\sigma_{D_j}^2 + \langle R \rangle^2 \sigma_{M_j}^2}. \tag{2.2}$$

For simplicity we assume an average profile scaling factor $\langle R \rangle$ for the error term, which is dominated anyway by the uncertainties in the second epoch "data" profile. Equation 2, which is the analytic minimization of Eqn. 1, allows for some freedom in the precise value of R where it matters most for the fit, i.e., in the difference between the profiles. In practice we find that the values of $\langle R \rangle$ and R are nearly identical (~ 5) for all 44 profiles.

In Figure 2.3 in addition to the raw profiles, we also plot the shifted model profile (solid black) and the residuals (purple) for the best fit value of R. The residuals are generally flat with no systematic trends.

The shock location as a function of azimuth around the rim is another observable that we extract from the ACS image. Ideally the forward shock position would be identified by finding where the emission fades to the sky level, but this measurement is biased by PSF blurring. To minimize this effect, we estimate the shock location using the following method. We determine the radial position of the peak surface brightness $R_{\max}$ and also the

position where the flux drops to half the peak value ($R_{1/2}$) going out in radius. A simple spherical shell profile allows us to extrapolate to the location of the forward shock $R_{\rm FS}$ using the expression $R_{\rm FS}^2 = (4\,R_{1/2}^2 - R_{\rm max}^2)/3$. We approximate the uncertainty on the shock positions generously to be $\sigma_R = R_{\rm max} - R_{1/2}$.

The R.A. and decl. positions of the shock location in each aperture were fitted to an ellipse, weighting by the inverse variance of the radial positional uncertainty. This locates the remnant's geometric center at 05:09:31.086 ,−67:31:16.90; the best-fit ellipse has a semi-major (semi-minor) radius of $15.5''(14.5'')$ with the major axis aligned at position angle 8.6°. We use the root-mean-square radial residual between the measured position and the ellipse model fit, $0.15''$, as our estimate for the uncertainty of the geometric center. This fit is in good agreement with the one reported in §3.2 of Warren & Hughes (2004), which fitted an ellipse model to the *Chandra* X-ray image. It also agrees well with the geometric center quoted by Schaefer & Pagnotta (2012).

Table 2.1 provides the region number and position angle for each of the 44 regions along the exterior rim in columns 1 and 2, the best-fit numerical values for the forward shock radius in column 3 and in column 4 the angular shift (outward-going radial shifts are quoted as positive) required to match the profiles. All of the shifts are positive, that is directed outward with respect to the remnant's center. Given the simplicity of the fits (for example, we assume the sky level underlying each profile is uniform, which ignores any stellar contamination), the fits are generally acceptable according to the minimum χ^2 values we quote (column 5) for the number of degrees of freedom (column 6) in each fit. Statistical errors on the shift values were determined from the fits using the usual $\Delta\chi^2 = +1$ criterion. Systematic errors on the proper motion were derived from R.A and Dec. registration uncertainties (which were slightly different) reduced by the square root of the number of effective PSF widths spanning the extraction region along the shock front (typically 5).

Table 2.1. Proper Motion Measurements for Outer Regions

Region	PA[deg]	Radius [″]	Shift [mas](± stat.± sys.)	χ^2	d.o.f.	V_b [km/s](± stat.± sys.)
1	1.7	15.3 ± 0.10	24.5 ± 5.35 ± 1.97	16.5	17	5760 ± 1256 ± 464
2	12.0	15.5 ± 0.17	27.0 ± 3.35 ± 2.01	32.3	18	6340 ± 786 ± 472
3	20.1	15.3 ± 0.11	32.0 ± 5.04 ± 2.14	12.9	14	7520 ± 1183 ± 503
4	26.9	15.1 ± 0.12	30.5 ± 3.75 ± 1.99	16.8	16	7170 ± 881 ± 467
5	33.3	15.0 ± 0.15	36.5 ± 3.12 ± 1.97	16.2	17	8570 ± 734 ± 463
6	39.5	15.0 ± 0.14	27.0 ± 2.37 ± 2.02	14.9	15	6340 ± 556 ± 474
7	45.5	14.9 ± 0.12	27.0 ± 2.11 ± 2.03	6.6	17	6340 ± 496 ± 477
8	52.1	14.8 ± 0.14	29.0 ± 2.48 ± 1.97	10.3	16	6810 ± 583 ± 464
9	59.0	14.8 ± 0.15	32.0 ± 2.26 ± 2.02	23.3	17	7520 ± 530 ± 476
10	65.2	14.7 ± 0.11	31.0 ± 1.91 ± 1.96	30.0	15	7280 ± 449 ± 461
11	73.1	14.6 ± 0.13	32.5 ± 2.99 ± 2.50	15.6	16	7630 ± 702 ± 588
12	79.3	14.5 ± 0.14	26.5 ± 2.57 ± 1.89	18.6	18	6230 ± 604 ± 443
13	85.5	14.5 ± 0.13	22.0 ± 3.14 ± 1.95	8.5	20	5170 ± 736 ± 458
14	91.5	14.5 ± 0.12	25.5 ± 2.88 ± 1.96	19.8	19	5990 ± 675 ± 461
15	97.7	14.6 ± 0.16	25.0 ± 3.58 ± 1.95	17.3	18	5870 ± 841 ± 459
16	103.9	14.7 ± 0.14	33.0 ± 5.05 ± 2.18	24.5	17	7750 ± 1186 ± 511
17	108.1	14.8 ± 0.21	38.0 ± 5.68 ± 2.51	26.3	19	8930 ± 1336 ± 588
18	112.3	15.0 ± 0.28	26.0 ± 5.94 ± 2.28	13.9	21	6110 ± 1395 ± 535
19	117.5	14.8 ± 0.13	28.5 ± 13.47 ± 3.03	9.3	10	6700 ± 3164 ± 711
20	123.0	14.9 ± 0.12	29.5 ± 5.87 ± 2.07	17.0	15	6930 ± 1378 ± 486
21	128.3	15.0 ± 0.09	17.5 ± 11.05 ± 3.87	2.3	7	4110 ± 2596 ± 909
22	131.2	15.1 ± 0.16	26.0 ± 4.68 ± 2.24	22.3	17	6110 ± 1098 ± 526
23	135.4	15.3 ± 0.17	18.5 ± 5.39 ± 2.44	21.5	17	4350 ± 1266 ± 574
24	145.8	15.3 ± 0.14	17.0 ± 8.74 ± 2.94	2.6	11	3990 ± 2052 ± 690
25	202.1	15.5 ± 0.12	30.5 ± 8.00 ± 2.24	21.0	18	7170 ± 1879 ± 526
26	209.5	15.3 ± 0.27	21.0 ± 8.51 ± 2.36	8.7	14	4930 ± 1998 ± 554
27	213.9	15.2 ± 0.14	25.5 ± 8.03 ± 2.37	13.5	16	5990 ± 1886 ± 556
28	220.6	14.9 ± 0.11	35.0 ± 7.89 ± 3.34	14.8	11	8220 ± 1854 ± 784
29	226.2	14.7 ± 0.16	37.5 ± 8.29 ± 2.25	8.8	17	8810 ± 1947 ± 530
30	231.9	14.5 ± 0.12	29.0 ± 5.51 ± 1.88	25.5	18	6810 ± 1294 ± 442
31	237.6	14.5 ± 0.12	19.0 ± 7.13 ± 2.27	6.3	13	4460 ± 1675 ± 532

Table 2.1 (cont'd)

Region	PA[deg]	Radius [″]	Shift [mas](± stat.± sys.)	χ^2	d.o.f.	V_b [km/s](± stat.± sys.)
32	246.9	14.4 ± 0.15	27.0 ± 5.49 ± 2.28	15.4	13	6340 ± 1289 ± 536
33	254.0	14.3 ± 0.15	25.0 ± 5.43 ± 1.90	9.9	11	5870 ± 1274 ± 447
34	260.0	14.5 ± 0.14	20.5 ± 5.97 ± 1.99	7.6	16	4820 ± 1401 ± 468
35	267.8	14.7 ± 0.12	16.5 ± 5.47 ± 2.18	23.6	13	3880 ± 1285 ± 513
36	272.8	14.7 ± 0.14	35.5 ± 5.76 ± 2.14	14.0	14	8340 ± 1354 ± 503
37	278.8	14.9 ± 0.16	28.0 ± 7.87 ± 2.39	4.2	11	6580 ± 1848 ± 563
38	285.1	14.9 ± 0.15	32.5 ± 8.08 ± 2.43	3.8	11	7630 ± 1897 ± 570
39	294.1	15.3 ± 0.12	19.5 ± 8.76 ± 2.59	6.5	9	4580 ± 2058 ± 609
40	326.4	15.1 ± 0.11	18.0 ± 4.16 ± 2.16	18.4	16	4230 ± 977 ± 508
41	332.9	15.2 ± 0.11	24.5 ± 8.05 ± 2.76	9.6	12	5760 ± 1890 ± 647
42	343.7	15.4 ± 0.17	25.0 ± 4.56 ± 1.87	20.5	17	5870 ± 1071 ± 439
43	350.0	15.5 ± 0.14	21.0 ± 10.01 ± 2.64	4.1	9	4930 ± 2350 ± 620
44	356.4	15.7 ± 0.30	15.5 ± 7.00 ± 2.54	22.1	20	3640 ± 1643 ± 596

Note. — The uncertainties in the radii are defined as $R_{max} - R_{1/2}$. Best fit values of the shift and shock speed for each extraction aperture are followed by their 1σ statistical and systematic uncertainties, respectively.

Figure 4 plots the expansion velocities as a function of position angle around the exterior rim. The uncertainties plotted include both statistical and systematic errors (root-sum-squared). We find that the expansion rates are consistent with a single global shock speed of 6500 ± 200 km s^{-1}, with a reduced χ^2 of ~ 1.1. Taking the eastern and western halves separately yields expansion velocities of 6600±200 km s^{-1} and 5800±400 km s^{-1}, respectively, that are generally consistent with the single global shock speed just quoted. We investigated how sensitive the global expansion rate is to the by-eye alignment of the individual extraction regions to the shock tangent; we find no significant bias in the global expansion rate for random rotations of the extraction apertures up to 5° (which are easily seen to be non-optimal).

2.3.2 Interior Regions

In addition to the outermost rim of Hα emission, we also measured the proper motions of a number of bright, isolated, thin filaments located within the interior of the remnant. The low S/N of the WFPC2 data limited us to the several regions shown in Figure 2.2 (right panel). The numbering scheme used here follows individual filaments consecutively (e.g.,

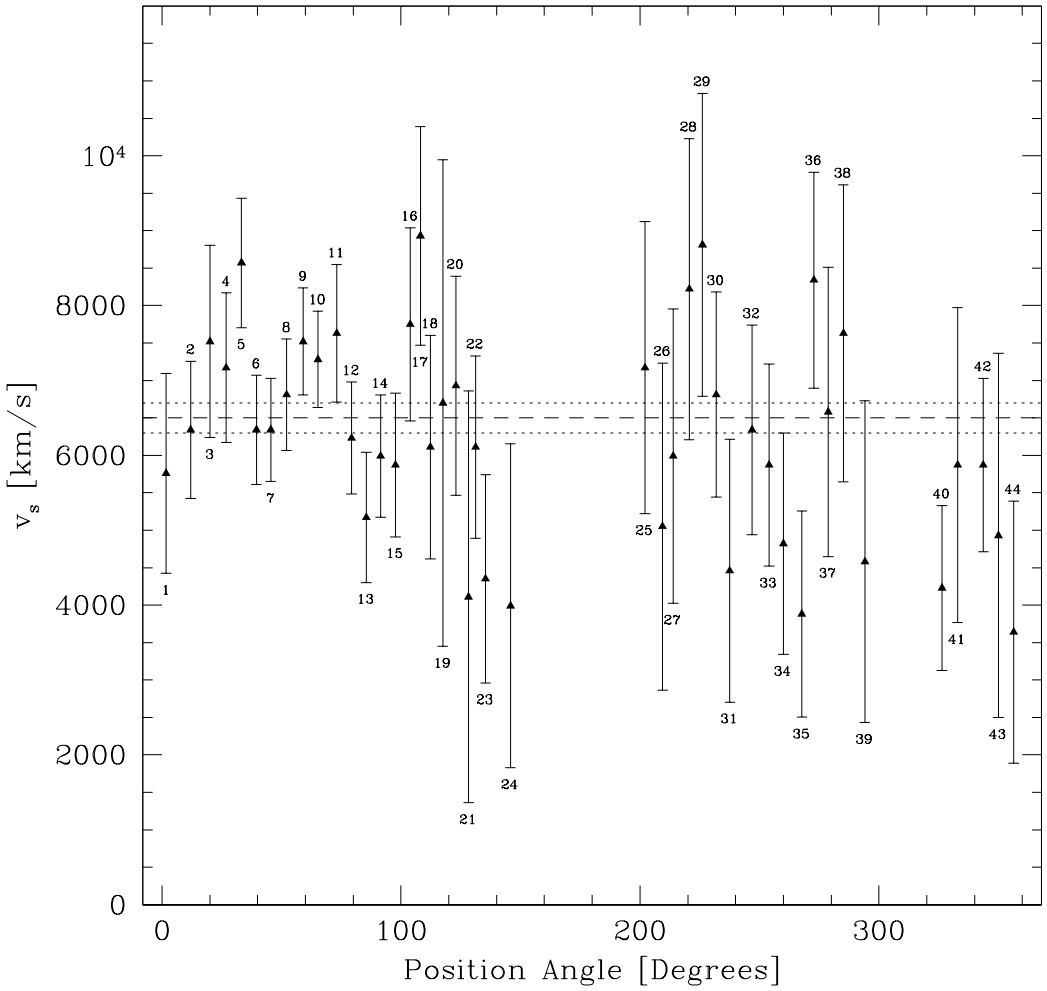

Figure 2.4 Expansion velocity vs. position angle for the 44 Hα profiles we consider. Each point is labeled with its corresponding identification number. The global average velocity and $\pm 1\sigma$ uncertainty range are shown with a dashed line and dotted lines respectively.

regions 1, 2, & 3 are on one filament; 4 & 5 on another, and so on). Example Hα brightness profiles for two interior regions are given in the bottom two panels of Figure 2.3.

The same techniques as described in §2.3.1 are used to determine the radial shifts of the inner filaments; values and uncertainties are given in Table 2.2. Here we do not convert angular expansion rates into physical velocities since these interior filaments likely suffer from unknown projection effects. Our selection of interior filaments includes those that coincide with the VLT FORS2 slit location at the southwest (SW) rim of 0509−67.5 from Helder et al. (2010). This portion of the rim exhibits considerable more sub-structure than elsewhere in the remnant. Helder et al. (2010) reported the width of the broad Hα component and broad-to-narrow intensity ratio for this region, which they interpreted assuming a simple single shock geometry. In §2.4 below, we re-examine their conclusions in the light of the complexity of the SW rim guided by our proper motion measurements of both the interior and exterior filaments.

2.3.3 Ambient Density

In BD shocks it is possible to estimate the ambient medium density from the flux of the Hα emission, which, for face-on shocks, goes as $I_{\mathrm{H}_\alpha} \sim (1/4\pi)\, n_{H_0} v_{\mathrm{s}} h\nu_{\mathrm{H}_\alpha} \epsilon_{\mathrm{H}_\alpha}$(Chevalier & Raymond 1978; Raymond 1991; Heng 2010), where $v_{\mathrm{s}} n_{H_0}$ is the flux of neutral hydrogen atoms entering the forward shock, $h\nu_{\mathrm{H}_\alpha}$ is the energy of an Hα photon ($\sim$ 1.9 eV), and $\epsilon_{\mathrm{H}_\alpha}$ is the probability that a hydrogen atom in the post-shock flow will emit an Hα photon before being ionized. For our estimate here, we assume $\epsilon_{\mathrm{H}_\alpha} = 0.2$ (Chevalier et al. 1980; Michael et al. 2003; Heng & McCray 2007).

We extract the Hα flux from a circular region of radius 8″ centered near the middle of the remnant in order to stay close to a face-on configuration, using a stellar mask to avoid emission from stars. To ensure the most accurate flux measurement, we use the unconvolved ACS image of the remnant.

Using the `synflux` routine from the `STSDAS SYNPHOT` package, we measure an Hα flux

Table 2.2. Proper Motion Measurements for Inner Regions

Region	PA[deg]	Radius [″]	Shift [mas](± stat.± sys.)	χ^2	d.o.f.	$\dot{\theta}$ [mas yr^{-1}](± stat.± sys.)
1	221.4	10.8 ± 0.11	23.5 ± 4.87 ± 2.15	31.4	21	24.1 ± 4.99 ± 2.21
2	228.8	10.6 ± 0.11	8.5 ± 6.26 ± 2.02	59.2	21	8.7 ± 6.43 ± 2.08
3	236.5	10.4 ± 0.08	18.0 ± 5.93 ± 2.13	15.7	21	18.5 ± 6.09 ± 2.19
4	215.4	12.0 ± 0.11	20.0 ± 6.03 ± 2.16	13.2	21	20.5 ± 6.19 ± 2.21
5	222.9	11.7 ± 0.14	31.5 ± 8.90 ± 2.15	21.6	21	32.3 ± 9.14 ± 2.21
6	221.9	14.1 ± 0.14	15.5 ± 4.92 ± 2.11	14.5	21	15.9 ± 5.05 ± 2.16
7	229.2	13.6 ± 0.10	16.5 ± 6.19 ± 2.15	14.5	21	16.9 ± 6.36 ± 2.21
8	233.2	12.5 ± 0.10	23.5 ± 6.14 ± 2.15	9.8	21	24.1 ± 6.30 ± 2.20
9	252.3	12.5 ± 0.10	32.0 ± 3.75 ± 2.10	34.3	21	32.9 ± 3.84 ± 2.16
10	255.6	13.7 ± 0.09	15.0 ± 6.97 ± 2.09	11.9	21	15.4 ± 7.15 ± 2.14
11	264.4	13.5 ± 0.11	19.0 ± 5.76 ± 2.09	9.4	21	19.5 ± 5.92 ± 2.14
12	305.3	14.2 ± 0.18	41.5 ± 11.91 ± 2.11	14.5	21	42.6 ± 12.23 ± 2.16
13	347.7	14.6 ± 0.11	20.5 ± 9.94 ± 3.21	4.9	11	21.0 ± 10.21 ± 3.30
14	1.5	13.9 ± 0.13	23.5 ± 8.36 ± 2.58	12.6	14	24.1 ± 8.58 ± 2.65
15	8.5	13.6 ± 0.11	15.0 ± 11.68 ± 2.48	3.1	12	15.4 ± 11.99 ± 2.55

Note. — The uncertainties in the radii are defined as $R_{max} - R_{1/2}$. Best fit values of the shift and angular expansion rate for each extraction aperture are followed by their 1σ statistical and systematic uncertainties, respectively.

of $2.74 \pm 0.05 \times 10^{-6}$ erg s^{-1} ster^{-1} cm^{-2}, assuming the same spectral shape as that of the northeast (NE) filament measured by Helder et al. (2010), since this region of the forward shock has a shock velocity similar to the global measured value (see value cited in §2.4). The flux measurement is robust against variation of the width of the narrow Hα line over the range 25–50 km s^{-1}. We obtain an ambient neutral hydrogen number density of $0.084 \pm 0.003(\epsilon_{\mathrm{H}_\alpha}/0.2)^{-1}$ cm^{-3} or, equivalently, a mass density of $1.95 \pm 0.07(\epsilon_{\mathrm{H}_\alpha}/0.2)^{-1} \times 10^{-25}$g cm^{-3} (assuming a mean molecular mass of $1.4 m_{\mathrm{AMU}}$). This calculation only accounts for neutral hydrogen, so it therefore sets a lower limit on the total (neutral plus ionized) hydrogen density surrounding 0509−67.5.

2.4 Broad Hα Velocity width versus shock velocity: A Tale of Temperature Equilibration

One major uncertainty in BD shocks is the degree to which the temperature of the shocked protons and electrons equilibrate directly at the shock front. In a simple J-shock where $\gamma = 5/3$, the temperature of the shocked electrons or protons should be $T_{\mathrm{e,p}} = 3/16\, m_{\mathrm{e,p}} v_{\mathrm{s}}^2 / k_{\mathrm{B}}$.

In the simplest case, then, the ratio of initial post-shock electron to ion temperatures, which we define as $\beta \equiv T_{\rm e}/T_{\rm p}$, should be equal to the ratio of the electron to proton mass $m_{\rm e}/m_{\rm p} \approx 0.00054$. In many remnants, though, β is considerably larger that this, hinting at some unknown process that is heating the electrons on a timescale much shorter than that of Coulomb collisions with protons. This anomalous heating is believed to arise from plasma instabilities, such as, for example, ions reflected upstream from the shock in the form of ion acoustic and Langmuir waves (Cargill & Papadopoulos 1988). While measuring the immediate post-shock electron and proton temperatures directly is not an option, measurement of the shock velocity and the width of the broad component of the Hα line can in principle allow us to constrain β. The large uncertainty on the distance to most Galactic remnants limits their value for such studies. Given the accurately known distance to 0509−67.5, our proper motion measurements result in a direct, accurate measure of the shock velocity. As we show below, this allows us to tightly constrain the degree of initial temperature equilibration in the NE portion of 0509−67.5's forward shock.

The width of the broad component of the Hα emission line was measured by Helder et al. (2010) to be 3900 ± 800 km s^{-1} and 2680 ± 70 km s^{-1} for the portions of the NE and SW rims, respectively, that were intersected by their slit. There is a significant velocity offset between the broad-and-narrow components in the SW of 630 ± 28 km s^{-1}; the velocity offset is smaller in the NE (170 ± 220 km s^{-1}) and so can be safely ignored in comparison to the expansion speed we measure. Helder et al. (2010) also measured the broad-to-narrow intensity ratio ($I_{\rm B}/I_{\rm N}$) for the Hα emission line to be 0.08 ± 0.02 and 0.29 ± 0.01 for the NE and SW rims, respectively.

Here we determine the shock velocity from the *HST* imaging at the location of the NE rim imaged by the FORS2 data. The slit was 1.6″ wide, which is the same as the width of region 8, which was centered on the slit location. The delivered image quality (seeing) was in the range 0.7″-0.8″ during the VLT observation. To account for the seeing-broadened PSF of the ground-based FORS2 data when compared to the ACS data, we determine the

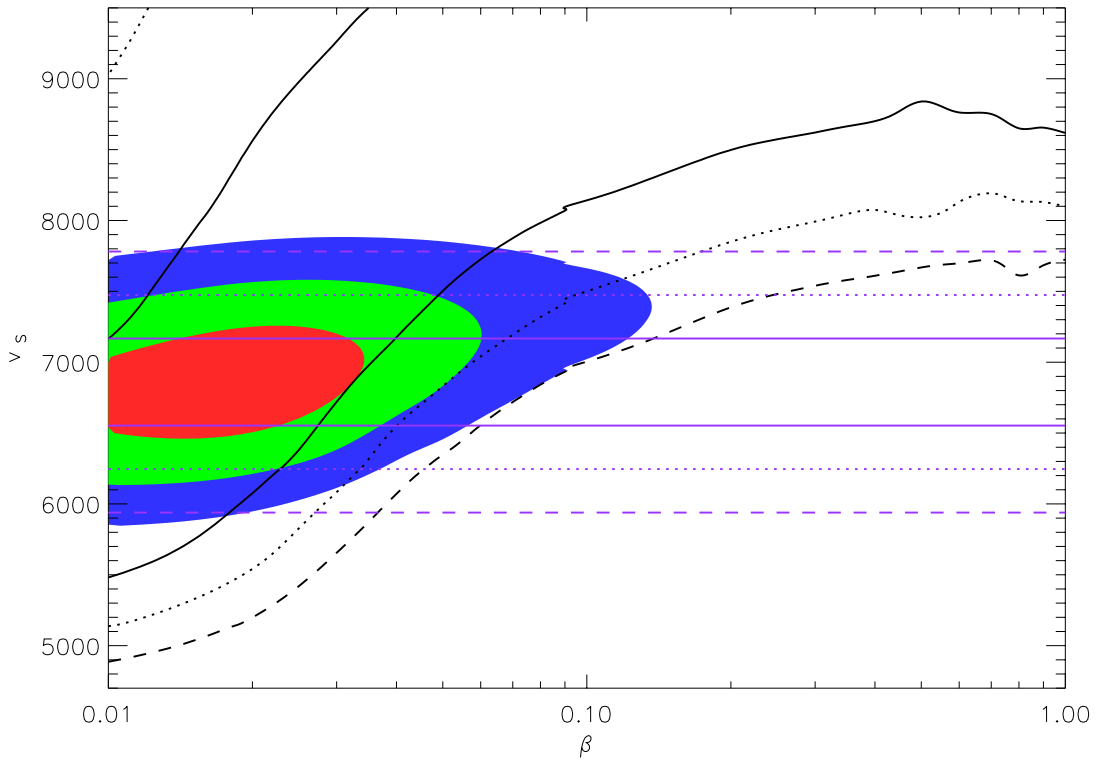

Figure 2.5 Allowed region of parameter space for shock speed and β (electron to ion temperature ratio) for the portion of the NE rim of 0509−67.5 observed spectroscopically by Helder et al. (2010). Black curves show the allowed region derived from the measured width of the broad Hα line and $I_{\rm B}/I_{\rm N}$ values using the Balmer shock models of van Adelsberg et al. (2008), which had a fixed neutral fraction of 0.5. The solid, dotted, and dashed curves correspond to the 1σ, 2σ, and 3σ confidence levels (most of the upper 1σ and 2σ contours and all of the 3σ contour lie above $v_s \sim 9500$ km s^{-1} and are not shown). Horizontal purple lines denote the 1σ, 2σ, and 3σ confidence ranges of our global shock velocity, with the solid, dotted, and dashed lines as before. The filled contours represent the joint combined allowed region that satisfies all measurements; red, green, and, blue filled regions represent the 1σ, 2σ, and 3σ confidence levels.

shock velocity in the NE by finding the weighted mean from regions 7, 8, and 9 which are statistically similar (velocities agree within 1σ) and encompass the smooth northeastern shock (seen in Figure 2.2). This gives an expansion velocity of 6860 ± 307 km s^{-1}, which we equate to the shock velocity. The error on shock velocity is purely statistical; we do not include a systematic error due to uncertainty on the LMC distance.

To interpret these measurements of the shock velocity, $I_{\rm B}/I_{\rm N}$, and the width of the broad Hα line for the NE rim, we use the Balmer shock models of van Adelsberg et al.

(2008). These models incorporate up-to-date atomic physics on charge transfer, collisional excitation, and ionization. They assume no cosmic ray acceleration, an edge-on shock, and an ambient neutral hydrogen fraction of 0.5. The key new feature is a refined treatment of the kinetic properties of the broad neutral component. For a given input value of Hα broad line width and $I_{\rm B}/I_{\rm N}$, these models calculate the corresponding, unique values of shock velocity and β. The black curves in Figure 2.5 show the allowed χ^2 confidence intervals (at 1, 2, and 3σ using solid, dotted, and dashed lines, respectively) on $v_{\rm s}$ and β using the spectral measurements ($I_{\rm B}/I_{\rm N}$ and broad Hα line width) from the NE rim. The purple lines represent the constraints on $v_{\rm s}$ from our expansion measurements, with the solid, dotted, and dashed lines again representing the 1σ, 2σ, and 3σ levels. The filled contours denote the joint confidence intervals in the space of $v_{\rm s}$ and β from the three independent data points.

The first point to make about Fig. 2.5 is that the spectral and imaging results are fully consistent with each other (at 1σ) in the context of the van Adelsberg models. Together the measurements constrain the allowed range of β to be ≤ 0.034 (1σ), ≤ 0.06 (2σ), and ≤ 0.13 (3σ). Note that $\beta = 0.01$ is the minimum value of the model data provided to us by van Adelsberg et al. (2008). Our interpretation differs with the approach of Helder et al. (2010), shown in their Figure 2, that would naively suggest all β values are equally likely. The joint confidence intervals result in preferred values for the broad Hα line width of 4460 km s^{-1} to 4610 km s^{-1} (1σ) and for $I_{\rm B}/I_{\rm N}$ of 0.059 to 0.11. Inclusion of the measured expansion velocity forces us to the upper range of the measured broad line width (although still consistent at 1σ), while the preferred $I_{\rm B}/I_{\rm N}$ range remains centered on the measured value (see Fig. 2.6, which we discuss in detail below).

In the SW the interpretation becomes more difficult since the shock structure is complicated by the presence of multiple filaments, consisting of an outer shock and a brighter, more interior filament. Therefore in the SW our discussion has to consider two separate shocks: an interior one corresponding to our interior regions 6 and 7 (as in our Figure 2.2), and an outer one comprised of our outer regions 28 and 29 (Figure 2.2). We find weighted

mean expansion velocities of 3810 ± 906 km s^{-1} and 8500 ± 1340 km s^{-1} for the inner and outer filaments. This includes a small correction for the interior filament due to the observed velocity offset of 630 km s^{-1} for the broad component relative to the narrow line, that suggests a non-edge-on shock inclination angle. A plausible explanation for the large difference in shock velocities in these two nearby filaments, is that the interior filament has recently encountered a region of higher density and has been decelerated significantly. The concave shape of the interior filament at this location adds some support to this idea.

If we assume, on the one hand, that the FORS2 spectrum of the SW rim included only the interior shock emission, then we find that the broad component width and our shock velocity are consistent, given the van Adelsberg models, for all values of β. However the predicted broad-to-narrow Hα ratio in this situation is too large with a predicted range of $0.77 - 1.4$. On the other hand, the outer shock's expansion speed predicts a range of $3600 - 4700$ km s^{-1} for the width of the broad Hα line which is far too high to be consistent with the measured value. Additionally the faster outer shock predicts small values of $I_{\rm B}/I_{\rm N}$ $(0.03 - 0.13)$, which are also inconsistent with the observations. A plausible explanation, therefore, is that we are seeing a combination of the two shocks in the FORS2 spectrum, where the broad component comes mainly from the interior filament, while there are significant contributions to the narrow component from both the interior and exterior filaments. We get good agreement with the measured broad-to-narrow ratio if we assume that the FORS2 spectral extraction aperture included all the exterior filament's emission and roughly 70% of the interior filament (using the *HST* fluxes). The possibility for contamination of the VLT spectra by both filaments was also suggested by the erratum to Helder et al. (2010) (Helder et al. 2011).

We also employ the Balmer shock models of Morlino et al. (2013a) to compare the measured shock velocities and Hα broad line widths for the SW and NE rim locations. These models include updated atomic physics and allow for multiple charge exchanges (> 3), along with other assumptions that vary from those of van Adelsberg et al. (2008)

with the consequence that the newer models predict smaller broad line widths for all shock velocities greater than 2000 km s^{-1}. The Morlino et al. (2013a) models also allow for the inclusion of the effects of cosmic ray (CR) acceleration, which tends to further decrease the Hα broad line width at fixed shock velocity.

A direct comparison of the measured Hα broad line width is shown in Figure 2.6 (*left*). We use equation 10 from Morlino et al. (2013a), the case without CR acceleration, for a direct comparison with van Adelsberg et al. (2008). For the SW data point we assume the slower shock velocity (3810 ± 906 km s^{-1}) of the inner brighter filament, since it likely contributes the most to the broad line width. In figure 2.6 (*right*) we show the intensity ratio compared to those predicted by the Balmer shock model of van Adelsberg et al. (2008) (this value is not modeled by Morlino et al. (2013a)). The southwestern shock is not shown in this figure since the measured narrow component flux contains significant contributions from both the slowly moving inner filament and the fast outer one.

Rather than providing evidence for efficient CR acceleration, the broad line widths from the Morlino et al. (2013a) models that include no CR acceleration (for either full or no equilibration) appear to be entirely consistent with the observations. However, this comparison is not conclusive since it only examines the broad line width and not the broad-to-narrow flux ratio, which, as shown above, was critical for constraining the degree of electron-ion equilibration for the van Adelsberg et al. (2008) models. Future work with a proper treatment of the measured Hα intensity ratios between broad and narrow components will be needed to constrain the extent of CR acceleration in this remnant.

In summary, we find consistency with a low level of temperature equilibration at the NE shock in 0509−67.5 and, correspondingly, we find no need to invoke the presence of efficient CR acceleration to explain the measurements. Unfortunately the complicated two shock structure in the SW does not allow us to draw any definitive conclusions along similar lines. Our ad hoc attempts to include both filaments in the interpretation of the spectral data, show consistency with a broad range of β values and, again no apparent need for

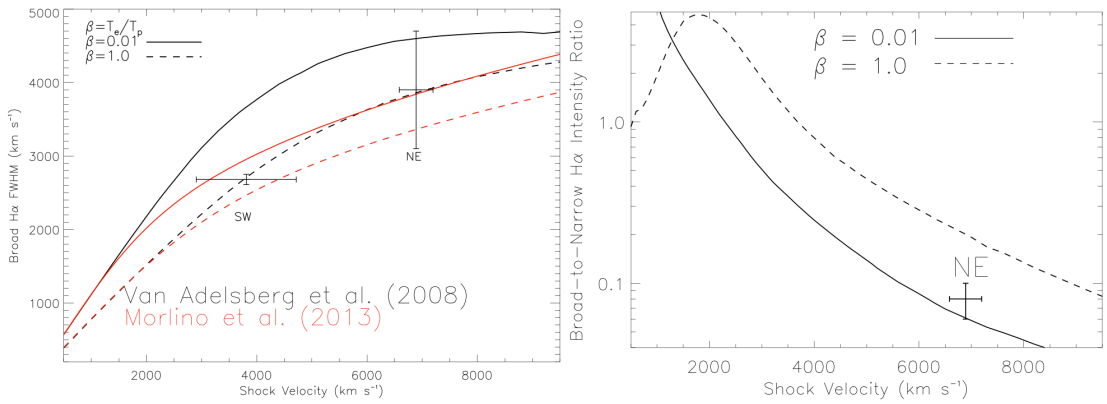

Figure 2.6 *Left* - Hα broad line width vs. shock velocity for the Balmer shock models of van Adelsberg et al. (2008) in black and the models of Morlino et al. (2013a) in red. Solid curves are shown for $\beta = 0.01$ and dashed curves for the case of full temperature equilibration ($\beta = 1.0$). The measured Hα broad line width and shock velocities for the NE and SW are shown with their corresponding 1σ statistical uncertainties. *Right* - Curves of the predicted intensity ratio of the broad and narrow components of the Hα line vs. shock velocity (van Adelsberg et al. 2008). The NE rim data point and uncertainties are plotted. Due to the complex nature of the SW shock, which is likely a blend of separate Hα emission lines from at least two filaments with different expansion speeds (see text for details), we omit showing this datum on the figure.

the inclusion of efficient CR acceleration. Therefore we do not confirm previous claims of evidence *for* efficient CR acceleration in 0509−67.5 based on the properties of the Balmer line spectrum. Available models that account for CR acceleration (Morlino et al. 2013a) predict lower broad line widths and so it does not seem likely to us that applying such models to the current Balmer shock data on 0509−67.5 will result in robust evidence for CR acceleration.

2.5 Hydrodynamic Simulations

2.5.1 Hydro Code

We employ hydrodynamic simulations in order to use our measurements of the velocity and position of the forward shock to set constraints on the properties of the remnant (e.g., age, explosion energy, shock compression factor) and the environment (e.g., ambient density). As a first heuristic example we examine the ejecta-dominated analytical solutions from Truelove

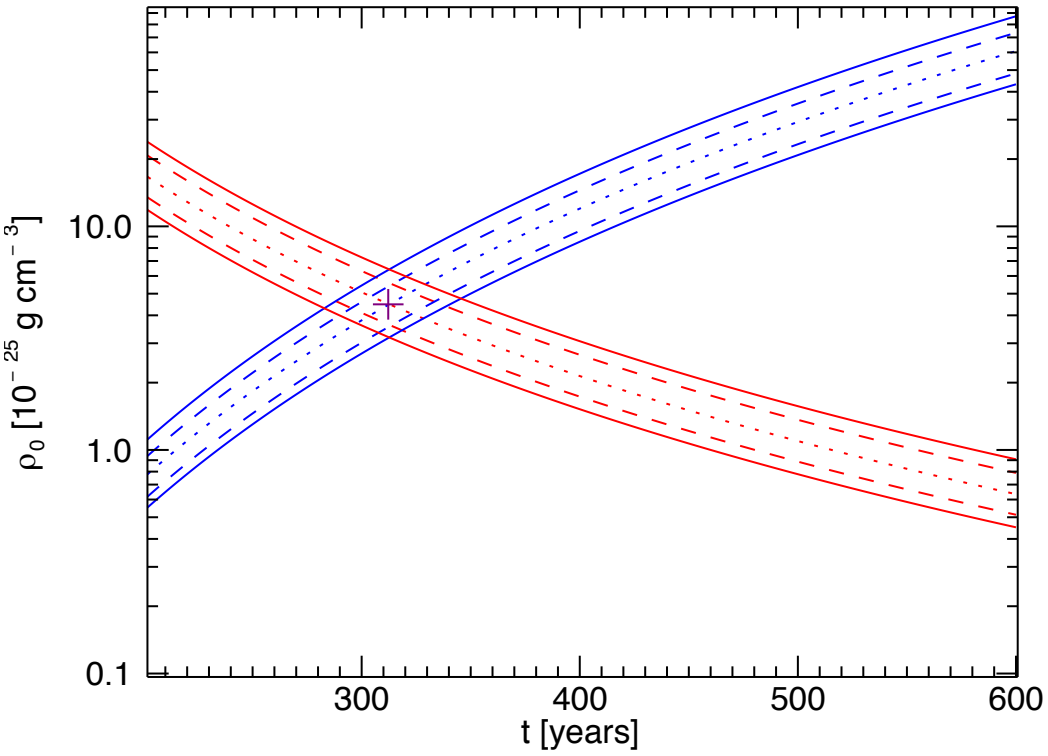

Figure 2.7 Constraints on the density of the ISM and the age of 0509−67.5 from our measurements of radius (in blue) and forward shock velocity (in red) using analytical evolutionary models (Truelove & McKee 1999). For this plot we assume an $n = 7$ power-law ejecta profile with an initial explosion energy of 1.4×10^{51} ergs and total ejecta mass of $1.4\,M_{\odot}$. The dotted lines in each case are the best-fit solutions, while the solid lines show the effect of a $\pm 5\%$ uncertainty on the distance to 0509−67.5. The dashed red lines show the bounds from the 1σ uncertainty on the global shock speed, while the dashed blue curves account for the remnant's ellipticity. The purple cross marks the intersection of the solutions for the best-fit radius and shock velocity.

& McKee (1999) for the r^{-7} ejecta density profile interacting with a uniform-density ambient medium for an explosion energy of 1.4×10^{51} ergs and ejected mass of $1.4\,M_{\odot}$. Figure 2.7 shows constraints on the age and ambient medium density derived from the measured radius (blue curves) and velocity of the forward shock of 0509−67.5 (red curves), with the dotted (dashed) curves showing the best fit (1σ uncertainty range). The solid curves show the affect of a $\pm 5\%$ uncertainty on the distance to the LMC . This approach gives a best fit age of 312 years with an ambient density of 4.5×10^{-25} g cm^{-3} for 0509−67.5, which agree with both the density measurement reported in Williams et al. (2011a) for a mean molecular weight of $1.4 m_{\rm AMU}$ and is within the range of ages determined by Rest et al. (2005a). We also

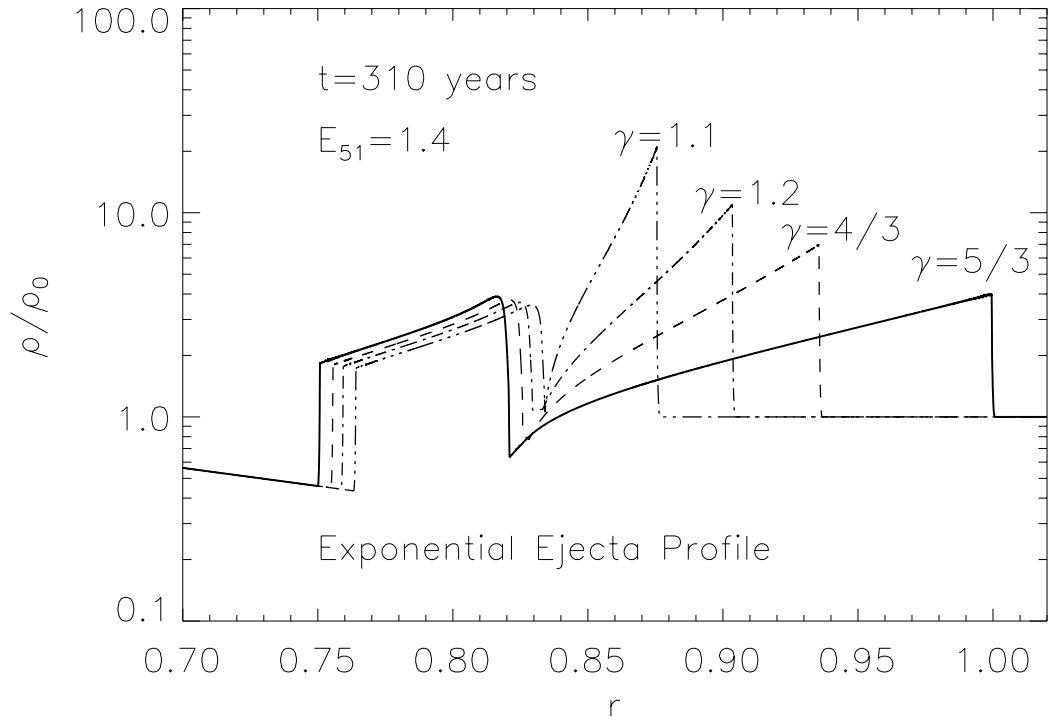

Figure 2.8 Radial density profiles from our hydro simulations for four values of $\gamma_{\rm eff}$ at an age of 310 years and an initial explosion energy of 1.4×10^{51} ergs. The solid, dashed, dotted, and dot-dashed lines represent simulations with $\gamma_{\rm eff}$ of $5/3, 4/3, 1.2$, and 1.1, respectively. We initialize these simulations with an exponential density distribution for the ejecta, which has a total mass of 1.4 $M_{\odot}$. We normalize the densities to the value of the density of the ambient medium (5×10^{-25} g cm^{-1}), and the radii of the simulations to the radius of the forward shock for the $\gamma_{\rm eff} = 5/3$ simulation.

see that the derived age of the remnant is relatively insensitive to the assumed distance to the LMC. While the analytical solutions of Truelove & McKee (1999) serve as a useful first approximation, we employ numerical hydrodynamic simulations to examine other ejecta density profiles and higher compression factors at the forward shock that mimic the effects of efficient CR acceleration on the locations of the fluid discontinuities in 0509−67.5.

For the simulations in this work we use the hydro code Darla, which is our own implementation of a solver for the Euler equations on a 1D, spherically symmetric Lagrangian mesh. The algorithm is based on those described by Richtmyer & Morton (1967) and Bowers & Wilson (1991). The differencing scheme is nearly identical to that used by Truelove & McKee (1999), and includes an artificial viscosity term for dissipation in shocks. Darla

stores the ratio of specific heats for its gamma-law equation of state as a user-specified field variable, allowing this property of the material to vary spatially. We use this feature to vary the compression of the ISM material in the forward shock in our simulation grids, mocking up the effect of cosmic ray acceleration without the need for a more complicated CR model, while at the same time allowing for a reverse shock in the ejecta that is unmodified by cosmic rays. While this obviously does not permit us to make predictions on the properties of whatever CRs may be accelerated in the simulated remnant, it is sufficient for studying the sensitivity of the relative locations of the forward and reverse shocks on the effective equation of state ($\gamma_{\rm eff}$) of the shocked ISM gas. All simulations use 1000 spatial zones equally divided between ejecta and the ambient medium.

We specify three different initial density profiles for the ejecta: two power-law density profiles ($\rho_{\rm ejecta} \propto r^{-n}$) with $n = 7$ and $n = 4$, and a third that uses an exponential profile. We use the $n = 7$ ejecta profile for its historical utility in modeling the evolution of SNR shock waves from SNe Ia (Chevalier 1982). More recently, however, Fryer et al. (2010) found that initial power-law ejecta profiles with $n = 4$ provided the best fit to 1-D averaged radial density profiles from their radiation-hydrodynamic simulations of double degenerate explosions. In either case, the power-law ejecta profiles include a central flat core, which is necessary to keep the mass of the ejecta from diverging (Truelove & McKee 1999). The radius where the profile transitions from the flat core to the power-law falloff is set by a dimensionless parameter, $w_{\rm core}$ (Truelove & McKee 1999), which additionally defines the initial maximum velocity of the ejecta for a given initial explosion energy and ejecta mass. We choose a range of $w_{\rm core}$ values that correspond to maximum ejecta velocities in the range of $12,000 - 45,000$ km s^{-1}.

We also implement exponential ejecta profiles. Dwarkadas & Chevalier (1998) showed that such profiles reliably fit global features of synthetic profiles produced from various explosion model simulations. The initial conditions for these profiles only depend on the input ejecta mass and explosion energy, avoiding the need for any "hidden" parameter (like

$w_{\rm core}$ in the power-law profiles). We treat the exponential profiles as our "nominal" case, with the power-law models showing variation about that.

We vary the compression factor at the forward shock with the input parameter $\gamma_{\rm eff}$ to mimic the effects of efficient CR acceleration, using values of $\gamma_{\rm eff} = [5/3, 4/3, 1.2, 1.1]$ as in Blondin & Ellison (2001). The values of $\gamma_{\rm eff}$ we use determine compression ratios, defined as $\rho_s/\rho_0 = (\gamma+1)\,/\,(\gamma-1)$, of $[4, 7, 11, 21]$, respectively. The first two values correspond to the equation of state for non-relativistic and relativistic monatomic gases, while the later two values are intended to simulate shocks with high compression ratios. Figure 2.8 shows simulated density profiles at an age of 310 years for the exponential density profile and the four $\gamma_{\rm eff}$ values. All four cases used the same initial kinetic energy of 1.4×10^{51} ergs and ambient medium density of 5×10^{-25} g cm^{-3}. For illustrative purposes we have normalized the radial coordinate of all the profiles to the FS radius in the $\gamma_{\rm eff}$= 5/3 case. This clearly shows the different compression factors for the four cases, and also that the locations of the FS were altered much more than that of the reverse shock or the contact discontinuity, when we vary $\gamma_{\rm eff}$. The different locations of the contact discontinuity are a result of the differences in swept-up ISM in the four cases.

We can cast the evolution of velocity and radius with time from the hydro code into a dimensionless form for each initial ejecta density profile and effective equation of state. Figure 2.9 shows these curves for the exponential profile and our four $\gamma_{\rm eff}$ cases. To convert to dimensional units we use the same characteristic values in these scaling relationships as Dwarkadas & Chevalier (1998), namely:

$$\mathrm{R_{ch}} = \left(\frac{\mathrm{M_{ejecta}}}{4/3\pi\rho_0}\right)^{1/3}, \tag{2.3}$$

$$\mathrm{V_{ch}} = \left(\frac{2\,\mathrm{E_{51}}}{\mathrm{M_{ejecta}}}\right)^{1/2}, \tag{2.4}$$

and

$$\mathrm{t_{ch}} = \frac{\mathrm{R_{ch}}}{\mathrm{V_{ch}}} = \mathrm{M_{ejecta}}^{5/6}\,(4/3\pi\rho_0)^{-1/3}\,(2\,\mathrm{E_{51}})^{-1/2}\,. \tag{2.5}$$

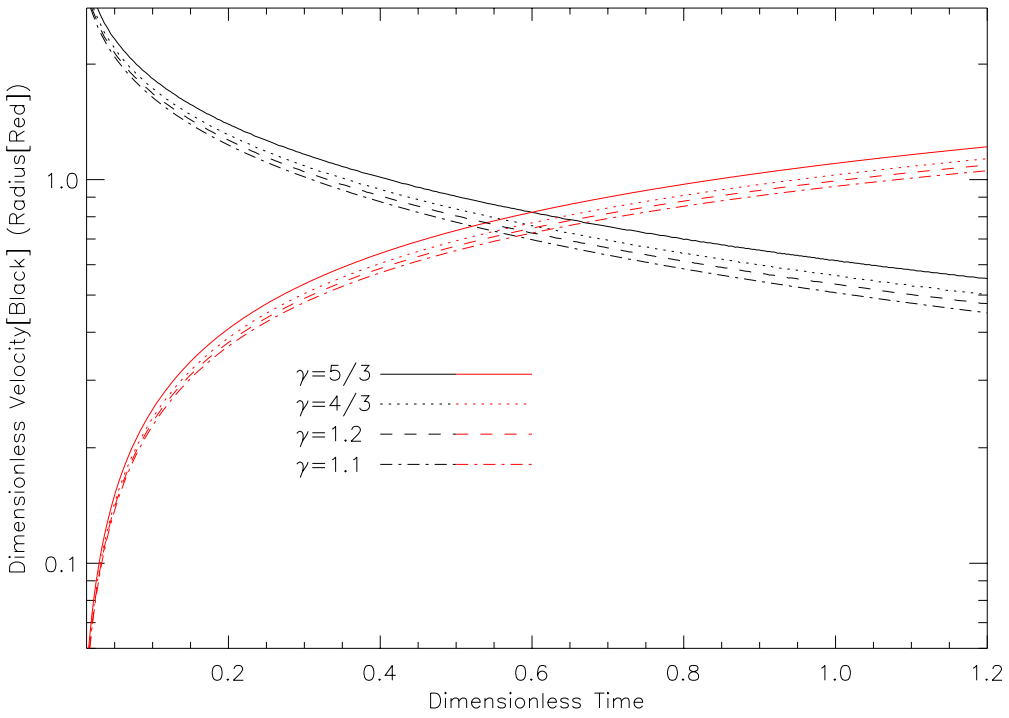

Figure 2.9 Curves of dimensionless forward shock velocity (black) and radius (red) as a function of dimensionless time for the exponential ejecta density profile and four values of $\gamma_{\rm eff}$ (5/3, 4/3, 1.2, and 1.1 shown with solid, dotted, dashed, and dot-dashed curves, respectively).

Varying the ejecta mass in the simulations over a range of $1.0 - 2.0\ M_{\odot}$ did not significantly impact the projected age for the remnant, so we adopt a total ejecta mass of $1.4\ M_{\odot}$ for all simulations.

The choice for our range of initial kinetic energies of the ejecta reflects the findings of Badenes et al. (2008) who preferred an initial explosion energy of 1.4×10^{51} ergs. We explore the effect of lower explosion energies using values of E_{51} =[1.0, 1.2, 1.4], where E_{51} denotes the initial kinetic energy in units of 10^{51} erg.

To summarize: each evolutionary model is defined by a total ejecta mass, an initial kinetic energy, $\gamma_{\rm eff}$, an initial ejecta profile, and for the power-law profiles, $w_{\rm core}$. We explore the resulting allowed parameter space of remnant age and ambient ISM density for each model, constrained by our measurements of the FS velocity (6500 ± 200 km s^{-1}) and average radius ($15'' \pm 0.5''$ or 3.636 ± 0.121 pc for the assumed LMC distance) from an ellipse fit to positions given in Table 2.1. The generous uncertainty on the FS radius comes from the measured ellipticity of 0509−67.5, as determined in §3.1.1.

2.5.2 Results

The Age and Dynamical State of 0509−67.5

For each evolutionary model as just defined, we track the value of the FS velocity and radius as a function of time for a specific value of the ambient medium density. At each time step (i) we compute the figure-of-merit function given by $\chi^2 = [(v_i - v)/\sigma_v]^2 + [(r_i - r)/\sigma_r]^2$ that compares the modeled velocity (v_i) and radius (r_i) to the measurements (v,r) with their uncertainties (σ_v,σ_r). By iterating over different values for the ambient medium density we map out the χ^2 surface in the parameter space of age and ambient medium density. This is repeated for the 3 initial kinetic energy cases, the 4 values of $\gamma_{\rm eff}$, and the 3 different initial ejecta profiles. In the case of the power-law profiles we marginalize χ^2 over all $w_{\rm core}$ values that produce maximum ejecta velocities in the range 12,000 - 45,000 km s^{-1}.

Figure 2.10 shows the 90% confidence intervals for all models, with each panel in the

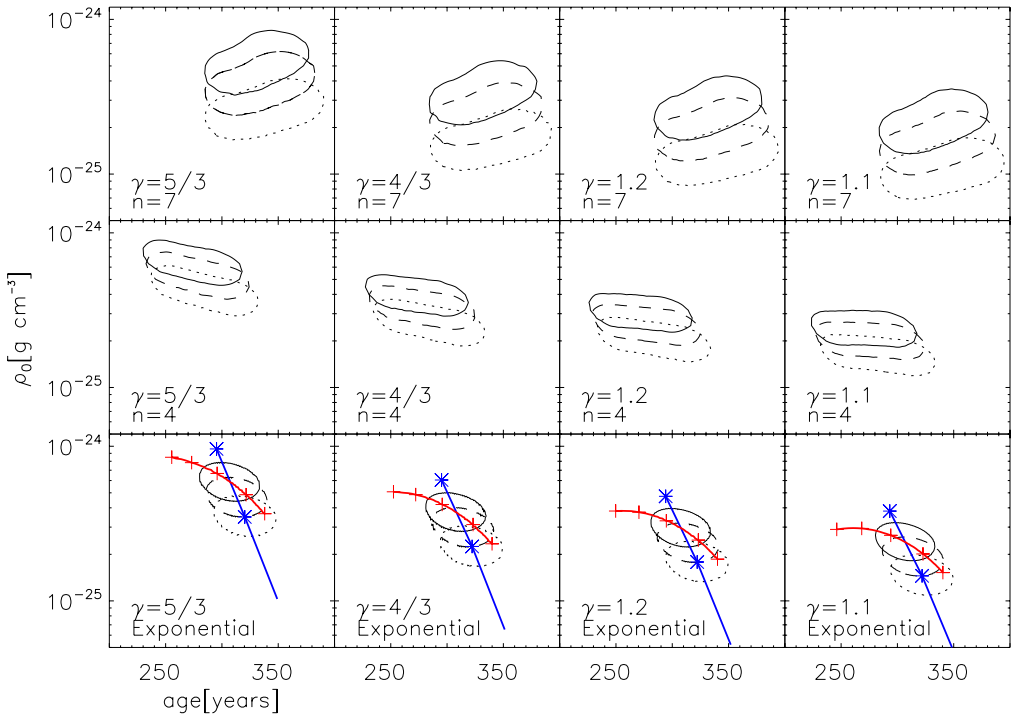

Figure 2.10 Constraints on the ambient medium density and the age of 0509−67.5 from our measurements of radius (3.636 ± 0.121 pc) and forward shock velocity (6500 ± 200 km s^{-1}) using our numerical hydrodynamic simulations. Each panel contains the 90% confidence intervals for three evolutionary models with different explosion energies (E_{51} values of 1.0, 1.2, and 1.4 plotted with dotted, dashed, and solid contours, respectively). Each row of panels shows models with the same initial ejecta density distribution, where the columns share common effective equations of state ($\gamma_{\rm eff}$). For our preferred exponential models (the bottom row of panels) we also show curves along which our uncertainty ellipses would move while varying explosion energy at fixed mass (blue curves) and varying the ejecta mass at fixed explosion energy (red curves). The curves intersect at our nominal case of $\rm E_{51} = 1.4$ and $\rm M_{ejecta} = 1.4$. Ejecta masses of $0.25 M_\odot$, $0.50 M_\odot$, $1.00 M_\odot$, $2.00 M_\odot$, and $3.00 M_\odot$ are denoted with red pluses (from left-to-right) and initial explosion energies, $\rm E_{51}$, of 1.0 and 2.0 are marked with blue asterisks (from bottom-to-top).

figure containing the models with the same $\gamma_{\rm eff}$ and initial density distribution and plotting the three models of varying initial energies of $E_{51} = [1.0, 1.2, 1.4]$ with dotted, dashed, and solid lines respectively.

One interesting result is that the age constraints for each initial density distribution vary only slightly across the different values of $\gamma_{\rm eff}$ and E_{51} we used. The tightest age constraints, 310^{+40}_{-30} yr come from our preferred case of an exponential density distribution with an explosion energy of 1.4×10^{51} erg. Considering the full range of simulations, we find an age range of 230-390 yr.

For our preferred exponential ejecta model with an explosion energy of 1.4×10^{51}ergs, we find that the dimensionless velocity for all four choices of our effective equation of state give a value of $\rm V/V_{ch} = 0.650$. The dimensionless radius of the remnant is $\rm R/R_{ch} = [1.05, 0.90, 0.84, 0.77]$ and the dimensionless time is $\rm T/T_{ch} = [0.93, 0.79, 0.74, 0.68]$, using the best fit ambient medium density for each of the different $\gamma_{\rm eff}$ cases (5/3, 4/3, 1.2, and 1.1).

We also investigated the effect on our fitted ambient density and age of varying the total ejecta mass and explosion energy for our preferred models. The red curves in figure 2.10 (bottom row) show the effect of varying mass at fixed explosion energy, while the blue curve shows the effect of varying explosion energy at fixed mass. Red pluses indicate total ejecta masses of $0.25\rm M_\odot$, $0.50\rm M_\odot$, $1.00\rm M_\odot$, $2.00\rm M_\odot$, and $3.00\rm M_\odot$ for the case of varying ejecta mass in figure 2.10 all of these assume an explosion energy of 1.4×10^{51} ergs. The blue line shows the best fit curve when we vary the explosion energy for a fixed ejecta mass of $1.4\,\rm M_\odot$. We show explosion energies in the range of $0.5 < E_{51} < 2.0$ and blue asterisks mark explosion energies of 1.0 and 2.0 (from bottom-to-top). The red and blue curves intersect at our nominal case where $\rm E_{51}$=1.4 and $\rm M_{ejecta} = 1.4$ for each $\gamma_{\rm eff}$.

With a determination of the remnant's age, we examine the expansion parameter of the remnant, defined as $\eta = v_s\, t/R_s$, where t is the age of the remnant. The expansion parameter η indicates the evolutionary state of the remnant: the free expansion phase

Table 2.3. Neutral Fraction as a Function of Compression Factor

$\gamma_{\rm eff}$	C_γ	$\langle C_\gamma \rangle$	$n_{\rm H}$	$f_{\rm n}$
5/3	4	2.90±0.03	$0.203^{+0.048}_{-0.045}$	$0.41^{+0.098}_{-0.091}$
4/3	7	4.80±0.05	$0.123^{+0.029}_{-0.027}$	$0.68^{+0.102}_{-0.100}$
1.2	11	7.30±0.08	$0.081^{+0.019}_{-0.018}$	$1.04^{+0.250}_{-0.232}$
1.1	21	13.60±0.41	$0.043^{+0.010}_{-0.010}$	$1.95^{+0.478}_{-0.446}$

Note. — C_γ is the compression factor (ratio of post- to pre-shock density) at the forward shock. $\langle C_\gamma \rangle$ is the emission-measure-weighted compression factor, integrated from the contact discontinuity to the forward shock.

has $\eta = 1$, ejecta-dominated phase includes the range $0.4 < \eta < 1$, the adiabatic Sedov phase has $\eta = 0.4$, while later stages of evolution (e.g., radiative) have $\eta < 0.4$. Our preferred exponential model yields an expansion parameter of $\eta = 0.57^{+0.08}_{-0.05}$, while our full complement of evolutionary models constrain the range of the expansion parameters to be $0.42 < \eta < 0.72$, showing that the remnant is firmly in the ejecta dominated phase of its evolution.

Constrains on $\gamma_{\rm eff}$ from the Ambient Medium Density

In their analysis of mid-IR spectra from the *Spitzer Space Telescope*, Williams et al. (2011a) found an average post-shock hydrogen number density of $n_{H_S} = 0.59^{+0.14}_{-0.13}$ for 0509−67.5. This value comes from the entire post-shock flow region of the FS. Therefore, in order to determine the pre-shock density we need to calculate an average compression factor, $\langle C_\gamma \rangle$, weighting the density in the FS region (from the contact discontinuity to the shock-front) by the emission measure, $EM = \int n_e n_p \, dV$, where n_e (n_p) is the post-shock electron (proton) density. With our assumed spherical symmetry we calculate $\langle C_\gamma \rangle = \int [\rho(r)]^3 \, r^2 \, dr / \{\rho_0 \int [\rho(r)]^2 \, r^2 \, dr\}$.

These average compression factors were calculated using the exponential ejecta density

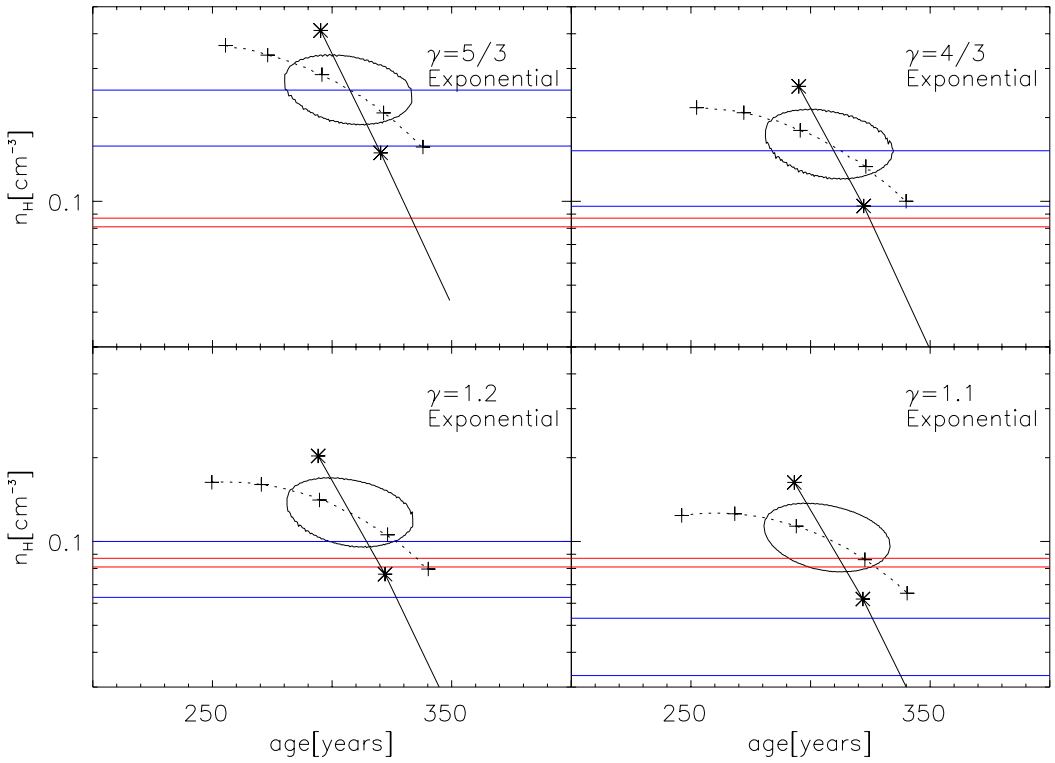

Figure 2.11 Constraints on the ambient hydrogen number density and age for the simulations initialized by exponential ejecta density profiles (the same as the bottom row of panels in Figure 2.10). The red horizontal lines mark the 1σ bounds on the neutral hydrogen density from the Hα surface brightness (see §2.3.3). The blue horizontal lines denote the 1σ bounds for the *total* hydrogen density in the ambient ISM from Williams et al. (2011a). Again we plot the curves along which our uncertainty ellipse would move for cases of fixed ejecta mass and varying the explosion energy (solid curve) and fixed explosion energy and varying the ejecta mass (dashed curve). The curves cross at $E_{51} = 1.4$ and $M_{ejecta} = 1.4$. Total ejecta masses of $0.25M_{\odot}$, $0.50M_{\odot}$, $1.00M_{\odot}$, $2.00M_{\odot}$, and $3.00M_{\odot}$ are marked with pluses (from left-to-right) and initial explosion energies, E_{51}, of 1.0 and 2.0 are identified with asterisks (from bottom-to-top]).

profile. Table 2.3 gives the compression factors at the shock front and the emission-measure-weighted compression factors for all effective γ, and are determined at the minimum χ^2 value for each model described earlier in section 2.5 for an explosion energy $E_{51} = 1.4$. The fourth column in Table 2.3 gives the ambient hydrogen number density, found simply as $n_{\mathrm{H_S}} / \langle \mathrm{C}_{\gamma} \rangle$.

Earlier in section 2.3.3, we determined the neutral hydrogen pre-shock density of, $n_{\mathrm{H}_0} = 0.084 \pm 0.003$, from the H$\alpha$ surface brightness and assuming that $\epsilon_{\mathrm{H}_\alpha} = 0.2$. With this we can now determine the pre-shock neutral fractions, which are shown in the last column of Table 2.3. From the neutral fraction alone we can eliminate the $\gamma_{\mathrm{eff}} = 1.1$ case since it

implies a neutral fraction greater than unity. The $\gamma_{\rm eff} = 1.2$ case is also problematic, since the allowed neutral fraction here ($f_{\rm n} > 0.8$) is larger than the maximum value expected given the local flux of Hα ionizing photons from the SNR and the ambient UV and soft X-ray backgrounds (see, for example, Ghavamian et al. 2007)

Figure 2.11 shows the probability contours for the exponential density profiles from figure 2.10 with the same 90% confidence intervals plotted now in terms of the ambient hydrogen number density (assuming a mean molecular mass of 1.4 $m_{\rm AMU}$). The blue horizontal lines denote the range of ambient medium densities for our various $\gamma_{\rm eff}$ values. Red horizontal lines bound our measured density range for the neutral hydrogen component. As in figure 2.10, we show our best fit curves for cases of varying total ejecta masses at fixed $\rm E_{51} = 1.4$ with the dashed line; correspondingly, a solid line shows variation of initial explosion energy at a fixed mass of 1.4 $\rm M_{\odot}$.

The $\gamma_{\rm eff} = 1.2$ case limits the allowed explosion energies to the range $1.0 < E_{51} < 1.2$, disfavoring the value $E_{51} = 1.4$ argued for by Badenes et al. (2008) and providing another strike against this specific model. On the other hand, we see clearly from figure 2.11 that the $\gamma_{\rm eff} = 5/3$ and $\gamma_{\rm eff} = 4/3$ cases agree with all of our initial explosion energy simulations especially the preferred, highest E_{51} one. Since the neutral hydrogen fraction estimates are also plausible for these cases, we can therefore safely conclude that the adiabatic index for the FS in 0509−67.5 lies in the range $4/3 \leq \gamma_{\rm eff} \leq 5/3$, with a shock compression factor of 4–7.

2.6 Conclusions

We present a two epoch *HST* Hα proper motion study of the LMC SNR 0509−67.5 wherein we measure the shock velocity and radius at a number of locations along the rim. The 44 locations at the outermost edge are consistent with a single global shock speed of 6500 ± 200 km $\rm s^{-1}$ when a distance of 50 kpc is adopted for the LMC. We use this value and the average radius of the remnant (15″ or 3.636 pc) in the context of hydrodynamic simulations to

constrain the remnant's age, ambient medium density, and forward shock compression factor (through the adiabatic index). The Hα surface brightness at the face-on shocks observed through the center of the remnant allows us to determine a pre-shock neutral hydrogen density of $0.084 \pm 0.003(\epsilon_{\mathrm{H}\alpha}/0.2)^{-1}\mathrm{cm}^{-3}$, where $\epsilon_{\mathrm{H}\alpha}$ represents the mean number of Hα photons produced per neutral hydrogen atom that enters the forward shock. 0509−67.5 is an ideal candidate for these measurements because the distance to the LMC is much better constrained than the distance to the Galactic remnants, and the BD origin of the shocks allow for a clear determination of the remnant's forward shock.

Our full complement of evolutionary models indicates that the remnant is between 230 and 390 years old, while our preferred exponential density profile simulations give an age of 310^{+40}_{-30} years for an initial explosion energy of 1.4×10^{51} erg. This age range is consistent with the age of 400±120 years reported by Rest et al. (2008) based on light echoes, which is subject to assumptions about the geometry of the dust sheets that scatter the SN light to our line-of-sight.

Using the global shock velocity and average radius, our full range of the remnant's possible age indicates an expansion parameter that falls in the range of 0.41 to 0.73, which firmly places SNR 0509−67.5 in the ejecta-dominated phase of its evolution.

The age range and density of the ambient ISM we infer from our evolutionary models (with $\gamma_{\mathrm{eff}} = 5/3$) are consistent with the predicted ranges from the hydro simulations of Badenes et al. (2008) that were initiated by realistic SN Ia explosion models. This validates our use of the exponential ejecta profile to model the evolution of the forward shock in 0509−67.5. In further comparison with Badenes et al. (2008) we find there is good overlap between our age and ambient medium density constraints and those that they determine from the centroid of the SiKα line (see Fig. 7 of Badenes et al. 2008). We do, however, find that our measurements prefer a lower ambient medium density than the range preferred by the OKα/SiKα ratio (also Fig. 7 of Badenes et al. 2008).

Kosenko et al. (2014) presented a parametric study of cosmic ray acceleration in supernova remnants and use 0509−67.5 as one of their specific examples. They find an age of 360 ± 50 years and an ambient hydrogen density range of 0.1–0.3 cm^{-3} for an explosion energy of 10^{51} ergs and an $n = 7$ ejecta density profile. These agree well with our results for the same explosion energy and ejecta profile for the cases with $\gamma_{\rm eff}$ of 5/3 and 4/3. This is strong validation of our use of $\gamma_{\rm eff}$ to capture the essential effects of cosmic ray acceleration on the dynamical evolution.

We also use the shock velocities from our proper motion study to assess the degree of temperature equilibration between the shocked ions and electrons at those locations of the forward shock that fell within the VLT/FORS2 spectrograph slit of Helder et al. (2010). Their published values for the measured broad Hα line width and the broad-to-narrow Hα line intensity ratio for a portion of the NE rim provide broad constraints on the shock velocity and essentially no constraint on the degree of temperature equilibration. Adding our new measurement of the shock velocity (at the appropriate aperture along the NE rim), provides an acceptable fit to all three measured values with no apparent need to invoke efficient CR acceleration. We find the degree of equilibration between the electrons and protons, β, to be quite low: less than 0.03 (0.13) at the 1σ (3σ) level. This is consistent with the low electron-ion equilibration values found for high speed shocks in other BD SNRs (see, e.g., Ghavamian et al. 2007). Since the models we use for this study (van Adelsberg et al. 2008) do not include the effects of cosmic ray acceleration, we can only conclude that there is no evidence requiring it.

The portion of the SW rim that fell in the spectroscopic slit is perhaps more interesting since this is where Helder et al. (2010) argued that CR acceleration was efficient. They drew this conclusion by comparing their measured Hα broad line width to an estimated shock velocity and found that the protons were cooler than expected. Now, however, with our proper motion measurements we can show that this interpretation is untenable. The high resolution *HST* imaging shows that the SW slit position contains multiple filaments. The

outermost one has a shock velocity of 8500±1340 km s^{-1}, while the adjacent brighter interior filament has a shock velocity of only 3810 ± 906 km s^{-1} (after accounting for projection). Given the strong dependence of the broad-to-narrow line ratio on shock velocity, it is likely that the broad component in the SW slit location is coming largely from the *slower* interior filament.

We also investigate how our measured shock velocities and corresponding Hα broad line widths compare to the Balmer shock model of Morlino et al. (2013a) under the assumption of *no* CR acceleration. Relative to van Adelsberg et al. (2008), the Morlino et al model under this assumption predicts smaller Hα broad line widths at all shock velocities greater than 2000 km s^{-1}. Still, the Morlino et al model is in excellent agreement with the measurements at the NE rim location; it also matches the measurements at the SW rim location as long as we make the plausible assumption that the broad line width measurement here is determined mainly by the slower moving and brighter interior filament. This agreement between the SW shock velocity and the model with no CR acceleration is consistent with the argument made by Morlino et al. (2013b), that if the shock velocity in the SW rim of 0509−67.5 were below 4500 km s^{-1}, then efficient particle acceleration is likely not occurring there.

For the Balmer shock models of Morlino et al. (2013a) that *do* include efficient CR acceleration, the projected Hα broad line widths take on increasingly smaller values, at a given shock velocity, as the modeled efficiency is increased. The inclusion of efficient CR acceleration is, at this time therefore, unwarranted due to the excellent agreement with their Balmer shock model that excluded CR acceleration altogether. Therefore, without additional evidence, Balmer shock models that include CR acceleration can only be used to set an upper limit on the shock acceleration efficiency. The broad-to-narrow Hα flux ratio (which is not currently available in the Morlino et al. (2013a) model) is one observable that has not yet been used to assess the extent of CR acceleration in 0509−67.5 and should be the focus of future efforts.

Even though our findings call into question the argument for efficient CR acceleration in

the SW filament, a more careful study of the long-slit data in conjunction with our proper motion measurements may yet produce the evidence to support this claim.

Finally we use our estimate of the pre-shock *neutral* hydrogen number density surrounding 0509−67.5 and the average post-shock *total* hydrogen number density from Williams et al. (2011a) to constrain the compression factor in 0509−67.5. We find that the highest compression factors we simulated ($C_\gamma > 11$) produce unphysical values for the neutral fraction in the ambient medium, while compression factors of ($C_\gamma = 4 - 7$) are fully acceptable. This range of values is still consistent with efficient CR acceleration: in their comprehensive study of the Tycho SNR Slane et al. (2014) find an overall compression factor of 4.6 with an acceleration efficiency of 26% and estimate that approximately 20% of the total SNR kinetic energy has been converted into cosmic rays. Although we have not yet found evidence for efficient CR acceleration in 0509−67.5, we have not found evidence that precludes it.

Chapter 3

Reviving the Single Degenerate Scenario for the Ia Supernova Event that Formed Remnant 0509−67.5

Abstract

Thanks to our proper motion measurements in §2.3 we are able to determine a dynamical offset of the explosion site from the geometric center along an approximately east-west dynamical axis where the remnant displays asymmetries in brightness and morphology. We measure shock speeds of 5740 ± 380 km s^{-1} to the west and 6370 ± 160 km s^{-1} to the east along our dynamical axis, and a projected diameter of $26.350 \pm 0.034''$. This measurement is used in a Monte-Carlo simulation of various hydrodynamic models, which find a continuum of dynamical offsets of the explosion site relative to the geometric center based on initial assumptions. In the scenario where the remnant expands into different ambient medium densities on each side for the entire lifetime of the remnant's evolution, we find the offset to be $0.790 \pm 0.350''$ to the west along the dynamical axis. We find an offset of $1.370 \pm 0.603''$ in the same direction as the first scenario with an initial asymmetry of the explosion energy. The third scenario is one in which the western shock has recently plowed into an over-dense region in which the limiting case predicts no dynamical offset of the explosion site from the geometric center. This new determination reveals 21 stars with I-band magnitudes ranging from 25.82 to 20.56 (assuming an E(B-V) of 0.13) within the 3-σ error circle of these possible explosion sites. Contrary to earlier claims, the single degenerate scenario for the orginating Type Ia explosion of remnant 0509−67.5 is far from dead.

3.1 Introduction

One of the biggest unsolved questions about Type Ia supernovae (SNe) is the nature of their progenitor systems. The two most prevalent explanations for these explosions are dubbed the single degenerate (SD) and double degenerate (DD) explosion models. In the single-degenerate paradigm, a C/O WD grows its mass by cannibalizing a non-degenerate companion star, in either the companion star's main sequence or its post-main sequence lifetime. The double degenerate explosion model consists of two white dwarf stars, which are degenerate, merging within a binary system where the stars emit gravitational waves and close their orbital distance, or even by the physical collision of two non-orbiting WDs (Raskin et al. 2010).

The evidence seems to cloud the issue further, since observations of different Ia SNe seem to show signs consistent with both SD and DD explosions. Li et al. (2011) argued that SN 2011fe was likely the result of a DD explosion since pre-SN imaging shows no plausible sub-giant or giant stars at the location of the explosion. Later Bloom et al. (2012) argued that hydrogen burning main sequence stars are also ruled out for SN 2011fe, which lends further credence to the claim that this SN is inconsistent with SD explosion models. Conversely, Dilday et al. (2012) found that the optical spectrum SN PTF 11kx is consistent with a single degenerate companion system with the progenitor's companion being a RS Ophiuchi like symbiotic nova. Recently McCully et al. (2014) argued that the Iax SN 2012Z likely resulted from a single-degenerate explosion via pre-explosion *HST* imaging that reveals a blue-giant/supergiant star at the location of the SN, which implies that this was likely the progenitor's companion star.

Apart from these findings, observations of SNRs further cloud the picture with findings that are again consistent with both SD and DD explosions. In Tycho's SNR, Ruiz-Lapuente et al. (2004) found a possible progenitor candidate labeled "Star G", with an anomalously high velocity greater than 100 km $\sec^{-1}$, though this result has been hotly debated (e.g.

González Hernández et al. (2009)). More recently, Xue & Schaefer (2015) independently determine the explosion site and find that star G is excluded at the 8.2σ confidence level, but state that "star O" from Ruiz-Lapuente et al. (2004) is a more viable candidate that also has a larger relative proper motion.

In the supernova remnant (SNR) 0509−67.5, which has been spectroscopically confirmed as a Ia explosion (Rest et al. 2008), Schaefer & Pagnotta (2012) argue that the SD explosion models must be ruled out for this SN, since they detected no plausible companion stars, down to an absolute V-band magnitude limit of $M_V = +8.8$, within their error circle that is shifted to the proposed explosion site. They neglect, however, to account for asymmetries in the shock velocities of the eastern and western halves, but instead calculate their explosion site from a purely geometric diagnosis; this was originally pointed out by Di Stefano & Kilic (2012).

Even though Schaefer & Pagnotta (2012) claimed to have ruled out the SD model for SNR 0509−67.5, in fact they only rule out progenitor systems where the companion star is left relatively unscathed by the SN explosion. In addition, Di Stefano & Kilic (2012) argue that there could be a significant time delay (10^5–10^9 yr) in the SD scenario between the end of accretion, during which the white dwarf would be spun up (increasing the mass required for thermonuclear ignition), and the SN explosion, when the white dwarf would have spun-down sufficiently to actually explode. During the spin-down time the companion star would be able to evolve significantly, becoming significantly fainter. Another counter argument is the possibility that the companion star may have been an M dwarf star that becomes magnetically locked at its poles with the white dwarf star, so that mass can efficiently accrete through a so-called "magnetic bottle" (Wheeler 2012).

Even the earliest optical and X-ray images of this remnant (Tuohy et al. 1982; Mathewson et al. 1983) showed an obvious NE-SW asymmetry in brightness; more recent data, including *Chandra* X-ray (Warren et al. 2005), ultraviolet (Ghavamian et al. 2007), infrared (Williams et al. 2011a), and our narrow-band Hα *Hubble Space Telescope* (*HST*) image of

SNR 0509−67.5 show this brightness asymmetry in even greater detail. A higher density ambient medium in the SW provides a plausible explanation for the morphological asymmetry. Given the importance of this scientific topic and the likelihood that a SD companion could be considerably fainter that previously assumed, in this work we redetermine the explosion site of the SN 0509−67.5 explicitly including our dynamical information in order to address any asymmetry in the evolution of the remnant between the eastern and western halves. We also give an absolute position with respect to a standard reference frame.

The structure of this chapter is as follows. Section 3.2 describes our *HST* observations and relevant data reduction. Proper motion measurements of the forward shock of 0509−67.5 are given in section 3.3. Section 3.4 discusses our candidates for progenitor companions. Conclusions are in §3.5. We assume a distance to the LMC of 50 kpc with an uncertainty of 4% (Clementini et al. 2003). Uncertainties are quoted at the 1-σ (68.3% confidence level) unless stated otherwise.

3.2 Data Analysis

For this work we used a narrow-band F658N and five wide-band images (F475W, F555W, F814W, F110W, and F160W) of 0509−67.5 observed with the *HST*. The F658N narrow-band Hα image was taken with the Advance Camera for Surveys (ACS) wide-field camera on 2006 October 28 for a total exposure time of 4,620 seconds (PI: John P. Hughes Program number 11015). Our five wide-band frames were imaged with the Wide-Field Camera 3 (WFC3) using the F475W, F555W, and F814W optical filters and the F110W and F160W infrared (IR) filters. The F475W and F555W images were taken on 2010 November 4 and have exposure times of 1010 and 696 seconds, respectively, as part of a Hubble Heritage observation (PI: Keith S. Noll; Program number 12326). We use F814W, F110W, and F160W images taken on 2014 September 24 with respective exposure times of 1465, 297, and 798 seconds with the WFC3 on *HST* (PI: You-Hua Chu; program number 13282).

The raw F475W, F555W, and F814W images are corrected for charge-transfer efficiency

(CTE) losses using the `ctereverse` Fortran routine, which is part of the CTE tools package provided by *the Space Telescope Science Institute*. The F658N, F475W, F555W, and F814W images have been processed using the `multidrizzle` routine on a scale of $0.04''$ pixel^{-1}, while the F110W and F160W IR images are drizzled to a scale of $0.10''$ pixel^{-1}. All images have been registered to the LMC microlensing catalog (Rest et al. 2005b), which has an astrometric uncertainty of $0.03''$.

3.3 Dynamical Centroid

3.3.1 Constraining Possible Asymmetries from Proper Motion Measurements

In section 2.3, we determined the geometric center of 0509−67.5, by taking advantage of the striking elliptical symmetry in the outermost Hα emission of the forward shock. The geometric center of the best fitting ellipse is at 05:09:31.086 ,−67:31:16.90 with an uncertainty of $\pm 0.15''$ that comes from the root-mean-square radial residuals.

Our geometric center is in good agreement with that reported in Schaefer & Pagnotta (2012). To further assess the accuracy of our geometric center we fit a second ellipse around the outermost edge of the faint Hα shell of 0509−67.5 and find that this center is displaced by $0.140''$ at an angle of 5.7° west of north with respect to our center determined in §2.3. To account for this difference, we take half of this offset and factor it into our uncertainty of our geometric center and shift our center by half of the offset to the center that we will use for this measurement, at 05:09:31.145 ,−67:31:16.91. Our statistical uncertainty of the ellipse we fit in section 2.3 is $0.150''$, which we root-sum-square (RSS) with the aforementioned $0.070''$ from the displacement of the geometric center. We also run a Monte-Carlo simulation where we perturb the locations of the shock front in the 44 outer regions of §2.3 with their positional uncertainties (see table 2.1) and find the 1σ uncertainty of our geometric center is $0.121''$, which we also RSS into our uncertainty of our geometric uncertainty and find a combined 1σ uncertainty of $0.210''$ for the geometric center of SNR 0509−67.5.

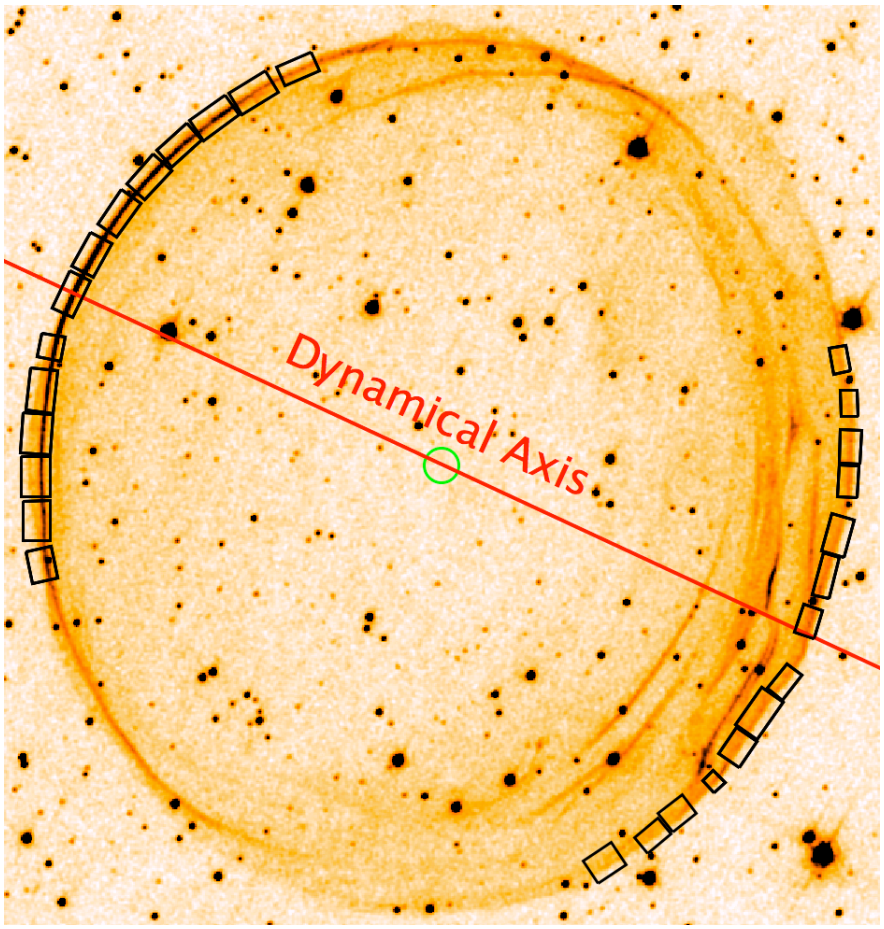

Figure 3.1 ACS F658N image of 0509−67.5 showing the dynamical axis and extraction apertures used to measure the extent of the asymmetrical expansion of the eastern and western halves of the remnant. We also show the 3σ uncertainty circle ($0.63''$) about our new geometric center at 05:09:31.145 ,−67:31:16.91.

A purely geometric determination fails to account for any possible offset in the explosion site due to asymmetric expansion, which, in fact, is indicated by several lines of evidence. In the southwest quadrant of 0509−67.5 there are brightness enhancements in the X-ray (Warren et al. 2005) and infrared (Williams et al. 2011a) bands that suggest a higher density there; our current *HST* Hα image shows a complex set of nested filaments in the SW that contrasts markedly with the single filament that dominates the entire eastern limb.

We are now in a position to use our proper motion measurements to look for asymmetric expansion velocities on the east and west sides of 0509−67.5, which would indicate an offset between the geometric center and explosion site of 0509−67.5.

First, we choose a symmetry axis that passes through the geometric centroid of 0509−67.5, includes an equal number of expansion regions on each side at roughly the same spacings from the symmetry axis, and lies along the NE-SW axis suspected of harboring a dynamical asymmetry. A symmetry axis at a position angle of 65° satisfied these constraints. This is offset slightly from the north-south symmetry axis (at 81.4°) from the elliptical fit. The expansion rate to the western side along the dynamical axis (W_D) was obtained using regions 24-38 (see figure 2.2 in section 2.3 and table 2.1); for the eastern side of our dynamical axis (E_D), we used regions 2-16. We determine the average radius to the W_D and E_D from the geometric center by projecting the shock location in each region to the symmetry axis and averaging the values. Following this procedure, we obtain mean radii of $13.120 \pm 0.023''$ in the W_D and $13.230 \pm 0.025''$ in the E_D. The expansion measurement is made in a similar manner by projecting the expansion velocities along the dynamical symmetry axis; we find the expansion speeds to be 5740 ± 380 km s^{-1} (W_D) and 6370 ± 160 km s^{-1} (E_D).

From the measured projected radii and velocities of the W_D and E_D sides, we can now determine the offset of the dynamical centroid from the geometric centroid along the symmetry axis. This, however, requires an additional assumption about the dynamical evolution of the remnant. The simplest assumption assumes that each side expands at a constant speed. In this case we find that the dynamical center of the remnant is offset from the geometric center by an amount $0.63''$ to the W_D. This is the most naive assumption that we can impose on the evolution and sets a maximum possible age of the remnant to be ~ 530 years, which lies well outside of the ranges found in §2.5, though it is consistent with the age determination from light echo measurements in Rest et al. (2005a).

To more accurately determine the site of the SN that gave rise to SNR 0509−67.5, we implement hydrodynamic modeling to understand the difference between our E_D and W_D projected shock speeds.

3.3.2 Hydrodynamic Simulations

We employ hydrodynamic simulations to examine the possible range of positional offsets for the explosion site of the SN that created 0509−67.5 to its geometric center that we observe now. Using the techniques developed in §2.5, we use the results for our hydrodynamic simulations that are initialized with an exponential density profile of the ejecta to evolve the forward shock in time and determine its radius and speed. An effective equation of state in the forward shock is assumed to be adiabatic ($\gamma_{\rm eff}$=5/3) in lieu of the non-detection of signatures of efficient CR acceleration in 0509−67.5 as argued in §2.4.

Using our dimensionless results of the forward shock radius and speed, we are able to cast these into dimensionally meaningful terms using scaling relationships of the radius ($R_{\rm ch}$), velocity ($V_{\rm ch}$), and time ($t_{\rm ch}$) with those given in Dwarkadas & Chevalier (1998), which are:

$$R_{\rm ch} = \left(\frac{M_{\rm ejecta}}{4/3\pi\rho_0}\right)^{1/3}, \tag{3.1}$$

$$V_{\rm ch} = \left(\frac{2\,E_{51}}{M_{\rm ejecta}}\right)^{1/2}, \tag{3.2}$$

and

$$t_{\rm ch} = \frac{R_{\rm ch}}{V_{\rm ch}} = {M_{\rm ejecta}}^{5/6}\,(4/3\pi\rho_0)^{-1/3}\,(2\,E_{51})^{-1/2}\,. \tag{3.3}$$

These of course are entirely dependent upon the physical quantities of the ejecta mass ($M_{\rm ejecta}$), initial explosion energy (E_{51}, which is the ratio of the explosion energy to 1×10^{51} ergs), and ambient medium density (ρ_0), which dictate the evolution of the forward shock into its ambient medium.

We examine the results of simultaneous simulations of the $E_{\rm D}$ and $W_{\rm D}$ requiring their ages to be equal, thus allowing us to explore a large volume in parameter space by allowing the ambient medium density, explosion energy, or ejecta mass to vary freely for the $E_{\rm D}$ and $W_{\rm D}$. Our measured values for the shock speeds of 6370 ± 160 km s^{-1} and 5740 ± 380 km s^{-1} for the $E_{\rm D}$ and $W_{\rm D}$ respectively, and a diameter of $26.350 \pm 0.034''$, serve to constrain

the hydrodynamic results by way of a χ^2 fitting criteria we use that is shown below;

$$\chi^2 = \sum \frac{(V_{\rm west} - V_{1_i})^2}{\sigma^2_{V_{\rm west}}} + \frac{(V_{\rm east} - V_{2_i})^2}{\sigma^2_{V_{\rm east}}} + \frac{(D_{\rm meas.} - (R_{1_i} + R_{2_i}))^2}{\sigma^2_D}, \tag{3.4}$$

where V_1 (V_2) and R_1 (R_2) are the simulated shock speed and radius for the $\rm W_D$($\rm E_D$) simulation at a given time. This χ^2 value is used as the figure-of-merit function to minimize in our implementation of the IDL downhill simplex fitting routine `AMOEBA` to fit the parameter that is being varied in the $\rm E_D$ and $\rm W_D$ along with the simulated age. It is important to stress that the statistic is *only* used as a fitting figure-of-merit, on which the routine `AMOEBA` minimizes. We do not use it to determine the uncertainties for the explosion site of 0509−67.5.

We use a Monte-Carlo approach to determine the uncertainties in our dynamical offset determination. In these simulations we perturb our measured values of the shock speeds in the $\rm E_D$ and $\rm W_D$ and diameter with their measured uncertainties and fit for all of our parameters of interest. Each set of perturbed input data comprises the i^{th} case for equation 3.4, which is the function that is minimized in the fitting routine. This routine examined 10^5 iterations for each evolutionary model explored. If a given iteration has best fit values of the shock speeds and diameter that differ by more than 2.5% from the given input values, then these data are rejected. This uncertainty of 2.5% is the approximate uncertainty intrinsic to my method of finding shock speeds and radii by means of weighting hydrodynamic zones by their artificial viscosity around the region where the density of the forward shock separates from the ambient medium density.

For each simulation, we are fitting for the $\rm E_{51}$, $\rm M_{\it ejecta}$, or ambient medium density simultaneously in the $\rm W_D$ and $\rm E_D$ along with the dynamical offset from the geometric center and age of the shock. For the majority of the iterations, the χ^2 value is zero since the shock speeds and diameter can be fit perfectly. The uncertainty of the dynamical offset in each case is taken to be the standard deviation of the range of values that are produced in

Table 3.1. Hydrodynamic results for the dynamical offset between the geometric center and possible explosion site(s) of SNR 0509−67.5

Varying Parameter	E_{51}, $M_{ej}/M_\odot$	ρ_{west}/ρ_{east}	$\log_{10}(\rho_{west}{}^{(1)})$	$\log_{10}(\rho_{east}{}^{(1)})$	Shift	t_{min}[years]
$\rho_{\rm west,\ east}$	1.0, 1.4	2.42	-24.32	-24.70	$0.790 \pm 0.350''$	294
	1.2, 1.4	2.31	-24.19	-24.57	$0.790 \pm 0.350''$	288
	1.4, 1.4	2.31	-24.10	-24.46	$0.790 \pm 0.350''$	281
Varying Parameter	$M_{ej}/M_\odot$, $\rho_0^{(1)}$	E_{west}/E_{east}	$E_{west}{}^{(2)}$	$E_{east}{}^{(2)}$	Shift	t_{min}[years]
$E_{\rm west,\ east}$	1.4, 3.6	0.49	0.76	1.54	$1.350 \pm 0.600''$	290
	1.4, 4.7	0.49	0.91	1.87	$1.370 \pm 0.603''$	283
	1.4, 6.0	0.48	1.06	2.20	$1.380 \pm 0.606''$	278

Note. — The west and east subscripts refer to east or west along our dynamical axis. (1) - *Density in units of* 10^{-25} *g* cm^{-3}. (2) - *Energy in units of* 10^{51} *ergs.*

the Monte-Carlo simulation, and the median value is taken to be the value of the dynamical offset from the geometric center, as reported in table 3.1.

Lifetime E-W Variations in Ambient Medium Density

One possible explanation for the asymmetry in shock speeds for the W_D and E_D is that they are evolving into ambient media with different densities. The case we examine here is the one in which both halves evolve into varying E_D-W_D ambient densities for the entire lifetime of the remnant's evolution. We choose to hold the total ejecta mass fixed at $1.4\,M_\odot$ and allow the E_D and W_D ambient densities to vary freely. Three different explosion energies of E_{51} =[1.0,1.2,1.4] are used to perform three independent calculations of the offset from the explosion site and the geometric center along our dynamical axis.

The best fit value for the offset is $0.790''$, and we find the 1σ uncertainty to be $0.350''$ for all three input explosion energies. These values are shown in table 3.1, along with the best fit E_D and W_D ambient medium densities and best-fit age. Reassuringly, the inferred ages are in good agreement with the age determination in §2.5.

E_D-W_D Variations in Explosion Energy

In these simulations, we explore the possible explosion site offset that could result from an asymmetry in explosion energy in the W_D and E_D halves. Again we assume a total ejecta mass of $1.4\,M_\odot$. Three separate simulations are implemented with global fixed ambient medium densities of ρ_0 =[3.6×10^{-25} g cm^{-3},4.7×10^{-25} g cm^{-3},6.0×10^{-25} g cm^{-3}], which correspond to the best fit densities in §2.5, which correspond to explosion energies of E_{51} =[1.0, 1.2, 1.4] for the global fits to 0509−67.5.

We find a best-fit offset of $1.370 \pm 0.603''$ to the W_D for an ambient medium density of 6×10^{-25} g cm^{-3}. These values differ slightly for the other two ambient medium densities explored, but only at most by an amount of $0.03''$. These values are given in table 3.1.

E_D-W_D Variations in Ejecta Mass

We also examined simulations where we fixed explosion energy and ambient medium density but let the ejecta mass in the two halves vary freely. Our primary finding is that an asymmetry in the ejecta mass alone cannot account for the differences in shock speeds we detect now. The fitted masses for these simulations yielded ejecta masses that are inconsistent with realistic progenitor masses for a Ia SN. Therefore, we will not consider this scenario further.

Recent Density Asymmetry

Besides considering the situation where our E and W halves have evolved into two different ambient medium densities throughout the entire evolution of 0509−67.5, we can imagine what results may follow if instead the two halves evolved into rather identical ambient medium densities until a recent interaction with a density enhancement in the west. In the most extreme case, the western shock could have collided with this over-density very recently, which is physically possible given a large enough density contrast in the west. This extreme case would indicate that the explosion site *has not* been offset from the geometric

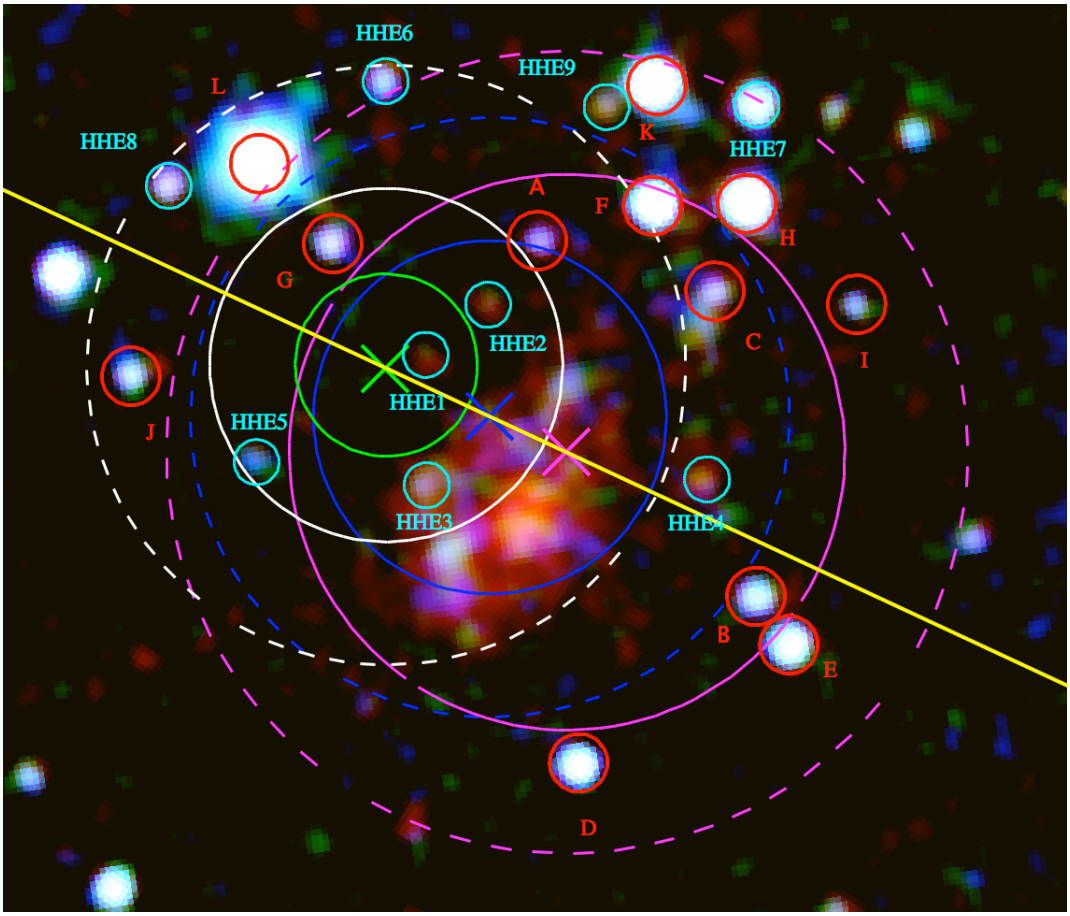

Figure 3.2 Three-color image of 0509−67.5 showing the constraints for the explosion site of the supernova, along with our selection of potential progenitor companions. The red, green, and blue colors correspond to our F475W, F555W, and F814W respectively. The scaling chosen is hyperbolic arc-sin to highlight the faint stars. The green, blue, and magenta crosses mark our geometric center, the dynamical offset in the lifetime density asymmetry case, and the case where there is an asymmetry in the initial explosion energy respectively. The green circle represents the 3σ uncertainty of the geometric center. The inner solid white, blue, and magenta circles represent the 3σ uncertainties in the case of a recent density enhancement, lifetime density asymmetry, and explosion asymmetry, respectively. The larger dashed white, blue, and magenta circles show the maximum displacements for a kick velocity of the progenitor companion when a maximum age of 400 years is adopted.

center that we observe here.

We therefore consider a third possible explosion site at the geometric center proper. In lieu of running more complicated hydrodynamic simulations to determine the proper uncertainty circle, we adopt the 1σ uncertainty to be a conservative $0.350''$, which we derive in the case of the lifetime density asymmetry.

3.3.3 Determination of the Explosion Site and Companion Search Radius

With the results found in table 3.1, we can now define our region of interest to examine potential progenitor companions. Figure 3.2 is a three-color composite image of 0509−67.5 showing the constraints for the explosion site of the SN, along with our selection of potential progenitor companions. The red, green, and blue colors correspond to our F475W, F555W, and F814W images, respectively. At the center of the remnant there is a diffuse source unassociated with the remnant, which is a galaxy at a redshift of $z = 0.031$ (Pagnotta et al. 2014). The green cross marks our geometric center with the green circle representing the 3σ uncertainty of $0.63''$. The inner white circle marks our 3σ uncertainty of $1.22''$ for the dynamical offset in the case of a recent density enhancement in the west. The blue cross marks the dynamical offset from the geometric center for the case of a lifetime asymmetry in the ambient medium density, and the inner blue circle marks the 3σ uncertainty of $1.22''$. The magenta cross indicates the dynamical offset in the case of an initial explosion asymmetry along with the inner magenta circle representing the 3σ uncertainty of $1.92''$.

To accurately constrain our search radius for progenitor companions, we must also account for any possible kick velocity of the companion star at the time of the explosion. As we will see in the following section, all of our progenitor companion candidates are main sequence stars, so we can assume a maximum kick velocity of 510 km sec^{-1}, which translates to an angular velocity of $0.0021''$ year^{-1} (Canal et al. 2001). We depict this constraint in figure 3.2 with the larger dashed white, blue, and magenta circles for a maximum age of 400 years, which we adopt from our findings for the $n = 7$ power law ejecta profile evolutionary

model in section 2.5 (see figure 2.10). These circles have radii of 2.06″, 2.06″, and 2.76″, respectively.

It is clear to see that there are stars within our search area, with all of stars A-L from Schaefer & Pagnotta (2012) (indicated with red circles and corresponding labels in figure 3.2), along with nine additional stars that we label HHE 1 - HHE 9, which are marked with cyan circles and labels. Though HHE 1-3 appear within the 3σ uncertainty circle of Schaefer & Pagnotta (2012), these stars were only identified with the aid of the deeper F814W image and IR wide-band images (F110W and F160W) we use here, which were not available in the aforementioned study.

3.4 Nature of the possible companion stars

3.4.1 Photometry of Possible Progenitor Companion Candidates

To determine the photometry of our various companion candidate stars, we use standard IRAF aperture photometry software package `APPHOT`. We use extraction apertures of 0.2″ and 0.3″ for our three optical and two IR images, respectively, where the aperture sizes are chosen to be slightly larger than the FWHM of the PSF in the frames. The apertures are corrected for photometric losses due to the selected aperture size in that particular filter, and these losses amount to the following: m_V = (.169, .165, .173, .238, .300) mags for our F475W, F555W, F814W, F110W, and F160W images, respectively, when we use the photometric zeropoints determined with a 0.4″ radius aperture.

The photometric results are given in table 3.2 and have not been corrected for possible dust extinction. Despite the imaging power of the WFC aboard *HST*, obtaining accurate photometry of field stars is far from a trivial process. The systematic uncertainty for the photometry is dependant upon the dither pattern used in the observation plan and the drizzling process used for image combination, as well as uncertainties due to the colors of the stars observed. Beyond this, the exact process used to subtract the background produces

Table 3.2. Photometry of Progenitor Companion Candidates

Star	F475W	F555W	F814W	F110W	F160W
A	27.051±0.186	26.720±0.193	24.850±0.100	24.280±0.149	23.390±0.097
B	25.570±0.055	25.460±0.073	24.000±0.047	23.290±0.049	22.690±0.049
C	27.250±0.288	26.770±0.266	24.780±0.086	23.730±0.091	23.040±0.096
D	24.750±0.034	24.530±0.039	23.580±0.033	23.010±0.044	22.560±0.044
E	24.790±0.033	24.620±0.038	23.590±0.034	23.020±0.037	22.520±0.038
F	24.160±0.023	23.840±0.023	23.050±0.022	22.600±0.033	22.030±0.034
G	26.320±0.109	26.170±0.143	24.330±0.066	23.840±0.085	22.910±0.056
H	23.570±0.017	23.380±0.018	22.620±0.017	22.160±0.024	21.670±0.028
I	27.260±0.256	26.490±0.166	25.290±0.131	24.500±0.143	23.490±0.097
J	26.400±0.126	26.150±0.140	24.760±0.079	23.830±0.071	23.320±0.073
K	23.420±0.014	23.190±0.016	22.420±0.015	22.000±0.019	21.650±0.022
L	21.210±0.005	21.090±0.005	20.760±0.006	20.640±0.010	20.340±0.014
HHE 1	≥28.100[1]	≥27.550[1]	25.690±0.198	24.970±0.262	24.430±0.234
HHE 2	≥28.030[1]	27.440±0.359	25.740±0.210	24.820±0.244	24.090±0.165
HHE 3	≥27.860[1]	26.880±0.233	24.890±0.153	21.340±0.015	20.260±0.014
HHE 4	≥27.770[1]	≥27.440[1]	25.230±0.127	23.970±0.116	23.340±0.116
HHE 5	27.500±0.293	26.470±0.155	26.020±0.258	24.570±0.143	23.550±0.087
HHE 6	26.560±0.143	26.550±0.182	24.640±0.073	23.940±0.087	23.260±0.067
HHE 7	24.910±0.039	24.770±0.046	23.640±0.035	23.110±0.044	22.490±0.039
HHE 8	26.560±0.153	26.190±0.150	24.810±0.096	23.630±0.072	23.140±0.070
HHE 9	≥27.910[1]	26.600±0.190	25.250±0.137	22.000±0.019	21.650±0.022

Note. — All magnitudes reported with reference to Vega in each filter. These have *not* been corrected for extinction.
(1) Detection less than 3σ above background noise.

non-negligible uncertainties on the order of $m_V \sim 0.02$ mags. We therefore take this value to be our systemic uncertainty in our photometry in lieu of more rigorous approaches like those in Sabbi et al. (2009).

3.4.2 Hertzsprung-Russell Diagram of Progenitor Companion Candidates

To place constraints on the masses of the progenitor companions, we plot F555W magnitudes vs. F555w-F814w colours in figure 3.3. The magnitudes have been adjusted to account for Galactic reddining using the extinction values from Schlafly & Finkbeiner (2011) for $R_V = 3.1$ and an E(B-V) value of 0.13, which is determined using the results of Warren & Hughes (2004). Also shown are the Isochrones from the Dartmouth Stellar Evolution Program (DESP) (Chaboyer et al. 2001; Bjork & Chaboyer 2006; Dotter et al. 2008) at ages of 1, 6, and 15 Gyr set at a distance modulus of 18.5, which corresponds to our assumed LMC distance of 50 kpc. These isochrones are for abundances of $[Fe/H] = -0.3$

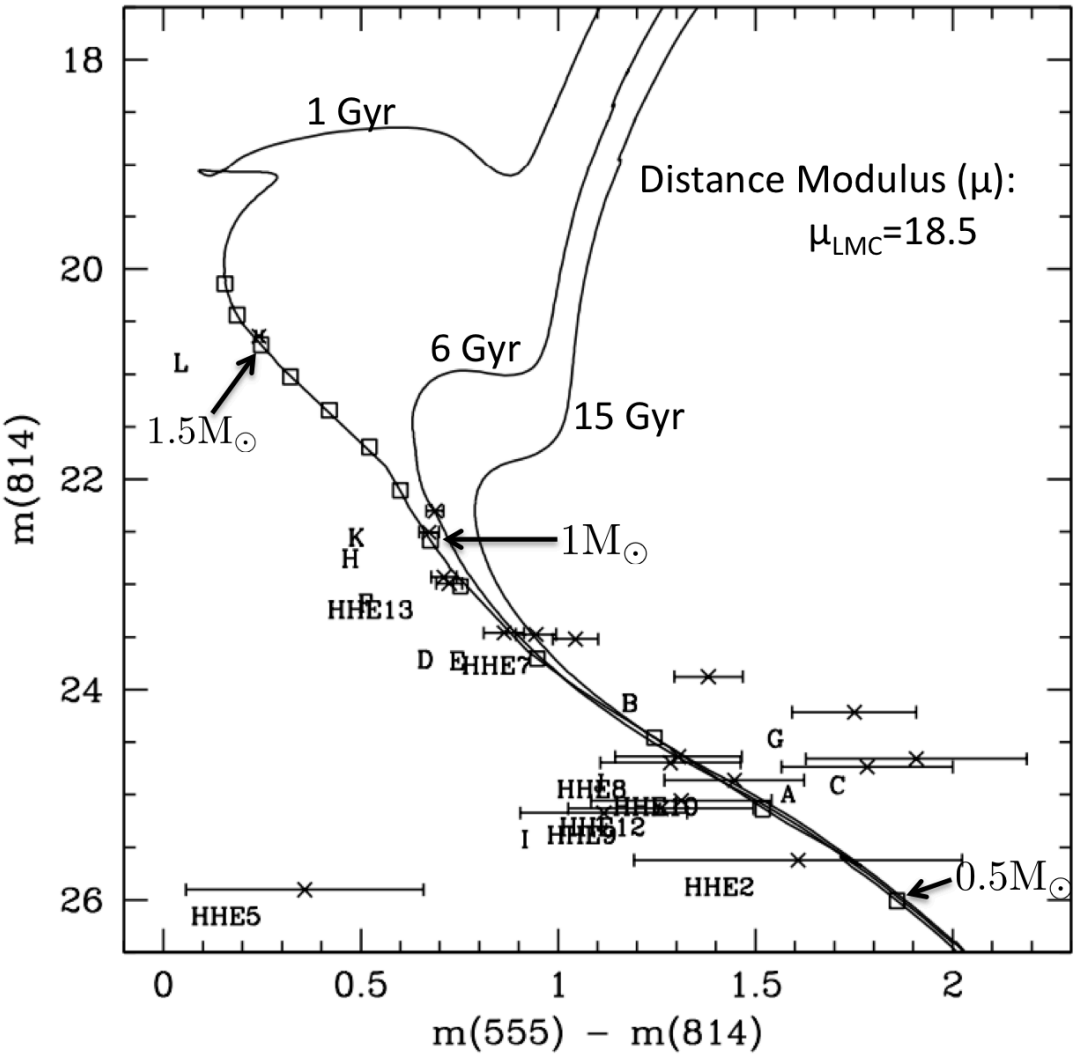

Figure 3.3 HR diagram with DESP isochrones (Chaboyer et al. 2001; Bjork & Chaboyer 2006; Dotter et al. 2008) over-plotted with our progenitor companion candidates for the SN that caused SNR 0509−67.5 using our photometry from the F555W and F814W WFC3 images. The data points are corrected for reddening using an E(B-V) value of 0.13, which comes from Warren & Hughes (2004), and the reddening values from Schlafly & Finkbeiner (2011) for an R_V of 3.1. The boxes that are over-plotted denote mass cuts from 0.5-1.7 $M_\odot$ in 0.1 $M_\odot$ increments from bottom-right to top-left.

and $[\alpha/Fe] = 0.0$. The squares on the plot mark out stellar masses of 0.5-1.7 $M_\odot$ in 0.1 $M_\odot$ steps (from the bottom-right to the top-left of the plot).

All of our progenitor companion candidates fall on the main sequence, with the possible exception of star HHE 5.

3.5 Conclusions

We add to the progenitor search conducted in Schaefer & Pagnotta (2012) by determining the possible offsets of the geometric center and explosion site from asymmetric expansion of the remnant. This is of particular concern due to apparent asymmetries in brightness and spectra of SNR 0509−67.5 that are seen in X-ray, ultraviolet, and infrared observations (Warren et al. 2005; Ghavamian et al. 2007; Williams et al. 2011a).

The remnant's proper motion measurements are projected onto our dynamical axis and we find a projected diameter of $26.350 \pm 0.034''$ and shock speeds of 5740 ± 380 km s^{-1} and 6370 ± 160 km s^{-1} to the W_D and E_D respectively. These values are used in hydrodynamic simulations to constrain the dynamical offset of the explosion site from the geometric center we report here.

The dynamical offset of the explosion site is determined in three unique ways: assuming a lifetime asymmetry in the ambient medium density, an asymmetry in the initial explosion energy between the eastern and western halves of 0509−67.5, and lastly, the asymmetry we observe in the E_D and W_D shock speeds is due to a recent density enhancement in the west. These dynamical offsets are $0.790''$, $1.370''$, and zero respectively with corresponding 3σ uncertainties of $2.06''$, $2.76''$, and $2.06''$ when we account for uncertainties that arise from locating the geometric center and from the dynamical offset modeling. These values also account for possible kick velocities the progenitor companion may have.

We are unable to place significant constraints on the possible north-south offset that may exist due to our especially sparse coverage in the southernmost portion of the rim where the signal-to-noise of the second epoch data imaged with the WFPC2 camera are too low

for us to measure the expansion. It would be unlikely however for the possible offset of the explosion site in the north-south axis perpendicular to our dynamical axis to be substantial, given that the asymmetry seen in the remnant occurs mainly along the E_D-W_D axis of the remnant.

We find 21 possible progenitor companions within our search zone determined with the aforementioned dynamical offsets and possible kick velocities that may have been imparted to the star at the time of the SN.

In the context of the spin up/down model of Di Stefano & Kilic (2012), we are unable to detect progenitor companions in the field if the time scale for the spin down of the accreting white dwarf exceeds the evolutionary time scale of the mass-donating star. The companion itself would have become a white dwarf, with apparent magnitudes dimmer than $m_V \sim 28.5$ mags (with our assumed distance modulus). Using the *HST* exposure time calculator, we find the simulated signal-to-noise ratios to be less than unity for our five simulated frames using the filters, numbers of dithered images, and exposure times from the WFC3 wide-band observations presented here.

In our sample of possible progenitor candidates we find that the masses inferred from our photometry show little evidence for any post-main sequence stars that would be consistent with SD models where the system is a recurrent nova or the companion is a classical symbiotic donor. We do however find that stars H, K, and L have masses > 1 $M_\odot$, which could be consistent with SD supersoft sources where a main sequence companion star is the mass donor in the system.

The remaining stars in our sample, with the exception of star HHE 5, encompass typical MS stars with masses in the range of $0.5 - 1.0$ $M_\odot$. This mass range corresponds to MS stars with spectral classifications M-G (Lang 1992). While these stars are seemingly unremarkable, there is a possibility that star HHE2 may be an M-dwarf star. The mass range of M-dwarfs is 0.10-0.57 $M_\odot$ (Lang 1992), thus most M-dwarf stars would be below our detection threshold, as was the case with white dwarf stars in the spin-up/down scenario

discussed earlier.

As Wheeler (2012) discusses, M-dwarfs are a class of stars that can posses strong magnetic fields, which given the correct circumstances would allow a magnetized WD to become locked at its magnetic poles with that of the M-dwarf star and result in a "magnetic bottle" that could allow for efficient mass transfer to grow the white dwarf's mass towards the Chandrasekhar limit.

The work of Wheeler (2012) also serves as a strong reminder that the majority of constraints posed on possible progenitor companions of Ia SNe result from simulations/models that do not include the effects of magnetic fields. Future simulations may open up the possibility of new classes of progenitor companions as modeling of mass-accretion improves and includes more physical effects.

Although more classical models are ruled out, the possibility that SNR 0509−67.5 resulted from a SD progenitor system is alive and well.

Chapter 4

Conclusions

As we have seen in the previous two chapters, this kinematic study of the LMC remnant 0509−67.5 has addressed many issues in astrophysics. Using the proper motion study of the remnant I was able to measure the global shock speed to be 6500 km s^{-1}. Using this global shock speed and the measured Hα flux of 0509−67.5, I was able to measure the neutral hydrogen density in the ambient medium to be $0.084 \pm 0.003(\epsilon_{H_\alpha}/0.2)^{-1}$ cm^{-3}, where ϵ_{H_α} is the number of Hα photons per ionization of hydrogen entering the shock.

The measured global shock speed, along with the measured average radius of 15″ (3.636 pc with our assumed distance of 50kpc to the remnant), allowed me to place the tightest constraints yet on the age of the remnant using one-dimensional hydrodynamic simulations. I find the age to be 310^{+40}_{-30} years with our preferred evolutionary model, while the previous best constraint on the age of 0509−67.5 was determined to be 400±120 years with the proper motion of light echo complexes (Rest et al. 2005a). Using the results from these hydrodynamic simulations in conjunction with the post-shock hydrogen density measured in Williams et al. (2011a), I determine that the compression factor of the blast wave is best fit with an effective equation of state in the range of $\frac{4}{3} \leq \gamma_{\rm eff} \leq \frac{5}{3}$, which corresponds to compression factors between seven and four.

When comparing the Balmer shock models of van Adelsberg et al. (2008) and Morlino et al. (2013a) to our measured proper motions of the portions of the remnant and the results of the spectral measurements of the broad Hα widths of Helder et al. (2010), I found no evidence of efficient CR acceleration in either the northeast or southwest filaments. Additionally, I was able to constrain the ratio of the ion-to-electron temperature, β, to be

$\beta \leq$ 0.03 at 1σ in the northeast filament of 0509−67.5 using the Balmer shock model of van Adelsberg et al. (2008) coupled with the measured $I_{\rm B}/I_{\rm N}$ and broad line width from Helder et al. (2010) and our measured proper motion of said shock. These results do not rule out efficient CR acceleration in these shocks, but rather indicate no need to attenuate the Balmer shock models that do not include CR acceleration to fit our data.

My last major result from this kinematic study concerns the search area for progenitor companions in the SD paradigm of Ia SNe. I find that there are 21 stars that are possible candidates, overturning the results of Schaefer & Pagnotta (2012) that argued the progenitor system had to be DD. Photometry of these stars allowed me to place constraints on the masses of these stars using the DESP isochrones shifted to a distance modulus of 18.5. We find that none of these stars have evolved off the main sequence, but could be candidates for supersoft sources for the stars with masses above $1 M_{\odot}$ or M-G type stars for the rest of the sample. These results have led me to conclude that the SD model for Ia SNe **cannot** be ruled out for 0509−67.5.

All of these findings have opened up many interesting questions that have led to my research plan for the next few years, upon which I will now expound.

My first priority is to apply the techniques developed in chapter 2 to the LMC remnant 0519−69.0. I am in possession of narrow-band Hα *HST* images separated by a year, and the data have been fully reduced and registered to the LMC microlensing catalog (Rest et al. 2005b). Figure 4.1 *left* shows the Hα image of 0519−69.0, which was imaged with the ACS aboard *HST*, and the right side of the figure shows a three-color X-ray image that I created using archival *Chandra* data. Using the proper motions along the shocked filaments, I will be able to hunt for signatures of efficient CR acceleration using optical spectra obtained with the RSS on SALT (see 1.2 in chapter 1). Preliminary analysis of these spectra shows a statistically significant broad component for multiple filaments in both of the slit locations observed.

Using proper motion measurements around the outer Hα filaments of 0519−69.0, I will

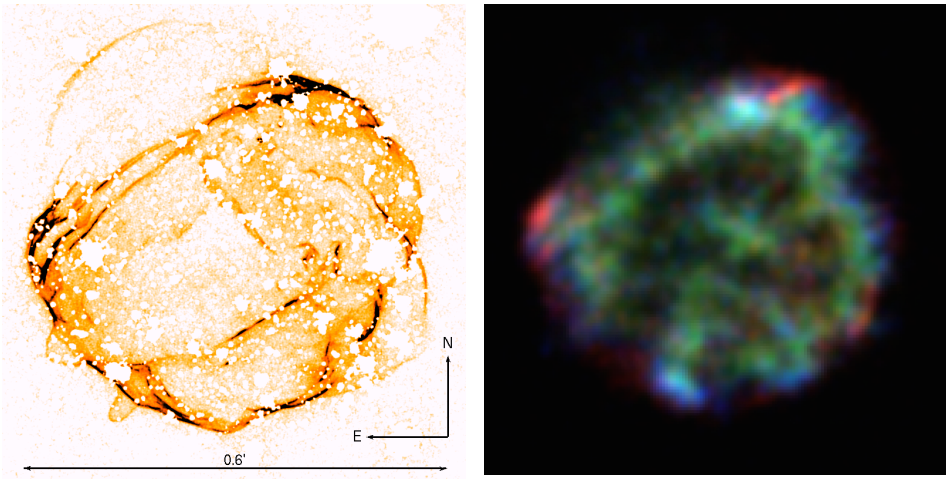

Figure 4.1 *Left* - *HST* narrow-band Hα Imaging of 0519−69.0. Field stars have been masked to accent the complicated shock structure of SNR 0519−69.0. *Right* - *Chandra* Advanced CCD Imaging Spectrometer (ACIS) observation of 0519−69.0. The red, green, and blue coloring respectively correspond to oxygen (0.3-0.6 keV), Fe-L (0.9-1.2 keV), and Si+S continuum (1.4-4 keV) emission in the shocked ejecta of SNR 0519−69.0.

constrain the search radius for progenitor companions in the SD paradigm with the techniques developed in chapter 3. This will address the main weakness of the determination of Edwards et al. (2012), who did not incorporate dynamical measurements into their explosion site measurement. I also plan on using F475W and F814W imaging acquired with the WFC3 aboard *HST*, which will become public 2016 February 21, to measure the photometric brightnesses of the progenitor companion candidates in the center of the remnant with the same techniques applied to 0509−67.5 in §3.3.3, and thereby determine the mass ranges of these stars.

Our findings in §2.4 have led me to begin a brand new analysis of the optical spectrum for the southwest rim of 0509−67.5. These data were taken with the FORS2 on the VLT and presented in Helder et al. (2010). I have fully reduced these data and removed both night sky lines and stellar continuum from stars in the field, which is shown in figure 4.2. The motivating factor for this fresh analysis is the complex shock structure in the southwest portion of the remnant, where we argue the results of the broad and narrow components of the Hα line were confused in the analysis of Helder et al. (2010), since there are two shocks

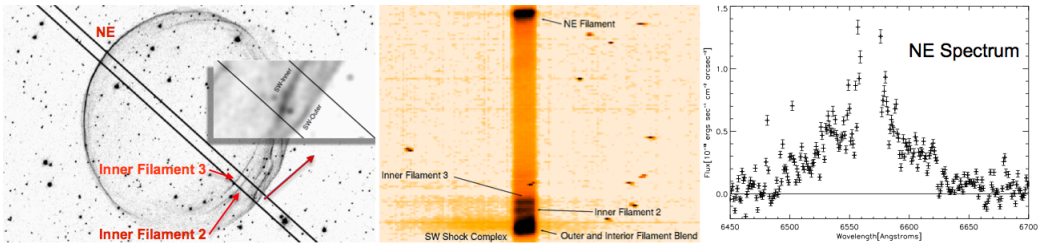

Figure 4.2 *Left* - *HST* narrow-band Hα image of SNR 0509−67.5. The longslit from Helder et al. (2010), along with a magnified view of the southwestern shock complex where there is a blend of an outer and inner filament, which are traveling at vastly different speeds. *Middle* - VLT FORS2 longslit spectrum of the Hα emission line of 0509−67.5 imaged on 2009-10-16 with Eveline Helder as PI (program id # 384.D-0518). Night sky lines and continuum flux from stars have been subtracted. The main filaments of the SW shock complex, as well as the filament in the northeast, of this spectroscopic re-examination are labeled. *Right* - Our fully reduced and calibrated 1-D spectrum of the broad Hα emission line in the northeastern portion of the forward shock of SNR 0509−67.5.

with greatly differing speeds that are separated by an amount similar to the PSF of the data (see §2.4). I highlight this complex shock structure in the left-hand panel of figure 4.2, which shows the slit position of the data on our Hα narrow-band image taken with the ACS aboard *HST*.

In addition to separating the measurements for the inner and outer filaments, we will measure the properties of the inner filaments 2 and 3, which are shown in red on the same panel of the figure. We have already made measurements of the angular expansion rate of these shocks in chapter 2. The middle panel of figure 4.2 shows the reduced two-dimensional spectrum of the Hα line where we can see a clear separation of the aforementioned inner filaments 2 and 3, but no apparent separation of the inner and outer filaments considered in §2.4. Figure 4.2-(*right*) shows the broad component of the Hα line from the northeast filament of 0509−67.5, which is clearly detectable with our reductions removing both night sky lines and stellar continuum from nearby stellar sources. We find statistically significant agreement between our measured broad line width in this northeastern filament and the value reported in Helder et al. (2010). This measurement is useful in confirming that the reductions I applied are correct.

My work in chapter 3 of this thesis has led us to take a deeper look at the possible

progenitor companion labeled star L in Schaefer & Pagnotta (2012). This star is of interest since it is the brightest star found in our uncertainty contours in §3.3.3. Unlike the majority of the stars identified as progenitor companions in §3.3.3, this star is bright enough to obtain ground-based spectroscopy. Beyond the practical reasons motivating the study of star L, it is the most massive star in our sample ($\sim 1.5 M_{\odot}$), which would be consistent with SD models where the progenitor system is a supersoft source. We have obtained an optical spectrum of this star with the RSS on SALT, and primary findings point to this star being an F-like star. Further analysis of the optical spectrum may unveil a large rotation rate of the star or other signatures of the stellar photosphere being modified by the SN that formed SNR 0509−67.5. Either of these would strongly suggest that star-L is the progenitor companion of a SD system that gave rise to SNR 0509−67.5.

I hope my readers have come to the same conclusion as I have, that supernova remnants are incredibly interesting sources that can shed light on many of the profound and unanswered questions facing astrophysics today.

Bibliography

Alcock, C., Allsman, R. A., Alves, D. R., et al. 2001, ApJ, 562, 337

Axford, W. I. 1981, in International Cosmic Ray Conference, Vol. 12, International Cosmic Ray Conference, 155–203

Badenes, C., Hughes, J. P., Bravo, E., & Langer, N. 2007, ApJ, 662, 472

Badenes, C., Hughes, J. P., Cassam-Chenaï, G., & Bravo, E. 2008, ApJ, 680, 1149

Bell, A. R. 1978, MNRAS, 182, 147

Bjork, S. R., & Chaboyer, B. 2006, ApJ, 641, 1102

Blandford, R., & Eichler, D. 1987, Phys. Rep., 154, 1

Blandford, R. D., & Ostriker, J. P. 1978, ApJ, 221, L29

Blondin, J. M., & Ellison, D. C. 2001, ApJ, 560, 244

Bloom, J. S., Kasen, D., Shen, K. J., et al. 2012, ApJ, 744, L17

Bowers, R. L., & Wilson, J. R. 1991, Numerical modeling in applied physics and astrophysics (Boston : Jones and Bartlett, c1991.)

Branch, D., Livio, M., Yungelson, L. R., Boffi, F. R., & Baron, E. 1995, PASP, 107, 1019

Burkey, M. T., Reynolds, S. P., Borkowski, K. J., & Blondin, J. M. 2013, ApJ, 764, 63

Canal, R., Méndez, J., & Ruiz-Lapuente, P. 2001, ApJ, 550, L53

Cargill, P. J., & Papadopoulos, K. 1988, ApJ, 329, L29

Carroll, B. W., & Ostlie, D. A. 2006, An introduction to modern astrophysics and cosmology

Chaboyer, B., Fenton, W. H., Nelan, J. E., Patnaude, D. J., & Simon, F. E. 2001, ApJ, 562, 521

Chevalier, R. A. 1982, ApJ, 258, 790

Chevalier, R. A., Kirshner, R. P., & Raymond, J. C. 1980, ApJ, 235, 186

Chevalier, R. A., & Raymond, J. C. 1978, ApJ, 225, L27

Clark, D. H., & Stephenson, F. R. 1975, The Observatory, 95, 190

Clementini, G., Gratton, R., Bragaglia, A., et al. 2003, AJ, 125, 1309

Colgate, S. A., & McKee, C. 1969, ApJ, 157, 623

Di Stefano, R., & Kilic, M. 2012, ApJ, 759, 56

Dilday, B., Howell, D. A., Cenko, S. B., et al. 2012, Science, 337, 942

Dotter, A., Chaboyer, B., Jevremović, D., et al. 2008, ApJS, 178, 89

Dwarkadas, V. V., & Chevalier, R. A. 1998, ApJ, 497, 807

Edwards, Z. I., Pagnotta, A., & Schaefer, B. E. 2012, ApJ, 747, L19

Eidelman, S., Hayes, K., Olive, K., et al. 2004, Physics Letters B, 592

Ellison, D. C., & Eichler, D. 1984, ApJ, 286, 691

Filippenko, A. V. 1997, ARA&A, 35, 309

Fryer, C. L., Ruiter, A. J., Belczynski, K., et al. 2010, ApJ, 725, 296

Gaskell, C. M. 1992, ApJ, 389, L17

Ghavamian, P. 1999, PhD thesis, Rice University

Ghavamian, P., Laming, J. M., & Rakowski, C. E. 2007, ApJ, 654, L69

Ghavamian, P., Raymond, J., Smith, R. C., & Hartigan, P. 2001, ApJ, 547, 995

Ginzburg, V. L., & Syrovatskii, S. I. 1964, The Origin of Cosmic Rays

González Hernández, J. I., Ruiz-Lapuente, P., Filippenko, A. V., et al. 2009, ApJ, 691, 1

Hamilton, A. J. S., & Sarazin, C. L. 1984, ApJ, 281, 682

Helder, E. A., Kosenko, D., & Vink, J. 2010, ApJ, 719, L140

—. 2011, ApJ, 737, L46

Helder, E. A., Vink, J., Bassa, C. G., et al. 2009, Science, 325, 719

Heng, K. 2010, PASA, 27, 23

Heng, K., & McCray, R. 2007, ApJ, 654, 923

Hovey, L., Hughes, J. P., & Eriksen, K. 2015, ApJ, 809, 119

Hughes, J. P., Hayashi, I., Helfand, D., et al. 1995, ApJ, 444, L81

Iben, Jr., I. 1997, in NATO Advanced Science Institutes (ASI) Series C, Vol. 486, NATO Advanced Science Institutes (ASI) Series C, ed. P. Ruiz-Lapuente, R. Canal, & J. Isern, 111

Kerzendorf, W. E., Schmidt, B. P., Laird, J. B., Podsiadlowski, P., & Bessell, M. S. 2012, ApJ, 759, 7

Kosenko, D., Ferrand, G., & Decourchelle, A. 2014, MNRAS, 443, 1390

Landau, L. D., & Lifshitz, E. M. 1959, Fluid mechanics

Lang, K. R. 1992, Astrophysical Data I. Planets and Stars.

Leibundgut, B., Tammann, G. A., Cadonau, R., & Cerrito, D. 1991, A&AS, 89, 537

Lewis, K. T., Burrows, D. N., Hughes, J. P., et al. 2003, ApJ, 582, 770

Li, W., Bloom, J. S., Podsiadlowski, P., et al. 2011, Nature, 480, 348

Long, K. S., & Blair, W. P. 1990, ApJ, 358, L13

Long, K. S., Helfand, D. J., & Grabelsky, D. A. 1981, ApJ, 248, 925

Lopez, L. A., Ramirez-Ruiz, E., Badenes, C., et al. 2009a, ApJ, 706, L106

Lopez, L. A., Ramirez-Ruiz, E., Pooley, D. A., & Jeltema, T. E. 2009b, ApJ, 691, 875

Mathewson, D. S., Ford, V. L., Dopita, M. A., et al. 1983, ApJS, 51, 345

McCully, C., Jha, S. W., Foley, R. J., et al. 2014, Nature, 512, 54

McKee, C. F. 1974, ApJ, 188, 335

Michael, E., McCray, R., Chevalier, R., et al. 2003, ApJ, 593, 809

Minkowski, R. 1941, PASP, 53, 224

Morlino, G., Blasi, P., Bandiera, R., & Amato, E. 2013a, A&A, 558, A25

—. 2013b, A&A, 557, A142

Nomoto, K., Thielemann, F.-K., & Yokoi, K. 1984, ApJ, 286, 644

Pagnotta, A., Walker, E. S., & Schaefer, B. E. 2014, ApJ, 788, 173

Patat, F., Barbon, R., Cappellaro, E., & Turatto, M. 1993, A&AS, 98, 443

Perlmutter, S., Aldering, G., Goldhaber, G., et al. 1999, ApJ, 517, 565

Peters, C. L., Lopez, L. A., Ramirez-Ruiz, E., Stassun, K. G., & Figueroa-Feliciano, E. 2013, ApJ, 771, L38

Phillips, M. M. 1993, ApJ, 413, L105

Raskin, C., Scannapieco, E., Rockefeller, G., et al. 2010, ApJ, 724, 111

Raymond, J. C. 1991, PASP, 103, 781

Raymond, J. C., Blair, W. P., Fesen, R. A., & Gull, T. R. 1983, ApJ, 275, 636

Rest, A., Suntzeff, N. B., Olsen, K., et al. 2005a, Nature, 438, 1132

Rest, A., Stubbs, C., Becker, A. C., et al. 2005b, ApJ, 634, 1103

Rest, A., Matheson, T., Blondin, S., et al. 2008, ApJ, 680, 1137

Reynolds, S. P., Borkowski, K. J., Hwang, U., et al. 2007, ApJ, 668, L135

Reynolds, S. P., & Chevalier, R. A. 1981, ApJ, 245, 912

Richtmyer, R. D., & Morton, K. W. 1967, Difference Methods for Initial-Value Problems, 2nd edn. (Malabar, Florida, USA: Krieger Publishing Company)

Riess, A. G., Press, W. H., & Kirshner, R. P. 1996, ApJ, 473, 88

Riess, A. G., Filippenko, A. V., Challis, P., et al. 1998, AJ, 116, 1009

Ruiz-Lapuente, P., Comeron, F., Méndez, J., et al. 2004, Nature, 431, 1069

Sabbi, E., Gallagher, J. S., Tosi, M., et al. 2009, ApJ, 703, 721

Schaefer, B. E., & Pagnotta, A. 2012, Nature, 481, 164

Schlafly, E. F., & Finkbeiner, D. P. 2011, ApJ, 737, 103

Schlegel, E. M. 1990, MNRAS, 244, 269

Schmitz, M. F., & Gaskell, C. M. 1988, in Supernova 1987A in the Large Magellanic Cloud, ed. M. Kafatos & A. G. Michalitsianos, 112–115

Schweizer, F., & Middleditch, J. 1980, ApJ, 241, 1039

Sedov, L. I. 1959, Similarity and Dimensional Methods in Mechanics

Slane, P., Lee, S.-H., Ellison, D. C., et al. 2014, ApJ, 783, 33

Smith, R. C., Kirshner, R. P., Blair, W. P., & Winkler, P. F. 1991, ApJ, 375, 652

Smith, R. C., Raymond, J. C., & Laming, J. M. 1994, ApJ, 420, 286

Sollerman, J., Ghavamian, P., & Lundqvist, P. 2003a, in From Twilight to Highlight: The Physics of Supernovae, ed. W. Hillebrandt & B. Leibundgut, 258

Sollerman, J., Ghavamian, P., Lundqvist, P., & Smith, R. C. 2003b, A&A, 407, 249

Thielemann, F.-K., Nomoto, K., & Hashimoto, M. 1994, in Supernovae, ed. S. A. Bludman, R. Mochkovitch, & J. Zinn-Justin, 629

Truelove, J. K., & McKee, C. F. 1999, ApJS, 120, 299

Tuohy, I. R., Dopita, M. A., Mathewson, D. S., Long, K. S., & Helfand, D. J. 1982, ApJ, 261, 473

van Adelsberg, M., Heng, K., McCray, R., & Raymond, J. C. 2008, ApJ, 689, 1089

Vink, J., Kaastra, J. S., & Bleeker, J. A. M. 1997, A&A, 328, 628

Wang, L., & Wheeler, J. C. 2008, ARA&A, 46, 433

Warren, J. S., & Hughes, J. P. 2004, ApJ, 608, 261

Warren, J. S., Hughes, J. P., Badenes, C., et al. 2005, ApJ, 634, 376

Wheeler, J. C. 2012, ApJ, 758, 123

Wheeler, J. C., & Harkness, R. P. 1986, in NATO Advanced Science Institutes (ASI) Series C, Vol. 180, NATO Advanced Science Institutes (ASI) Series C, ed. B. F. Madore & R. B. Tully, 45–54

Williams, B. J., Borkowski, K. J., Reynolds, S. P., et al. 2011a, ApJ, 729, 65

Williams, B. J., Blair, W. P., Blondin, J. M., et al. 2011b, ApJ, 741, 96

Williams, B. J., Borkowski, K. J., Reynolds, S. P., et al. 2014, ApJ, 790, 139

Woosley, S. E., ed. 1991, Supernovae: 10th Santa Cruz Workship

Woosley, S. E., & Weaver, T. A. 1994, ApJ, 423, 371

Wu, C.-C., Leventhal, M., Sarazin, C. L., & Gull, T. R. 1983, ApJ, 269, L5

Xue, Z., & Schaefer, B. E. 2015, ApJ, 809, 183

Yamaguchi, H., Badenes, C., Petre, R., et al. 2014a, ApJ, 785, L27

Yamaguchi, H., Eriksen, K. A., Badenes, C., et al. 2014b, ApJ, 780, 136

Young, T. R., & Branch, D. 1989, ApJ, 342, L79

Zel'dovich, Y. B., & Raizer, Y. P. 1967, Physics of shock waves and high-temperature hydrodynamic phenomena

Zwicky, F. 1940, Reviews of Modern Physics, 12, 66